# Self-Assembly of Matching Molecular Weight Linear and Star-Shaped Polyethylene glycol Molecules for Protein Adsorption Resistance

by

Christelle F. Jullian

Dissertation submitted to the faculty of the
Virginia Polytechnic Institute and State University
in partial fulfillment of the requirements for the degree of

Doctor of Philosophy
In
Materials Science & Engineering

Dr. Rick O. Claus, Chairman

Dr. Brian J. Love
Dr. Kathy Lu
Dr. Gary Pickrell
Dr. John L. Robertson

November 1, 2007
Blacksburg, Virginia

Keywords: Polyethylene glycol, Linear and Star-Shaped Molecules, Thin Films, Covalent Self-Assembly, Configuration, Albumin Adsorption

**Self-Assembly of Matching Molecular Weight Linear and Star-Shaped Polyethylene glycol Molecules for Protein Adsorption Resistance**

Christelle F. Jullian

## Abstract

Fouling properties of materials such as polyethylene glycol (PEG) have been extensively studied over the past decades. Traditionally, the factors believed to result in protein adsorption resistance have included i) steric exclusion arising from the compression of longer chains and ii) grafting density contribution which may provide shielding from the underlying material. Recent studies have suggested that PEG interaction with water may also play a role in its ability to resist protein adsorption suggesting that steric exclusion may not be the only mechanism occurring during PEG/protein interactions. Star-shaped PEG polymers have been utilized in protein adsorption studies due to their high PEG segment concentration, which allows to increase the PEG chain grafting density compared to that achieved with linear PEG chains. Most studies that have investigated the interactions of tethered linear and star-shaped PEG layers with proteins have considered linear PEG molecules with molecular weights several orders of magnitude smaller than those considered for star-shaped PEG molecules (i.e. 10 000 g/mol vs. 200 000 g/mol, respectively). Additionally, the star-shaped PEG molecules which have been considered in the literature had up to ~70 arms and were therefore modeled by hard-sphere like structures and low chain densities near the surface due to steric hindrance. This resulted in some difficulties to achieve grafted PEG chain overlap for star molecules.

Here, triethoxysilane end-functionalized linear PEG molecules have been synthesized and utilized to form star-shaped PEG derivatives based on ethoxy hydrolysis and condensation reactions. This resulted in PEG stars with up to ~4 arms, which were found to result in grafted star-shaped PEG chains with significant chain overlap. Linear PEG derivatives were synthesized so that their molecular weight would match the overall

molecular weight of the star-shaped PEG molecules. These 2 PEG molecular architectures were covalently self-assembled to hydroxylated silicon wafers and the thickness, grafting density, and conformation of these films were studied. The adsorption of human albumin (serum protein) on linear and star-shaped PEG films was compared to that obtained on control samples, i.e. uncoated silicon wafers. Both film architectures were found to significantly lower albumin adsorption. Figure 1 represents a schematic of linear and star-shaped PEG molecular coatings with matching molecular weight and covalently self-assembled to a given surface.

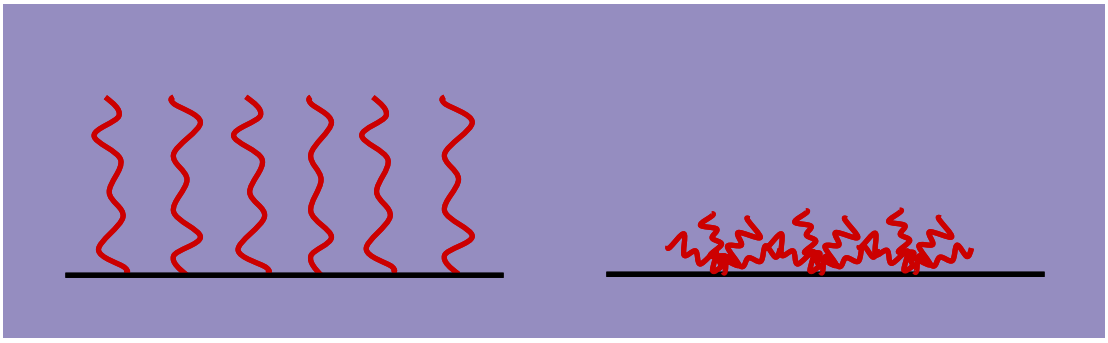

**Figure 1: Illustration of matching molecular weight a) linear and b) 4-arm star-shaped PEG molecules tethered to a surface and utilized for protein adsorption studies.**

**Acknowledgements**

I would like to thank the following people for their help and support during my work on this dissertation:

• My advisor, Dr. Rick Claus, for his support, encouragement, guidance, and patience over the last few years,
• Dr. Brian J. Love, Dr. Kathy Lu, Dr. Gary Pickrell, and Dr. John L. Robertson for serving on my committee,
• Dr. Bill Spillman Jr. for his support and many helpful discussions,
• Dr. Tim E. Long for his help on many aspect of this work,
• John Layman for his help with DLS measurements,
• Dr. Vicki Long for her help with DSC,
• Dr. Alan R. Esker, and his Ph.D. student Ufuk Karabiyik for helping with ellipsometry measurements,
• Geno Iannaccone, Bill Bebout, and Tom Glass for their help with NMR,
• Mehdi Ashraf for his help with GPC, and
• Frank Cromer for support with XPS.

I would especially like to thank my parents Dany et Juju, and my sister Bb for their love and support imported from France.

Last but not least, Merci Benouille!

*Dedicated to MLL*

## Table of Contents

## List of Figures

### CHAPTER I.



### CHAPTER II.



### CHAPTER III.

**CHAPTER IV.**

## List of Tables

**CHAPTER I.**



**CHAPTER II.**



**CHAPTER III.**



**CHAPTER IV.**

# CHAPTER I.

## INTRODUCTION AND BACKGROUND

### A. *Biocompatibility considerations*

#### 1. A need for better biocompatible materials and interfaces

Biomaterials and biomedical devices are currently being used in many different fields of medicine such as the stents that are used for the treatment of vascular diseases, and orthopedic implants or prostheses for replacement of knee, hip, shoulder, ankle, elbow, and finger joints. However, many of these biomaterial implants or devices induce complications when put in contact with the host. For instance, intravenous stents are used to treat atheroscleotic stenosis caused by plaque deposition and consequently limiting blood flow and raising blood pressure. However, the recurrent narrowing of the stent-treated artery (restenosis), leads to blood clot formation and inflammation of the stent-treated area. This ultimately leads to device failure and surgery. Research in biomaterials and biomedical devices aims at creating novel materials and coatings in order to create novel interfaces with appropriate structures and properties. These novel interfaces need to interact with the host in a positive manner, which means minimizing both the host reactions to biomaterials and the biomaterial reactions to the host[1].

Finding or creating materials that positively interact with the host is not a new concept. In fact, materials such as stone, bones and metal blades were used for skull surgeries in prehistoric times, which resulted in 80% patient survival on average. Later, silk, leather, wine, and egg albumin were used to treat wounds. From the Pharaonic times in Egypt until the Roman conquest around 30 B.C., a natural wood tar compound, cyclic alcohol gujacol was used for antiseptic purposes[2]. Borax, which occurs as natural deposits on earth, was used in medicine for its anti-bacterial and anti-fungal properties. Gold plates

and coconuts shells were used to repair defects in skulls by ancient civilizations[3]. Some of these techniques were practiced up until World War I, whose many casualties lead to the development of reconstructive and plastic surgery involving mostly grafts but also artificial parts to replace the eyes, chins, noses, and ears of wounded soldiers[4]. This led to the development of metallic and plastic facial and orthopedic implants, the use of powdered coagulant on the field, antiseptics, sterilization, and more sophisticated surgical tools.

Since then, much research and development of new commercialized products has been aimed at improving the outcomes resulting from biomaterials-tissue interactions. Among the most common host reactions to biomaterials are blood-material interactions, toxicity, inflammation, and infection. In parallel, biomaterials also greatly affect the host through enzymatic and mechanical degradation, calcification, and adsorption of tissue constituents. Medical cases prove that materials bioincompatibility can lead to device failure even when using the state of the art biomedical technology. Indeed, bioincompatibility of vascular grafts used for hemodialysis therapy causes platelets to accumulate in the graft, which consequently has to be replaced via surgery, although it is meant to be a permanent device. The development of well controlled drug-delivery devices and biodegradable polymeric scaffolds for tissue engineering are examples of some of the challenges that the field of biomedical research faces. Thus, new materials and coatings are continuously being studied with the primary goal of improving their interaction with body cells and fluids compared to commercially available materials.

In order to render a surface biocompatible, one may synthesize a new material or may modify the surface properties of a substrate by depositing a biocompatible film on that surface. In any case, the newly created interface will interact with the biological environment it is put in contact with, most likely comprised of various types of cells, proteins, and other biologically active components.

## 2. Host reactions to devices and biomaterials: Maintaining homeostasis

A sequence of events takes place following any medical device or biomaterial implantation[5]. Generally, this cascade of events occurs because incompatible or poorly compatible medical devices and biomaterials that are used to fabricate them, may induce immune, inflammatory and undesirable proliferative responses capable of damaging the host. The injury is translated into a change in homeostasis which may result from 2 types of interactions. Interactions between blood and the implanted material or device may take place, and/or interactions between a particular tissue and the implanted material or device may occur. Homeostasis is a characteristic of living organisms such as the human body, where an ensemble of mechanisms regulates and maintains the internal conditions of this organism. Changes in temperature, pressure, acid-base balance, waste concentrations, and salinity generally result in homeostasis imbalance, which in turn trigger host reactions. For instance, thermoregulation occurs when the skin temperature increases above a certain threshold, triggering blood capillaries dilatation (vasodilation) in order to increase heat transport (flow) carried by the blood, therefore increasing the cooling rate. Sweating and skin hair flattening are the other mechanisms that may occur in parallel to vasodilation. The amplitude of the homeostasis imbalance determines the degree of compatibility or incompatibility of a given biomaterial or device. Therefore, the various host reactions aim at maintaining homeostasis through the activation of series of checks and balances (i.e. feedback loops).

Among the various possible host reactions to a particular biomaterial or device, blood-material interactions occur relatively early in the process of maintaining homeostasis[5]. As mentioned above, blood contacting devices may be perceived as an injury by the host because blood-material interactions translate in a change of the cells and components of vascularized connective tissue. Proteins, cells, and fluid migrate from the vascular system to the injured area and protein and cell adsorption occurs on the injured tissue. Adsorption may be irreversible of reversible (followed by desorption) depending on the molecules and is often exothermic, occurring spontaneously and liberating energy. While fibrinogen proteins may desorb from a surface due to reversible adsorption, albumins

resist desorption fairly well. In fact proteins are known to start adsorbing on a surface less than a second after they contact that surface. Their early adsorption kinetics is a diffusion controlled process. This initial molecular and cellular change of the vascular system triggers the formation of blood clots (i.e. thrombi) at the interface as the result of the complex blood coagulation cascade. Inflammation, may translate into an increase of the number of white blood cells type molecules such as neutrophils, monocytes, and macrophages, and into the release of signaling proteins such as cytokines. Inflammation, which can be acute or chronic depending on its time scale (acute comes first and may become into chronic), is usually followed by the formation of granulation tissue around the implanted material. This granulation tissue, comprised on fibroblast and endothelial cells, will serve to create new capillary vessels and replenish the extracellular matrix components in collagen and elastin. In addition to granulation tissue, foreign-body reaction may occur where foreign-body giant cells and other cells such as macrophages form a layer around the biomaterial in an attempt to phagocytose it. Depending on the implanted material or device, fibrosis which is a fibrous capsule will also be present around the implant.

The variety of pathways that inflammatory reactions to biomaterials may take (thrombosis, acute and chronic inflammation, granulation tissue formation, foreign-body reaction, and fibrosis) was previously outlined. In addition to these inflammatory reactions, immune reactions may as well be triggered in response to a foreign material or device implantation. These are outlined in the following paragraph.

The immune system aims at protecting the host from foreign bodies such as bacteria, viruses, and chemicals, by recognizing the "non-self" histocompatibility proteins present on these cells. Contrarily to the inflammation reactions which may target both the biomaterial and surrounding tissues, the immune system would specifically target the implant. Interestingly, although the immune system's role is to protect the human body against infectious organisms such as viruses and other microbes, a nonactive and noninfectious material may trigger an immune response anyway. The innate immune system, which refers to the immediate and non-specific defense mechanism, involves

neutrophils, macrophages, and natural killer cells. Contrarily, the adaptive immune system involves antibodies and may also be activated against a biomaterial or device, potentially leading to device failure.

Finally, in addition to the inflammation and innate immune system reactions, the complement system, i.e. a biochemical cascade comprised of plasma and membrane proteins from the innate immune system, may in turn be activated. This system comprises membrane and plasma proteins with various roles, including "non-self" recognition proteins, inflammatory cells activation proteins, and cytotoxicity signaling proteins.

In addition to the effects of the biomaterial or device on the host which have been outlined, the host also affects the implant. This can result in wear, fatigue, corrosion, cracking, enzymatic degradation, and calcification of an implanted material or device.

## 3. Protein adsorption significance

### *a) The blood coagulation cascade*

As mentioned in the previous paragraph, biomaterial implants or devices trigger various complications when put in contact with the host including inflammation, blood coagulation, and implant encapsulation, whose goal is to keep the host healthy. However, protein adsorption on medical devices, whether it is blood proteins such as fibrinogen or structural proteins such as collagen, may lead to device failure. It is known that devices such as intravascular stents and arteriovascular grafts are affected by blood protein adsorption which is one of the primary events of the blood coagulation cascade potentially resulting in device failure. Within milliseconds after biomaterial-blood interaction, plasma proteins, largely fibrinogen, adsorb on the device surface. In fact, a competitive adsorption occurs, where reversible adsorption of proteins is followed by irreversible adsorption of other proteins. This is called the Vroman effect[6] and is outlined in the next paragraph. This irreversibly adsorbed protein nanolayer is known to

enhance the complex blood coagulation cascade that follows protein adsorption, and includes cellular adhesion and activation (i.e. platelets and leukocytes) and fibrin and platelet thrombi formation (thrombosis) which obstruct the blood flow potentially causing macroscopic thrombus associated with embolization risks. Platelets adhere on this protein layer and become activated. This is followed by the activation of high molecular weight kininogen and the polymerization of fibrinogen into fibrin, and fibrin cross-linking which results in blood clot formation[7]. The coagulation cascade is known to be a very complex process where a sequence of some 50 enzymatic reactions occurs that eventually leads to blood clot formation[8]. Figure 1.1 illustrates the complex coagulation cascade and fibrin formation, while Table 1.1 summarizes some of the coagulation factors. Note that Table 1.1 focuses on the factors that activate the blood coagulation cascade and therefore does not list most inhibitors such as antithrombin III and others.

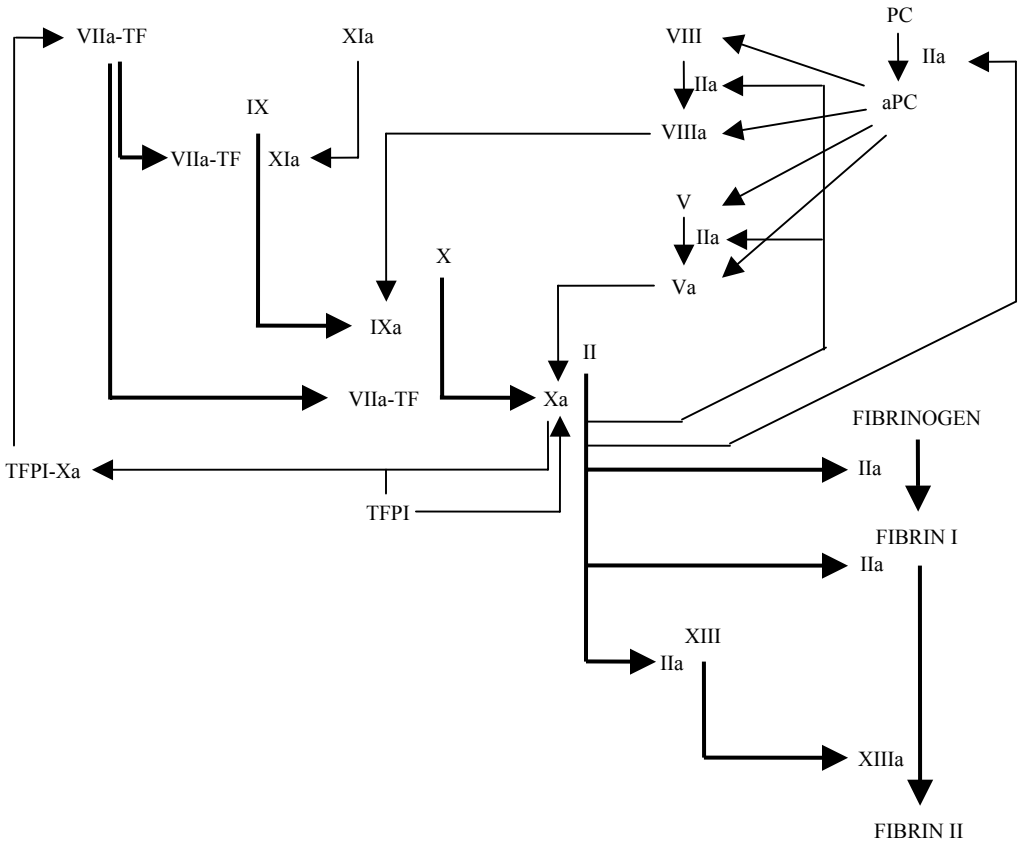


**Figure 1.1: Coagulation cascade involving various coagulation factors and formation of fibrin cross-linked polymers.**

**Table 1.1: Some important factors of the coagulation cascade.**

| Abbreviation | Factor | Common Name | Mw (kg/mol) | Conc. (µmol/l) | Act on |
|---|---|---|---|---|---|
| II/IIa | II/IIa | pro-thrombin | 72/37 | 1.4 | V, VIII, fibrinogen, XIII, PC |
| VII/VIIa | VII/VIIa | pro-convertin | 50/50 | 0.01 | IX, X |
| IX/IXa | IX/IXa | Christmas factor | 57/46 | 0.09 | X, VII |
| X/Xa | X/Xa | Stuart-Prower-factor | 59/46 | 0.17 | II, VII, V, VIII |
| PC/aPC | protein C | | 62/56 | 0.07 | Va, VIIIa |
| XIII/XIIIa | XIII/XIIIa | fibrin stabilizing | 320/160 | 0.1 | Fibrin |
| TFPI | tissue factor pathway inhibitor | lipid association coagulation inhibitor | 43/41/34 | 0.003 | Xa, VIIa |
| V/Va | V/Va | proaccelerin | 330/180 | 0.02 | Xa |
| VIII/VIIIa | VIII/VIIIa | antihemophil globulin A | 285/165 | 0.0007 | Ixa |
| TF | tissue factor | thromboplastin | 45 | memb. | VII, VIIa |

### *b) The Vroman Effect*

Plasma protein adsorption from solution to a biomaterial/device surface is a well accepted fact although it is neither well understood nor predictable given a particular milieu. The Vroman effect suggests that *in-vivo* plasma protein adsorption on a surface occurs following complex adsorption/displacement steps[6, 9, 10]. Proteins with highest mobility due to lower molecular weight are first adsorbed on the surface. These are then displaced (desorbed) by higher molecular weight proteins with higher affinity for the surface. Protein adsorption as a function of time or solution concentration rapidly increase, reaches a maximum and then a plateau as illustrated in Figure 1.2. This is also referred to as a Langmuir adsorption isotherm which is characterized by a rapid linear initial adsorption rate (diffusion controlled) followed by a slower rate which finally reaches steady state. Generally, lower molecular weight proteins exhibit lower affinity to solid surfaces while larger molecular weight proteins are characterized by higher affinity. Certain proteins such as albumins which are relatively low molecular weight (66 000 g/mol) compare to other plasma proteins and which have the highest concentration in blood of all blood proteins (i.e. 35-50 mg/ml plasma), are adsorbed immediately on solid interfaces, especially on blood contacting devices. It is believed that albumin adsorption

constitutes an exception to the Vroman effect, as adsorbed albumins may remain relatively stable and resist competitive adsorption/desorption. In other words, albumins may not readily be displaced by the adsorption of larger molecular weight proteins such as immunoglobulin, fibronectin, fibrinogen, and high-molecular-weight kininogen as depicted in Figure 1.3. Contrarily to albumin, fibrinogen, a larger molecular weight protein (340 000 g/mol) and in fairly large concentration in blood (i.e. 2-5 mg/ml plasma) has an adsorption kinetics that follows the Vroman effect and may be desorbed by high-molecular-weight kininogens for instance.

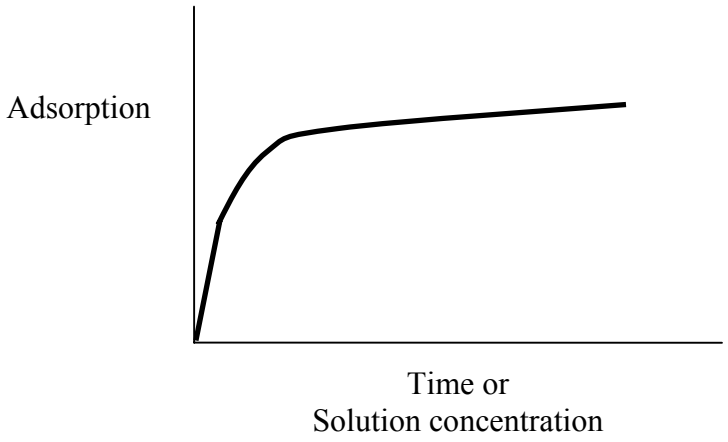


**Figure 1.2: Typical adsorption kinetics of a single protein in solution.**

*c) Protein structure in solution*

Proteins are essentially amino acid copolymers or organic-inorganic complex characterized by hydrophilic and hydrophobic areas, and positive and/or negative charges distributed within their structure. This implies that proteins are highly surface active and therefore favor surface binding and sometimes self-aggregation. Globular proteins such as human albumins have a fairly compact and ordered conformation in physiological aqueous solutions contrarily to flexible polymers in good solvent (i.e. random coils). This compact structure arises from forces exerted within the protein itself and between the environment and protein[10].

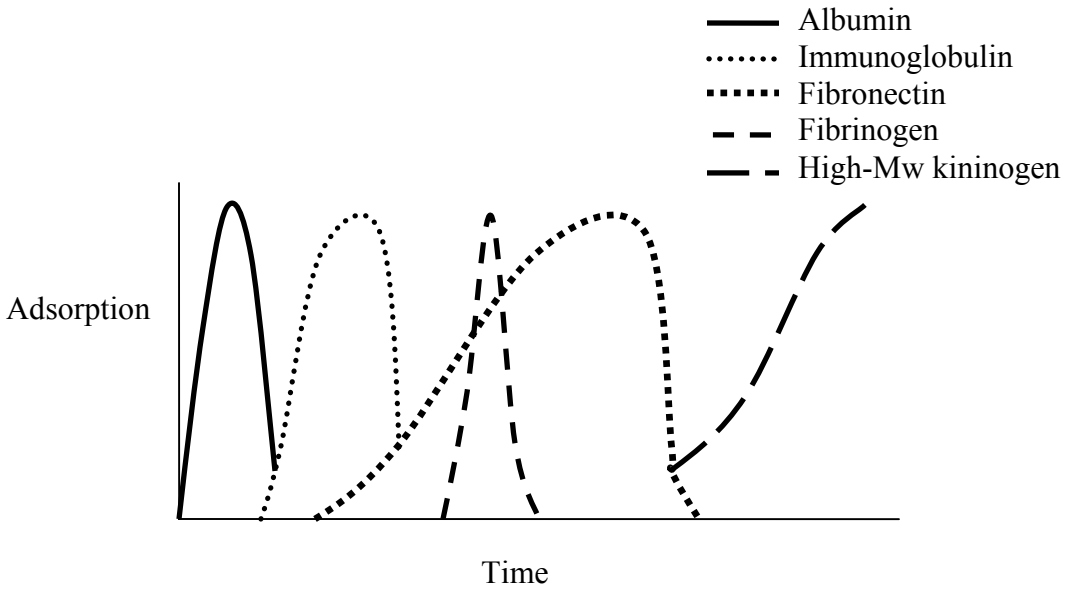


**Figure 1.3: Successive adsorption and desorption of various blood proteins on a surface.**

As major contributors, rotational mobility (i.e. increased conformational entropy) constitutes a major driving force for unfolding the protein structure while hydrophobic interactions favor its folded structure. Due to these competing forces, the folded compact crystalline protein structure can readily change to its corresponding denatured structure given small changes in solvent temperature, ionic strength, and pH. Hydrophobic interactions arise from the favorable dehydration of the hydrophobic moieties of a protein molecule when undergoing folding. Therefore, folded protein structures carry low conformational entropy which decreases the system entropy and increases the Gibbs energy of the system, while the hydrophobic dehydration increases the dissociated water molecules entropy, lowering the system Gibbs energy. Again, due to these competing thermodynamic energies the folded structure is fairly unstable.

Along with these major forces, additional factors play a smaller role in favoring either the folded or unfolded structure for a protein in solution. Coulomb interactions, mostly occurring between oppositely charged amino acid residues present on the outside of the protein structure due to their hydrophilicity, participate in stabilizing the structure. These Coulomb interactions strongly depend on the solvent pH and on the system isoelectric

point, so that, from a thermodynamic stand point, they favor either the folded or the unfolded structure. Van der Waals interactions between dipoles within the protein molecule and between water molecules should slightly favor protein compactness, although this effect is not clearly understood. Intramolecular hydrogen bonds between NH and CO moieties within a protein molecule allow for α-helices and β-sheets structures and may or may not contribute to the protein compact structure. There is an existing debate about whether hydrogen bonds within a protein molecule (i.e. between NH and CO moieties) and hydrogen bonds between water molecules decrease or increase the system Gibbs energy compared to hydrogen bonds between NH/CO and water molecules.

*d) Protein adsorption at solid interfaces*

Adsorption is generally believed to arise from a competition between conformational entropy reduction and polymer-surface attraction. In other words, adsorption occurs if the loss of conformational entropy is compensated by a positive interaction between the surface and polymer/protein (i.e. attraction)[10]. Protein adsorption from a solution to a surface can be driven by a variety of factors. These factors include protein/surface electrostatic interactions, protein/surface van der Waals forces which decrease hyperbolically with increasing protein/surface distance, surface and protein dehydration where adsorption occurs, and finally, adsorbed protein conformation change. A hydrophilic surface often promotes protein adsorption when it is charged, due to electrostatic attractive forces between oppositely charged proteins and surface. Proteins which are less structurally stable, i.e. those that will readily unfold, may adsorb on non-charged or similarly charged surfaces, due to the gain in conformational entropy associated with the adsorbed unfolded structure.

As mentioned in the previous paragraph, the various factors that affect protein adsorption to solid interfaces include material/device surface and protein electrostatic and van der Waals attractive/repulsive forces, material/device surface and protein dehydration (surface energy), as well as folded-unfolded conformation change associated with

adsorbed proteins at a solid surface. These factors are known to be interdependent. Solvent temperature, pH, and ionic strength are known to affect the material/device surface and protein electrostatic interactions, e.g. increased salt concentration or ionic strength increases the concentration of counter and co-ions at the vicinity of protein/material surface and often shield the electrostatic attractive forces between the proteins and the solid surface as well as the electrostatic repulsive forces between protein moieties. Therefore, increased ionic strength may lead to a lesser amount of adsorbed proteins at the surface. This ionic strength effect is often opposite to that observed on polyelectrolytes adsorption, where increased ionic strength promotes the formation of loops within the adsorbed layer. Thus, more polyelectrolyte mass is adsorbed per unit surface, which results in increased layer thickness. Varying the solvent pH affects the strength of acidic and basic functional groups, i.e. the strength of the so called *weak* ionic amino and carboxyl groups. At a pH below their isoelectric point, proteins carry a net positive charge, whereas at a pH above their isoelectric point they carry a net negative charge. Albumins dissolved in water containing 0.15M NaCl have an isoelectric point between 4.7 and 5.7 depending if they are lipid-bound or defatted[11]. Therefore, at pH of about 7.4, albumins will be characterized by a net negative charge. It is generally observed that maximum albumin adsorption on solid hydrophilic surfaces occurs at pH around the isoelectric point[12-14]. Albumin adsorption significantly drops when the solvent pH is either above or below the isoelectric point of albumin.

Overall, the change in Gibbs Energy associated with protein adsorption to a solid surface can be written as follows:

$$\Delta G_{Ads} = \Delta G_{\mathrm{Pr}otDehydr} + \Delta G_{SurfDehydr} + \Delta G_{\mathrm{Pr}ot/SurfAnd\,\mathrm{Pr}ot/\mathrm{Pr}otInteractions} + \Delta G_{Ads\,\mathrm{Pr}otConfChange} \quad (1)$$

where, $\Delta G_{\mathrm{Pr}otDehydr}$ is the change in free energy of the system associated with expelling proteins from solution and recovering hydrogen bonds between water molecules, $\Delta G_{SurfDehydr}$ is the change in free energy of the system arising from displacing the water molecules in contact with the surface by adsorbing proteins, $\Delta G_{\mathrm{Pr}ot/SurfAnd\,\mathrm{Pr}ot/\mathrm{Pr}otInteractions}$

corresponds to the change in free energy of the system resulting from electrostatic and van der Waals interactions between the surface and proteins as well as between close-by adsorbed protein molecules, and $\Delta G_{Ads\,\mathrm{Pr}otConfChange}$ is the change of free energy of the system due to the folded-unfolded entropic conformational change of adsorbed proteins.

In turn, protein adsorption will spontaneously take place if:

$\Delta G_{Ads} < 0$ (i.e. themodynamically favored reaction) (2)

Protein adsorption will have equal chances to succeed or fail if:

$\Delta G_{Ads} = 0$ (3)

Finally, protein adsorption will not take place spontaneously if:

$\Delta G_{Ads} > 0$ (i.e. themodynamically unfavored reaction) (4)

## 4. Blood contacting devices

As we have seen, it is well accepted that protein adsorption constitutes an important spontaneous event that influences the blood coagulation cascade, specifically by affecting platelet adsorption and activation, as well as fibrin polymerization and cross-linking, which ultimately leads to thrombus or blood clot formation. This is the so-called blood coagulation cascade and is well known and documented to occur on blood contacting devices. Therefore, what follows is an overview of some of the most utilized blood contacting devices in use today that treat vascular diseases and renal failure. These are intravascular stents and the hemodialysis extracorporeal circuit, respectively. Although these devices are widely used for therapy, complications that include thrombus formation on the surface of these devices decrease their efficiency. These blood contacting devices are discussed next. Anti-fouling coatings are of significant interest because they would potentially reduce blood coagulation on such blood contacting devices and would subsequently reduce complications such as inflammation.

*a) Intravascular stents*

Permanent metallic intravascular stents are currently the most common technology for the treatment of atheroscleotic stenosis, whereas balloon angioplasty is becoming obsolete. Stents are metallic mesh tubes implanted to prop open arteries which have been clogged with excessive deposition of lipoproteins on their lumen (inner lining of an artery). This constriction of the artery diameter consequently limits blood flow, creating high blood pressure, turbulent blood flow, and eddy currents formation. Although stents are meant to be permanent devices, in-stent restenosis often occurs after stent procedures. In-stent restenosis is the recurrent narrowing of the stent-treated artery due an excessive proliferation of smooth muscle cells and extracellular matrix synthesis such as collagen. In-stent restenosis is followed by stent thrombosis (blood clot formation), and inflammation.

The stent technology has been accompanied by numerous coating studies, which sought to identify coatings that would primarily decrease the in-stent restenosis rate. Stent coatings can either be permanent or biodegradable with drug-releasing properties. Therapeutic agent eluting stents, with rapamycin and taxol based coatings, have been shown to decrease smooth muscle cells proliferation and in-stent restenosis, and are commercially available[15]. These therapeutic agents are anti-proliferative drugs which are locally delivered to the vascular wall, limiting scar tissue build-up. One of the major drawbacks of this coating technology is the polymeric matrix which structurally supports the drugs and controls its release kinetics. Both biodegradable (poly(lactic acid), poly(glycolic acid)) and non-degradable (polyurethane, silicone) polymeric matrix induce long-term chronic inflammation at the site of the implantation. Another major challenge has been to engineer coatings with constant drug release rates to avoid early high rates followed by slower ones. Engineering coatings which would release drugs over several years would be of great interest in this particular case but has proven to be extremely challenging.

Films involving active agents such as heparin, natural biodegradable polysaccharides such as hyaluronan and chitosan have been extensively investigated[15, 16]. The layer-

by-layer (LBL) electrostatic self-assembly has been used as the fabrication process for these coatings because while heparin is highly negatively charged due to several sulfate groups, hyaluronan and chitosan have acidic and basic groups (carboxylic acid and amine respectively) which can easily become charged by controlling the solution pH. Heparin is commonly used during surgical procedures for its anticoagulant properties due to its antithrombin binding sites. When antithrombin binds to heparin, a conformational change increases by a thousand times its ability to bind to activated coagulation factor (e.g. thrombin) and therefore inhibit the coagulation cascade. Chitosan is derived from chitin, a fibrous material similar to cellulose. Hyaluronan has anti-proliferative and anti-inflammatory properties and is one of the chief components of the extra cellular matrix contributing to its structural and mechanical strength. Both chitosan and hyaluronan are subject to enzyme hydrolysis which ultimately controls their degradation and drug release rates.

Coated stents may reduce the formation of blood clots and early platelets activation in addition to the proliferation of vascular smooth muscle cells that are considered to be an important factor of restenosis after stent implantation[15, 17]. However, restenosis still may occur[18]. Localized delivery of DNA may more efficiently inhibit restenosis[19] but remains an expensive technology. Highly permanent and stable diamond-like-coatings (DLC) coatings have high hardness and are affected by micro-cracks due to large residual stress. Blood clot formation may actually result from large local modulus discontinuities arising from vessel wall/stent compliance mismatch[20]. Compliance matching stents, which more closely match the vessel wall compliance have therefore been developed in an attempt to investigate this problem[21].

### *b) Hemodialysis*

Hemodialysis therapy involves intimate contact of the patient's circulatory system with many different materials. Most of these materials are synthetic polymers such as polyvinylchloride that generally constitutes the tubing part, polysulfone, polyacrylonitrile, polyamide, and polymethylmethacrylate that constitute dialyzer

membranes. Arteriovenous accesses are generally made of silicone, teflon or polyurethane. Complications have been reported in the literature for decades. These include the usual protein adsorption, inflammation, coagulation, and cells activation and proliferation[22, 23]. Several coatings on arteriovenous grafts have attempted to minimize these complications. These coatings have involved hydrophilic coatings to hinder the hydrophobicity of membranes and grafts[23] and hydrophobic coatings[24]. Both have been found to decrease various protein adsorption and cell adhesion. This illustrates the current debate about surface energy (wettability) and biocompatibility.

### B. *Self-assembly of molecular coatings*

Illustrating the "bottom-up" approach, mostly for coating fabrication, with the ability to be combined with "top-down" approaches such as lithography techniques, self-assembly refers to the autonomous organization of functionalized molecules, cells, elements, systems into a desired, ordered architecture. One particular vision in this field envisions using various self-assembly processes at all scales in order to fabricate large-scale complex devices. Self-assembled atomic and molecular elements would be engineered to self-assemble into macroscopic systems and devices. Various types of interactions and forces may be involved in such a complex fabrication process. The most common forces, at least at the molecular level, arise from electrostatic, hydrogen bonding, hydrophobic, van der Waals, and $\pi$-$\pi$ interactions.

Complex self-assembly processes involving proteins and encoded by DNA are the biochemical basis of living organisms such as the human body. These self-assembling processes have inspired engineers and scientists to design novel systems and devices based on many different self-assembly techniques. The double-stranded helical structure of DNA (deoxyribonucleic acid) is governed by the self-assembly of complementary single-stranded moieties bound via hydrogen bonds. DNA self-assembly and disassembly regulates proteins and RNA synthesis for cells. Microtubules self-assemble and disassemble in a system that controls mitosis, a complex process of cell division

resulting in two identical daughter cells. Proteins continuously change their conformations by folding and unfolding their structure for chemomechanical, electromechanical, optomechanical, and optoelectronic purposes[25]. Membrane proteins bind to membrane lipids via hydrophobic and/or electrostatic interactions with calcium ions.

By mimicking the self-assembly processes naturally occurring in the biological world, researchers have been using and developing self-assembly processes to be integrated in artificial systems and devices. Short and long-range ordered structures, comprised of 1-, 2- and 3-dimensional structures such as nanowires, bilayer membranes, and 3-dimensional crystals, respectively have been integrated in devices. Most often, the design of such devices requires semiconductor-like architecture, a nanometer-scale architecture highly ordered in the x, y, and z directions. Therefore, multiple applications of self-assembled structures have risen reinforcing the importance of research in this area. Some of the most common fields where self-assembly has been applied are molecular electronics, optoelectronic, biotechnology and medical device development. These fields begin to merge when complex biotechnology devices incorporate integrated molecular electronics elements.

In this section, a general background on various self-assembly methods, their fundamentals, possible applications and limitations is provided. Both Langmuir-Blodgett (LB) and layer-by-layer (LBL) processes, which were developed long ago have been implemented, and have become very attractive fabrication methods. These will be outlined next. The section on self-assembly applications focuses on biotechnology devices where self-assembly has played a key role. Numerous electronic and optoelectronic devices have greatly benefited from SAM and LBL self-assembly techniques but are not within the scope of this dissertation.

## 1. Long-range ordered Langmuir-Blodgett (LB) films and Self-Assembled Monolayers (SAMs)

More than 8 decades ago, Langmuir published the first theory supporting the hypothesis that a monomolecular film can be created and self-assembled on solid surfaces[26]. However, it was only in the 1980's that the field of self-assembly started to grow exponentionally, partly motivated by the need of materials and devices miniaturized and controlled at the molecular scale.

Multiple monolayers of long-chain amphiphilic oil molecules were first realized by Langmuir and Blodgett based on the following theory. A sufficiently small amount of olive oil molecules dropped on clean water should maximize spreading resulting in one monolayer of oil at the surface of water[26]. Calcium ions from talc were used as a witness of the oil layer. By measuring the area of the oil layer, and knowing the volume of oil that was dropped, the layer thickness was estimated and found to be one molecule deep. Further, the orientation and packing of the oil molecules was demonstrated. The carboxylic acid end ($COO^-$) was found to be bound to calcium ions in the water, while the hydrocarbon end ($CH_3$) was facing up toward the air. The spreading of oil was hypothesized to be due to the presence of "active groups" in the oil molecule that combined with the water via "secondary valence".

Later, the transfer of a calcium stearate ($(C_{17}H_{35}COO)_2Ca$) monolayer from the air/water interface to a glass substrate was demonstrated with conservation of the order and packing that existed on the water[27]. The clean hydrophilic glass was placed in the "clean" water subphase. When risen through the floating molecules, the first layer was applied. The possibility of depositing successive monolayers was then demonstrated. Following the first monolayer applied during an upward motion of the substrate, alternating layers oriented in opposite directions were successively applied as the substrate was moving downward and upward. The film's alternating structure was deduced from the change in the wettability of the film outermost layer, given by the measurement of the surface's contact angle at different stages of the process. Surface

wettability is readily noticeable as the substrate emerges dry when the hydrophobic moieties are the outer moieties, whereas it emerges wet when the hydrophilic moieties are the outer moieties.

The LB deposition method has given rise to Self-Assembled Monolayers (SAMs), which are highly ordered and crystalline thin films. SAMs are very often used to mimic lipid biomembranes, but have found some applications in molecular electronics and biotechnology devices such as protein-based devices and sensors. These are discussed in Section B. 3.

### *a) Surfactants*

Approximately fifty years separated the first transferred LB film to the extensive use of this technique, which is now widely used for very different applications in various research fields. The surfactant molecules that are used can be hydrocarbon or fluorocarbon hydrophobic chains, whereas the hydrophilic moiety can be a polar or charged group ($NH_3^+$, $PO_4^-$, $COO^-$, $OH^-$) or even a small oligomer such as hexa(ethylene glycol). By definition, surfactants are specifically comprised of an active hydrophilic *head* and of a hydrophobic *tail*. The *head* undergoes chemisorption via the creation of a chemical bond with a liquid or solid interface, which may involve electrostatic and van der Waals interactions. The *tail* forms intermolecular van der Waals interactions with neighboring *tails* helping the packing and ordering of the floating surfactant. Since van der Waals are short-range interactions, high packing and order only occur provided a sufficient number of molecules. This is characterized by the surface pressure, introduced in the next paragraph. Depending on the polarity of the *tail*, long-range electrostatic interactions may also arise between neighboring *tails*. Finally, the third part of the amphiphile is the *end* group. It is usually a methyl ($CH_3$) group. The physical and chemical properties of these amphiphiles determine the architecture adopted in aqueous solutions. Shorter hydrophobic *tails* may result in more soluble amphiphiles, associating as micelles for instance in aqueous solution instead of floating monolayers.

*b) Surface pressure*

One of the critical parameters in building stable LB films is the bath surface pressure. A sufficiently high surface pressure implies that the floating monolayer is cohesive and highly crystalline. This highly ordered monolayer may then be transferred to a substrate conserving the same order provided that the surface pressure remains constant. This is done by physical motion of the bath barrier during transfer of the ordered floating monolayer to the substrate. Variable surface pressure translates into variable amphiphile orientations at the liquid interface as shown in Figure 1.4. As a result, film defects such as boundaries between solid, liquid, and gas phases, boundaries between crystalline and collapsed areas, and pinholes generally result from low surface pressures. This translates into thickness and refractive index non-uniformity, as well as rigid, amorphous, and unstable structures. As mentioned previously, this "ideal" surface pressure depends on the chemical and physical structures of the amphiphile molecules and is often obtained empirically. Water is a highly ordered liquid via hydrogen bonds and thus has a fairly high surface tension (73 mN/m at 20°C). Surfactants usually lower the water surface tension. The surface pressure $\Pi$ is simply the difference between the surface tension of pure water $\gamma$, and the surface tension with the floating monolayer $\gamma_0$ given as:

$$\Pi = \gamma - \gamma_0 \tag{5}$$

Controlling the surface pressure of the monolayer at the water-air/oil/gas interface allows control of the state of the monolayer at the liquid interface. The higher the surface pressure, the more tightly packed and ordered the monolayer. As a result, as surface pressure increases, the number of molecules per unit water surface increases, and the monolayer state at the interface may change from gaseous, to liquid, to solid. Gaseous state here refers to disordered floating molecules because the water surface available to the molecules is large. By decreasing the water area, the molecules are physically moved closer together until complete crystalline order is achieved.

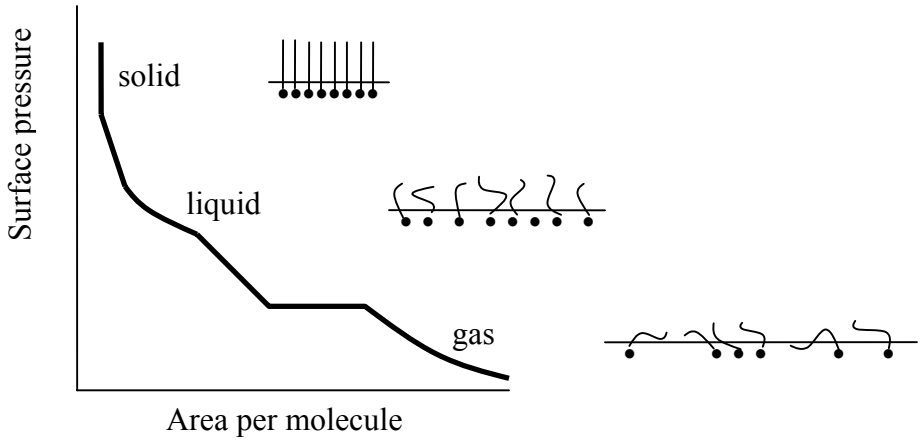


**Figure 1.4: Illustration of a Langmuir isotherm showing amphiphiles at the liquid interface in the crystalline, liquid, and gas phases, with their corresponding orientations.**

### *c) Monolayer transfer on solid surfaces*

*Procedure:* A substrate is immersed down through the monolayer or/and pulled up through the monolayer. When a hydrophobic substrate is immersed in the liquid through the monolayer on the liquid interface, the hydrophobic tails of the monolayer spontaneously adsorb on the substrate. Conversely, when a hydrophilic substrate is pulled up through the monolayer on the liquid interface, the hydrophilic heads of the monolayer adsorb on the substrate. Depending on the sequence chosen different structures can be achieved. A head-to-tail structure is created by depositing a first monolayer where the tails are adsorbed on the substrate and the heads are sticking out, and subsequently depositing a second monolayer where the tails adsorb on the previously deposited monolayer heads. By changing the substrate hydrophilicity/hydrophobicity and varying the dipping up/down sequence, tail-to-head, head-to-head, or tail-to-tail structures may also be created.

Troughs (i.e. LB film deposition apparatus) design has been significantly improved over the years. Automated systems improving deposition speed and film quality, and reducing vibrations with shock absorbers are in wide use today. A wide range of temperatures for

the water bath is available. Troughs comprised of 2 water baths and 2 rotating arms are now common, decreasing bath contamination and allowing multi-functional film fabrication. Deionized and bacteria-filtered water is used to ensure maximum purity. These improvements have resulted in improved structural quality or crystallinity of LB films.

*Monolayer/substrate interactions:* Self-assembly of monolayers can create long-range ordered structures. Although the nature of both the substrate and the amphiphilic molecules may differ, this particular adsorption mechanism is referred to as spontaneous chemisorption via the creation of a chemical bond between surface-active molecule heads and a surface-active substrate. Chemical bonds include covalent, ionic, dipolar, and hydrogen bonds. The LB plate substrate is usually made of platinum, glass, quartz, silicon, or mica. These allow for self-assembly of alcohols, carboxylic and fatty acids, phospholipids, and amines via van der Waals or ionic interactions, as well as self-assembly of hydrophobic tails on hydrophobic substrate via hydrophobic interactions. As seen in section A, the water pH, ionic strength, and temperature significantly affect the rate at which the floating monolayer can be transferred to a substrate.

*From LB films to SAMs:* Although self-assembled monolayers and multi-monolayers were first realized about 85 years ago, the creation of films with specified physical, mechanical, and thermal properties remains a challenge. One strategy has been to use amphiphilic monomers that undergo polymerization when stimulated by light. This approach clearly reinforces the film mechanical and thermal properties since van der Waals interactions between monolayers are replaced by covalent bonds. Increased film stability has also been achieved by taking advantage of electrostatic interactions between amphiphiles and other element such as proteins[28]. The LB process is also limited regarding the substrate size and topology which can be coated. Finally, while the LB technique offers fabrication of tailored molecular architectures, it is restricted to amphiphilic molecules with appropriate physico-chemical properties which make them insoluble, i.e. floating. The obtained long-range ordered structures often comport defects. Self-Assembled Monolayers (SAMs) carry the same high order and crystallinity as LB

films do, but are processed by immersing a substrate in a dilute solution containing amphiphile molecules. Because the deposition process occurs in solution, single SAM with the amphiphiles surface-active *heads* chemisorbed onto the surface active substrate limits the number of feasible film architectures. Consequently, van der Waals interactions usually control the adsorption process, inducing long-range order. While the LB technique allows for multi-monolayers deposition, SAM traditionally refers to a single, ultrathin, and crystalline monolayer. In fact, most SAMs are formed from stabilizing alkyl $CH_2$ chains, allowing for crystalline packing of the amphiphiles. This concept allows for some freedom in designing the amphiphile molecule. For instance Whitesides *et al.* have synthesized mixed SAMs comprised of highly crystalline hydrophobic alkyl moieties and highly amorphous hydrophilic oligo(ethylene glycol) moieties[29]. Because adsorption occurs in solution, soluble amphiphiles are used, which opens up new architectural possibilities such as utilizing micelles.

Compared to LB films, SAM deposition is controlled the diffusion of amphiphiles to the substrate which has the potential to provide longer-range order and less defects. Often, amphiphiles comprise thiol (SH) end-functionalities which are used to deposit organothiol monolayers on gold substrates due to high bond stability[30]. The deposition process is known to first occur via chemisorption of the amphiphilic active head onto the substrate which follows a $1^{st}$ order Langmuir isotherm. There is a linear relationship between the SAM adsorption rate and the number of unoccupied gold atoms. In addition, lateral rearrangement of the SAMs occurs in order to satisfy van der Waals attraction forces between neighboring chains, and consequently, to achieve long-range order. Van der Waals interactions are maximized by a 30° tilt of the alkyl chains (from the gold surface normal) arising from the hexagonal structure of S-Au bonds[31]. Organosilicon SAMs deposited on hydroxylated substrates (OH functionalized) is the other well known and stable system based on Si-O covalent bonds. Organosilicon SAMs are characterized by some of the strongest adhesion to the substrate due to the high binding energy of siloxane Si-O-Si bonds, but are not as ordered as organothiol-based SAMs. Figure 1.5 represents organothiol and organosilicon SAM structures.

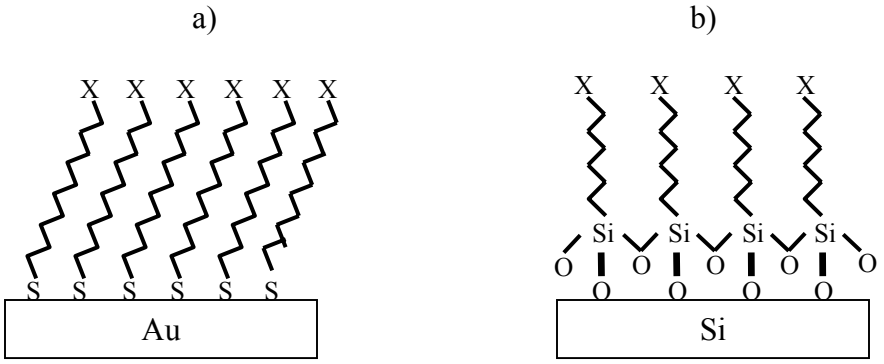


**Figure 1.5: a) Organothiol SAMs on a gold substrate showing the 30° tilt angle with the surface normal and the long-range order, and b) organosilicon SAMs on a hydroxylated silicon substrate. The Xs represent the end groups attached to the tails, which are most of time hydroxyl (OH) or methyl ($CH_3$) groups.**

## 2. Layer-by-layer (LBL): towards shorter-range ordered structures

### *a) Electrostatic-based Self-Assembly*

In contrast to LB films and SAMs, layer-by-layer (LBL) self-assembly allows for the formation of multilayers that may exhibit short-range order as opposed to long-range order seen with LB films and SAMs. This results from the common deposition of high molecular weight flexible polyelectrolytes, which renders LBL films more amorphous in nature with a fuzzy structure. However, this more amorphous structure has shown to be appropriate for many applications such as organic light-emitting diodes and photovoltaics due to the absence of defects which are readily introduced using LB films and SAMs. 2- and 3-dimensional self-assembled structures have been demonstrated.

In 1992, Decher and coworkers introduced this novel technique to deposit polyelectrolyte thin films on charged substrates based on electrostatic attraction[31]. Cationic and anionic polyelectrolytes in solution at relatively high concentrations were successively adsorbed on an oppositely charged surface, inducing a reversal of the surface charge. A rinsing step in between deposition of each cationic and anionic layer is necessary in order to remove loosely attached ionic residues and prevent solutions's contamination. The

formation of multilayer assemblies was thus achieved by Decher and coworkers. Up to 100 layers were deposited, and the linearity of the process was demonstrated using UV/vis spectroscopy and small angle X-ray scattering, techniques still used today. The film thickness was found to increase linearly with the number of bilayers.

The LBL technique can actually be considered to have been originally demonstrated by the alternate deposition of charged inorganic colloids by Iler in 1966[32]. Later, magnetic particles[33], polyelectrolyte polymers[31], functionalized fullerenes[34], charged DNA[35], proteins[36], gold nanoparticles[37, 38], and clay platelets[39] were self-assembled on substrates based on electrostatic interactions. The LBL deposition technique is therefore appropriate for various types of nanoparticles and biomolecules in addition to polyelectrolytes, which makes it considerable more versatile than LB films and SAMs. Additionally, the adsorption of higher molecular weight molecules makes the LBL technique appropriate for building supramolecular self-assembled systems. Kunitake demonstrated the fabrication of ordered multilayers free standing films, which opened up new perspectives[40]. Casting of dispersed bilayers and polymers was found to conserve the multilayer architecture, and therefore, ordered free-standing composite films were demonstrated. The tailoring of molecular design and interactions translated the multilayer molecular order into macroscopically ordered materials. Multilayer composite cast films made from dispersions of amphiphiles, polymers, proteins, quantum sized metallic particles (CdS), and metal oxide ($Al_2O_3$), have been fabricated[40].

LBL films can be highly uniform due to the conformal nature of the LBL electrostatic self-assembly process. The driving force is the electrostatic attraction between oppositely charged or polar groups on the substrate and on a given adsorbent. As mentioned in Section A with protein adsorption on a solid surface, adsorption of charged or polar molecules on a surface will induce a change in free energy at the interface. This change in free energy is associated with the desolvated substrate, the displacement of counterions at the interface, and the electrostatic attraction between the substrate and the charged adsorbent. Indeed, the formation of LBL self-assembled architectures represents a thermodynamic equilibrium (minimum free energy) that is mainly governed by a change

in entropy and a relatively small change in enthalpy. The change in enthalpy depends on the interactions between adjacent bilayer molecules, and is supposed to be relatively small compared with covalent bond formation for example. The change in entropy occurs by bringing molecules close to each other, and which were originally somewhat far apart. This depends on the solute concentration and creates a decrease in translational entropy, while binding these molecules to the substrate induces a small decrease in conformational entropy. Note that the change in entropy is smaller for the LB technique than for the LBL process, because the LB technique is only affected by a relatively small decrease in conformational entropy since the molecules are already ordered at the water-air interface. This entropy loss is outweighed by a large entropy gain due to the liberation of solvent and counterions from the interface, which drives the adsorption. Because of the change in entropy, kinetic controls the adsorption of LBL molecular layers.

### *b) Factors influencing adsorption and structure*

As in the LB process, the solution pH, temperature, and concentration are known to affect the LBL film structure and deposition rate. This is due to the fact that LBL film deposition is controlled kinetically due to a great change in entropy during molecule adsorption.

The influence of adsorption time and ionic strength of the solutions on the film growth and thermal properties have been studied[41]. Polyelectrolyte multilayers were found to have low roughness compared to bare glass, while increasing salt concentration or ionic strength led to thicker layers. As seen in Section A, increased salt concentration results in increased electrostatic shielding between polyelectrolytes in solution. This implies that polyelectrolytes in high ionic strength solvents form denser structures with loops as opposed to more loose structures when no or less salt is added. In turn, polyelectrolytes adsorb on the surface conserving the same dense structure which leads to more polyelectrolyte mass per unit area, i.e. thicker layers. Increased ionic strength also shields the attractive forces that exist between oppositely charged surface and

polyelectrolyte molecules. The layer thickness and roughness have been found to increase nonlinearly with the salt concentration. This means that there should be a critical salt concentration that can be added without causing too many defects or too much roughness.

Additionally, polyelectrolytes often contain weak ionic groups such as amine and carboxyl groups whose charges strongly depend on the aqueous solution pH, i.e. it depends on whether the pH is above or below the polyelectrolyte isoelectric point. At a pH close to the isoelectric point, the polyelectrolyte will be uncharged and will adsorb as a relatively thick layer due to water becoming a poorer solvent and due to loops formation. However, at a pH either well above or below the isoelectric point, the polyelectrolyte will be fully charged, and will adsorb as a thinner layer due to stronger interactions between the surface and the corresponding polyelectrolyte. Polyelectrolyte concentrations also affect the deposited layer structure. Higher concentrations may result in larger surface charge reversal, adsorption time reduction, and thicker layer due to chain contraction and loops formation. Drying steps in between layer deposition may also affect layer thickness due to swelling decrease, especially for hygroscopic molecules.

As demonstrated by Schmitt and others later, the internal structure of these polyelectrolyte films has often been studied with X-ray and neutron reflectivity and were found to be characterized by a fuzzy internal structure[42]. Although these polyelectrolyte films have a well defined supramolecular internal structure, bilayers interpenetration is known to occur. Schmitt reported that about 50 % of a given layer was in fact overlapping with neighboring layers, the layers close to the substrate being thinner than those closer to the film/air interface. Anionic and cationic layers have been found to have different thicknesses, again depending on electrostatic interactions shielding. Inorganic counterions, such as $Na^+$ and $Cl^-$, from the solutions may also be adsorbed into the multilayers.

*c) LBL advantages*

As an alternative to LB films, the LBL process is simpler because adsorption occurs spontaneously in solution and is kinetically controlled. Therefore, adsorption rates and film built-up are generally faster for the LBL than for the LB process, usually on the order of several minutes per layer, although it has been shown to be on the order of hours for gold colloids[31]. Generally, LBL involves stronger intermolecular interactions such as long-range electrostatic interactions, leading to more stable films and defect-free when amorphous polyelectrolyte layers are used. There is no restriction on substrate size and geometry. The increased range of materials that may be deposited using the LBL vs. the LB method is appropriate for multiple applications ranging from electronic, to photonic and biomedical devices. For instance, the use of proteins and DNA allowed the fabrication of coatings and devices useful for biomedical applications. The use of conducting polymers and magnetic nanoparticles shows promises for electronic and photonic devices. While LB films are mostly used as an interface in devices and to mimic biological membranes, LBL multilayers have had impact in various fields of research.

## 3. Nanoscale self-assembly: A wide range of applications

Thin-films with electrical, magnetic, optical, and biomedical functionalities have been fabricated using self-assembly of polymers, metals, ceramics, semiconductors, and biologically active species. The focus of this section is on the bionanotechnology field. Following is a discussion on some important and diverse research that has been reported since the establishment of self-assembly as a viable technique for various bionanotechnology device fabrication. Several levels of device complexity has been considered, ranging from molecular sensors to molecular manufactures as some have envisioned. Protein-based devices, where proteins have been immobilized on semiconductor substrates could be used as sensors[25]. A greater challenge would be to self-assemble molecular elements in order to create functional devices such as molecular transistors, which would mimic metal-oxide-semiconductor-field-effect transistor or

MOSFET functionality at higher device densities. Increasing in the scale of complexity, biomolecular logic gates are believed to offer potential for integrated circuits provided appropriate organization. Research has shown that processes mostly relying on molecular self-assembly, such as protein self-assembly, in order to create 2-dimensional lattices for sensing applications result in many lattice defects. This remains a major limitation. Consequently, the preferred biotechnology device fabrication methods are based on a mixture of self-assembly and lithography-type methods.

*SAM for biosensor interface:* Considering the diverse functions of existing proteins, it is possible to engineer a wide range of biosensors arising from electrochemical, electromechanical, and optoelectronic interactions. The organization of protein molecules in a controlled manner on a 2-dimensional electrode pattern may be utilized to fabricate various biosensors. SAMs have been widely used to create junctions between proteins and electrodes, emphasizing the importance of SAMs molecular conductance. One of the first molecular conductance measurements was performed by Reed and coworkers in 1997 using a single benzene-1, 4-dithiol SAM molecular junction between 2 gold wires[43]. Demonstrating reproducible charge transport through 1 SAM, SAM-functionalized electrode patterns have become a widely used design tool for biosensors. It is well accepted that the presence or absence of chemical bonds, as well as the nature of both the electrode and the SAM molecule affect current transport properties through the SAM/electrode. The organic molecule length is known to be a critical parameter for charge transport as the current through the deposited organic SAM is found to decrease exponentionally with SAM's length[44]. As expected, the electronic transport has been found to increase when SAMs are chemically bound to two electrodes rather than only one[45]. Two chemical contacts versus only one induce current transport that is from 1 to 4 orders of magnitude larger than when only 1 chemical contact is present. However, no significant change in current transport was noticed between different SAMs molecule/substrate combinations. C-Si, S-Hg, and S-Au junctions seem to have an insignificant effect on the electronic transport[45-47]. Organothiols comprised of alkane and phenyls chains have been chemisorbed on gold, silver, copper, platinum, palladium

substrates via thiol functionalities, while organosilanes SAMs may be deposited on hydroxylated semiconductor silicon and dielectric substrates.

*Towards biosensors:* A molecular biosensor is usually comprised of a recognition moiety and a signaling moiety. Considering the diverse functions of existing proteins, it is possible to engineer a wide range of biosensors arising from electrochemical, electromechanical, and optoelectronic interactions. Protein-based biosensors may take advantage of the highly specific protein-ligand interaction, which is irreversible, therefore stable and appropriate for sensor applications[48]. Ringler and Schultz[48] have attempted to fabricate a 2-dimensional lattice network with predetermined dimensions and symmetry based on the structural proteins streptavidin and L-rhamnulose-1-phosphate aldolase (RhuA). Streptavidin (S) is well known for incorporating 4 biotin binding sites per molecule. RhuA was genetically modified in order to induce 8 biotin binding sites per molecule. Using electron microscopy, it was demonstrated that rapid mixing of these proteins resulted in the self-assembly in solution of RhuA and S via biotin linkers with the stochiometry $(RhuA)S_4$. $(RhuA)S_4$ were comprised of a central RhuA molecules attached to 4 S, one on each side of the cube-like RhuA molecule. $(RhuA)S_4$ may represent a single building block of a possible 2-dimensional lattice based on the self-assembly of multiple $(RhuA)S_4$ units. Using a floating lipid monolayer that was allowed to interact with $(RhuA)S_4$ and (RhuA) units, the fabrication of a 200 nm by 200 nm 2-dimensional lattice comprised of $(RhuA)S_4$ and (RhuA) units was demonstrated. The main limitation was that the lattice showed numerous disordered aggregates and deviations from the unit's stochiometry. These potentially uniform 2-dimensional lattices could result in biosensor applications utilizing for instance proteins with electrochemical functionalities, which would constitute the signaling and recognizing moieties. Biosensors have also been designed based on the controlled adhesion and growth of cells on a given substrate. Cell adhesion can be controlled at the nano/microscales through the pre-adsorption of proteins which will either favor or disfavor cell adsorption and growth. This may thus give rise to a 2-dimensional cell-patterned electrodes usefull for biosensor applications. SAMs with various "*tail*" or *"head"* functionalities, i.e. antifouling or fouling tail molecules, have been used for the

purpose of modifying a surface properties to make it protein friendly or protein resistant. Varying SAMs physico-chemical properties changes SAMs protein adsorption properties, which control cell adhesion. Whitesides and coworkers used the strong gold-thiol affinity to chemisorb oligo(ethylene glycol)- and methyl- terminated SAMs on a gold surface to selectively guide endothelial cells[49]. The SAM-endothelial film was then desorbed when a small voltage of 1.2 V was applied. If these adsorption/desorption steps are reversible, mechanical release and uptake would be created, of interest for nano-electro-mechanical systems. DNA's self-assembly properties have also been used to create various molecular structures relevant to biosensors[50, 51]. Microfluidic devices have been of interest for biosensing applications as well. SAM-patterned electrodes have been used to fabricate wall-less microfluidic device, which were operated with a magnetohydrodynamic pump. This design allowed for the elimination of wall's fouling properties and for the reduction of flow resistance and therefore higher flow rates. Fouling issues have challenged the well-function of fluidic devices due to non-specific protein adsorption and subsequent cell adsorption.

*Biomimetic membranes:* Supported phospholipid bilayers (SLB), which are comprised of 2 phospholipid monolayers transferred from the air-water interface onto a substrate (glass, quartz, and silicon wafers substrates) were first synthesized by McConnell and coworkers using the LB method[52]. SLB mimics biological lipid membranes because they are designed and engineered to allow for a thin water layer to exist between the solid support and the phospholipid bilayers[53]. This design allows for the conservation of various membrane functionalities such as the specific and non-specific adsorption and binding of proteins on the membrane. SLB can be modified with various functionalities to trigger specific binding processes such as SLB functionalization with biotin to study the specific interactions of avidin and biotin which constitutes a typical protein-ligand interactions model. Additionally, SLB patterning on the micron scale with nanometer resolution could lead to a multi-functional SLB, allowing for microfluidic devices fabrication or 2-dimensional membrane arrays[54]. These arrays may be utilized to simultaneously study several specific interactions for high-throughput applications. As a result, SLB-based structures have become a key element for the fabrication of biomimetic

membranes, biosensors, and *on-a-chip* systems[55]. *On-a-chip* systems may integrate biomimetic membranes (including membrane-binding proteins for instance), living cells, microfluidics, electronics, and sensors. Chemical and biological processes such as cell-to-cell, ligand-receptor, and antibody-antigens interactions for immunoassays, ion transports through selective membrane channels, membrane rearrangement to accommodate for membrane binding events to occur, have been studied using SLB. Stochastic sensors represent an important sensing technology as they allow fast detection of specific molecules in solution and have been fabricated based on a lipid bilayers membrane[56]. The membrane possesses a nanopore through which the molecules of interest are able to pass through, changing the observed ionic current through the membrane under an applied potential. Current blockages are therefore created and monitored. The current blockage's magnitude, duration, and frequency are related to the molecules size, type and concentration. Lipid bilayers comprising a protein nanopore (α-hemolysin) have been stabilized by encapsulating the film in porous agarose gel. This encapsulation increased the device stability by minimizing structural disturbance of the bilayers and permits device transportation.

*Drug delivery devices:* Drug delivery devices via self-assembly of amphiphilic block copolymers forming micelles type structures have been used to transport and deliver drugs[57]. Typically, the block copolymers are formed of biodegradable hydrophobic and hydrophilic polymers, which spontenously self-assemble as spherical micelles in water with the hydrophobic moieties organize to form the micelle core and interact with a hydrophobic drug, while the hydrophilic moieties interact with the solvent and therefore form the outside shell. Most often, the hydrophilic part of the block copolymer is poly(ethylene glycol) with a molecular weight around 1,000-10,000 g/mol to resist protein adsorption which could jeopardize the delivery of the encapsulated drug. A similar encapsulation method using micelles has been applied to gene delivery devices[58]. While hydrophobic drugs are encapsulated via dialysis or emulsion methods taking advantage of micelle core/drug hydrophobic interactions, other encapsulation methods had to be invented for metal-containing drugs and hydrophilic drugs. For metal containing drugs, the formation of a polymer-metal complex is usually a key step.

Micelle core/drug hydrogen bonds and π-π interactions may also be a driving force for drug encapsulation. Because controlled drug-release is difficult to obtain, and due to the accumulation of biodegradable polymer moieties in our organism which remain problematic, pH-responsive drug delivery devices have become the preferred technique[59, 60]. pH-sensitive micelles are specifically suitable for selective drug/gene/dyes delivery inside cells, where it is slightly more acidic (pH~ 4-5) than the physiological pH of 7.4. Often, the release of the functional element is triggered by a pH decrease which causes micelle break-up. The endocytotic pathway is believed to allow the absorption of the polymeric-drug/gene/dyes delivery device.

### 4. Self-assembly limitations

Self-assembly is most often used to create 1-, 2-, or 3- dimensional structures with nanometer resolution. Amphiphilic micelles, quantum dots, bilayer membranes, and photonic crystals are common examples of such structures. However, how can these nanometer scale elements be used to create macroscopic structures or devices with sizes on the order of micrometers to meters? In order for self-assembly to be used industrially at larger scales, it needs to be able to assemble nano-, micro-, and milli-meter scales parts into macroscopic 3-dimensional devices.

Self-assembly has showed promise as one of the elements required to build devices such as quantum computers, light-emitting diodes, and biosensors. However, fabricating such devices may not be limited to self-assembled parts and self-assembly processes. Other fabrication methods such as photo or soft lithography are often used together with self-assembly fabrication methods to create functional devices. Therefore, at the current stage of research, the bottom-up self-assembly process is often used as a sub-process due to the complex nature of microelectronic and biomedical devices. For example, the fabrication of microfluidic devices for sensor applications may incorporate the deposition of SAMs as one fabrication step to chemically alter the substrate's surface, while photolithography would be used to prepare the electrode pattern. Exposure of a light-sensitive material (photoresist layer) and development, i.e. removal of the exposed or non-exposed parts of

the photoresist film, leads to electrode patterned surfaces. Contact printing using an elastomer stamp and combined with chemical etching has been the other preferred method.

Of particular interest here, Whitesides and coworkers have reported in the literature that they have assembled macroscopic 3-dimensional objects/devices using forces besides those used for molecular self-assembly[61]. In particular, macroscopic systems have been self-assembled using capillary, magnetic, and electrical activation forces. Of interest, is the fact that these interactions are longer range than those characterizing intermolecular forces (hydrogen bond, van der Waals and hydrophobic interactions). Conventional photolithography was often used as part of the fabrication process to obtain these macroscopic self-assembled systems.

An alternative to lithography has been envisioned by Drexler as the concept of *molecular manufacturing*, which has become a famous controversy concerning self-assembly limitations. *Molecular manufacturing* proposes to use mechanosynthesis to build complex structures, where nanobot and molecular machines would be used to position molecules, control reactions, and build-up structures. The precise positioning of xenon atoms on a nickel surface was demonstrated by IBM in 1989, when *IBM* was spelled out with xenon atoms using a Scanning Tunneling Microscope (STM) tip. Atomic Force Microscope (AFM) has also been used later for demonstrating the same atomic positioning ability but on nonconducting surfaces[62]. The important limitation suggested by others is mostly known as the *fat and sticky fingers*, which argue that atomic precision placement can not be obtained due to the size of whatever medium is used to displace atoms and due to atom's reactivity.

Another proposal to create macroscopic self-assembled materials has been to use bioreactors to synthesize functional materials. Cellulose produced by bacteria has been used to fabricate soft cellulose tubes of various diameters that are currently being tested for vascular graft applications[63]. Varying shaking velocity and oxygen concentration during bacteria cultivation were found to affect the mechanical properties of the cellulose

tubes. The bacterial cellulose tubes exhibited burst pressure and tensile properties similar to those of natural blood vessels. The capability of using bacteria colonies to produce materials with desired mechanical and geometrical properties is of great interest for the creation of cost-effective artificial grafts with desired geometry and shape.

### C. *Polyethylene glycol-PEG: a protein resistant polymer*

#### 1. PEG's physical and chemical characteristics

Among biomaterials, polyethylene glycol (PEG) is particularly interesting due to its unique ability to repel proteins without denaturing them, its extremely high water solubility, and its availability in different molecular weights. Also, the hydroxyl groups at its chain ends render this polymer very attractive as chemical reactions with other molecules or substrates may easily be carried out.

Polyethylene glycols-PEGs- or polyethylene oxides-PEOs- are commercially available with molecular weights ranging from 200 to several million. Traditionally, PEG is used to refer to the polymers with a molecular weight below 20 000 g/mol, while PEO usually corresponds to those with a molecular weight larger than 20 000 g/mol. PEGs have low melting temperatures ranging from -65°C for PEG 200 (200 g/mol) to 63°C for PEG 8000. Even for the highest molecular weight PEGs (several millions in molecular weight), the melting temperature only reaches a maximum of 70°C. PEG has a very flexible backbone $(CH_2CH_2O)_x$ that readily crystallizes. In the crystalline state, PEG chains are arranged in a monoclinic crystal structure of dimensions a=7.96 Å, b=13.11 Å, c=19.39 Å, and β=124°48'. This monoclinic unit cell is comprised of 4 PEG chains, each one comprised of 7 monomer units, $(CH_2CH_2O)$, and 2 helical turns. This yields a monomer unit size averaging 2.77 Å in length, which is consistent with values reported in the literature. PEG crystallinity increases with increasing molecular weight and PEG's state at room temperature goes from liquid to waxy solid, to crystalline powder. When PEG is mixed with water, the crystals melt due to high PEG-water dissolution. This also

unusually occurs for the very high molecular weights that are highly crystalline. Therefore, PEG is recognized for its interesting solubility and swelling properties in water but also in several organic solvents such as benzene, e.g. the interaction between PEG units and water is characterized by the formation of several hydrogen bonds between water molecules and the ether group, and the number of these interactions per ether group appears to vary depending on several factors[64]. It is believed that a monohydrate and up to trihydrate may be formed by water molecules around one PEG unit. PEG-water association may change with PEG molecular weight, water content and temperature.

Traditionally, PEG has been introduced into or on materials via several methods, the goal being to reduce protein adsorption. Copolymers comprised of PEG either as branches attached to the backbone or as part of the backbone, and PEG grafted at the surface of materials have been the preferred methods for modifying materials properties. Specifically, reducing protein and cell adsorption and therefore improving blood compatibility of PEG-containing materials has been the main motivation behind modifying surfaces with PEG. While adding PEG into a block or graft copolymer formulation may modify the bulk properties of a given material, grafting PEG molecules onto a surface only affects the surface properties of a given material, conserving the bulk's properties. Grafted PEG also allows increasing PEG concentration at the surface of a material, which is where various cells and proteins may adsorb. Because this dissertation focuses on the study of surfaces modified with linear and star-shaped PEG derivatives, this section focuses on the work that has been done with PEGylated surfaces relevant to protein adsorption.

### 2. PEG tethered to surfaces lowers protein adsorption

#### *a) PEG-modified surfaces*

PEG has been recognized as a biomaterial because it minimizes interactions with proteins and cells[64]. This makes it highly attractive for fouling-resistant material surfaces. This

anti-fouling property has been attributed to the steric repulsion arising from the compression of the PEG chains when a protein or a cell is approaching a PEG-modified surface[65, 66]. Other biological systems such as bacteria have also been found to resist adsorption on PEG-modified surfaces as well. The efficiency of PEGylated surfaces to resist protein adsorption was found to vary according to PEG chains length, PEG chains grafting density, and the size of the approaching molecule. Details on the factors influencing PEG's ability to repel proteins will be outlined in Section C.3.

*b) Tethered PEG: linear vs. star-shaped molecules*

Different PEG molecules with various architectures have been tethered to surfaces and their ability to repel proteins has been studied. These architectures have included linear and star-shaped PEG molecules[67, 68]. As illustrated in Figure 1.6, star molecules are usually formed by the junction of various linear molecules which are referred to as the star arms. This junction forms the star core with arms extending out from the higher density core.

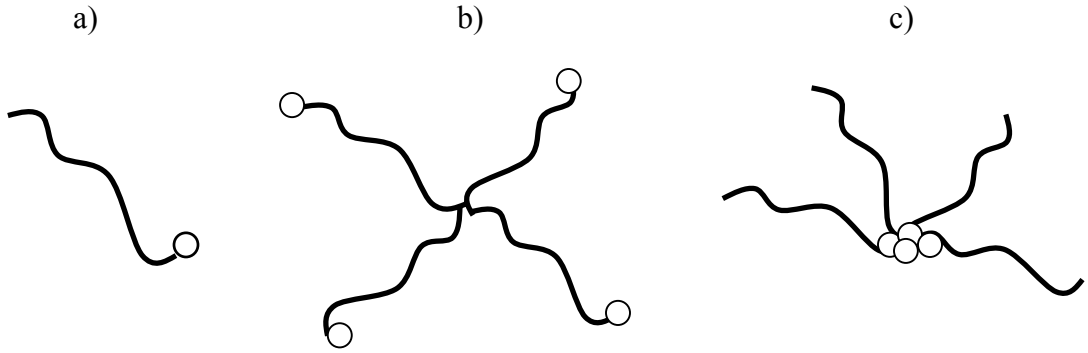


**Figure 1.6: a) a linear PEG molecule, b) an end-functionalized 4-arm PEG star, and c) a core-functionalized 4-arm PEG star. The circles represent either end or core functional groups by which the molecules may tether to surfaces.**

Although end-functionalized star molecules are more common, core functionalized stars may lead to different film architecture than end-functionalized star molecules due to different anchor points. In both cases, stars are characterized by large number of functionalities (end groups) in a small volume. By definition, star molecules have an

increased number of chains per unit volume comparative to linear molecules. Although star-shaped molecules have been of great interest due to their specific rheological and diffusion properties, they have offered great potential to increase surface biocompatibility due to their high functional density. The motivation behind comparing star versus linear molecules with respect to their protein repulsion properties has been to increase PEG chains surface density using star molecules. Star molecules may have very high PEG densities, i.e. up to more than 70 arms. This particular structure type is thought to create hard-sphere like molecules due to the steric hindrance arising from the large number of arms in a small area.

Irvine and coworkers[68] compared protein adsorption on 2 tethered linear PEG molecules of respectively 10 000 (*linear 1*) and 20 000 g/mol (*linear 2*) molecular weights to 2 tethered PEG star molecules. The first stars were comprised of 24 arms, with the molecular weight of each arm being 9700 g/mol. The second stars were formed of 72 arms, with the molecular weight of each arm being 4500 g/mol. The total molecular weight of these stars was therefore 233 000 (*star 1*) and 360 000 g/mol (*star 2*), respectively. A schematic of *linear 1* and *star 1* is showed in Figure 1.7. Neutron reflectivity and ellipsometry measurements were performed to study the density and protein adsorption of these tethered linear and star molecules in the hydrated state. The grafting density or surface coverage was maximized for both the tethered linear and star PEG molecules. As expected, the grafting density for both tethered stars (0.14 and 0.37 chain/nm$^2$ for stars 1 and 2, respectively) was found to be significantly higher than that for both linear molecules (0.09 and 0.06 chain/nm$^2$ for linear 1 and 2, respectively). Both linear and star tethered PEG molecules significantly reduced albumin (68 000 g/mol) and cytochrome-c (12 000 g/mol) adsorption after 4 hours of immersion. It was proposed that the very large density of the stars core forces the extension of arms, increasing the PEG segment density away from the substrate, while lowering it near the substrate. Therefore, although the stars are overlapping, protein adsorption may occur between the stars near the substrate, where the PEG segment density is lower. Contrarily, tethered linear molecules, which were also overlapping, presented higher PEG segment density near the substrate and better resisted protein adsorption.

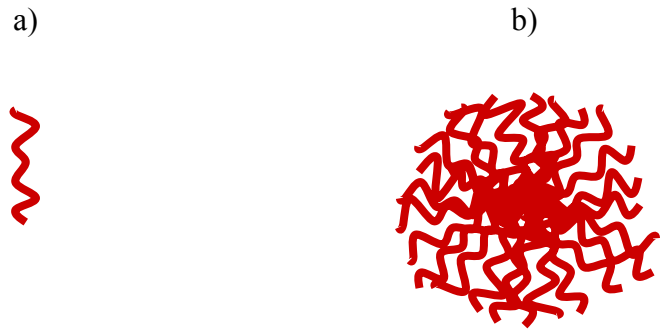


**Figure 1.7: a) a linear PEG molecule similar to linear 1 (see text) and b) a 24-arm star molecule similar to star 1 (see text). The molecular weight of each arm of the 24-arm star is equivalent to the molecular weight of 1 linear PEG chain.**

Sofia *et al*[67] have studied albumin, cytochrome-c, and fibrinogen (500 000 g/mol) adsorption on grafted linear and star-shaped PEG molecules based on X-Ray Photoelectron Spectroscopy (XPS) and ellipsometry measurements. Linear PEG molecules with molecular weights of 3400, 10 000, and 20 000 g/mol (*linear 1*, *2*, and *3* respectively) were used. The PEG stars were very similar to those studied by Irvine[68] and exhibited hard sphere-like structures as well. *Star 1* had 20 arms of 10 000 g/mol each, and *star 2* had 70 arms of 5200 g/mol each, corresponding to 200 000 and 350 000 g/mol overall molecular weight for *star 1* and *2*, respectively. As in the previous study, these stars were end-functionalized and tethered on silicon wafers. In agreement with Irvine's study[68], grafting densities for grafted linear PEG molecules increased as the molecular weight decreased from 20 000 to 3400 g/mol due decreased excluded volume for shorter PEG chains. *Linear 1*, *2*, and *3* reached a maximum grafting density close to 0.18, 0.06, and 0.03 chain/nm$^2$ respectively, which is slightly below the surface densities reported by Irvine[68] but still corresponding to a linear chains overlapping structure. However, the grafting density of both tethered stars was lower by 2 orders of magnitude than the stars grafting densities obtained by Irvine. These lower grafting densities implied that the tethered star molecules were weakly overlapping. Protein adsorption was allowed for 24 hours, which is significantly higher than the previous study. It was found that linear PEG tethered molecules reduced all protein adsorption especially when

the grafting density was close to the maximum obtained values. However, even at the highest achieved grafting densities, tethered PEG stars adsorbed proteins, especially the smallest one, cytochrome-c. This was justified by the lack of stars overlap, which created spacing between star molecules allowing adsorption.

From both of these studies, it is implied that highly overlapping chains are necessary to fully repel proteins for both linear and star-shaped PEG molecules.

## 3. Protein adsorption models for PEGylated surfaces

### *a) PEG molecular weight, grafting density, and conformation effects*

Jeon and coworkers[65, 66] theoretically studied protein resistance of PEG molecules (~100 monomer-long) grafted on a hydrophobic surface and in the brush structure. The brush structure is defined to be when the PEG layer thickness is superior to the radius of gyration, $R_G$, of these PEG chains. This was found to be true as $R_G$ for PEG with ~100 monomers is around 3nm, and as PEG thickness was around 8nm. The change in free energy of the PEGylated surface-protein interface determines protein adsorption or protein repulsion. This change in free energy of the interface was considered to be the sum of the free energies arising from steric repulsion and hydrophobic attractions between the advancing protein and the PEGylated surface. The short-range van der Waals interactions were neglected because outweighed by the long-range hydrophobic interactions. The steric repulsion free energy had osmotic and elastic contributions. From these free energy calculations, it was concluded that PEG surface density and chain length are important factors accounting for protein repulsion, and that high PEG surface density is especially important for repelling smaller proteins.

Prime and Whitesides[29] designed mixed SAM comprised of a densely packed (pseudocrystalline) hydrophobic moiety attached to a gold surface via thiol molecules, and comprised of hydrophilic oligo(ethylene oxide) chains. These ethylene oxide chains had between 1 and 17 monomers. The linear PEG molecules studied by Irvine[68] had a

minimum of 227 monomer units up to 466 units corresponding to 10 000 and 20 000 g/mol, respectively. All the proteins tested by Prime and Whitesides were significantly larger than the size of the PEG chains and a 2 hour adsorption was allowed. This SAM structure was designed to model a hydrophobic surface modified by flexible and randomly oriented PEG chains in order to compare their data to Jeon's previous studies[65, 66]. It was found that while shorter PEG chains needed higher grafting densities to successfully repel proteins, longer PEG chains needed lower surface densities to resist protein adsorption. The terminal group present on the PEG chains had no effect on protein repulsion properties, as no difference was noticed between the behavior of hydroxyl and methyl end groups. With a protein adsorption time of 2 hours, only 2 ethylene oxide monomers were found to repel fibrinogen, pyruvate kinase, lysosome, and ribonuclease A proteins given a sufficient PEG surface concentration. However, the zero protein adsorption reported is relative to the rinsing and nitrogen flow drying step.

Wang and coworkers[69] have studied the effects of various PEG conformations on protein adsorption. Small molecular weight PEG moieties of mixed SAMs were used. 2 conformations were considered: the helical and the planar. The helical conformation of PEG exists both in the crystalline and aqueous solution (at least locally) states of the polymer. The helical structure exhibits a *trans-gauche-trans* (*tgt*) conformation of the PEG backbone (C-C-O), where the *gauche* angle is rotated uniformly compared to the -C-C-O plane over the length of the helix, either clock- or counter clock- wise. An amorphous structure may arise from *gauche* defects, which are gauche angles that differ from those characteristic of the crystalline structure. It is known that the concentration of gauche defects affect the length of the chain length. Random coil conformations have a significantly large concentration of gauche defects. Contrarily, the planar *all-trans* conformation (*ttt*) corresponds to a stretched planar structure, occurring for instance when PEG chains are fully extended due to higher grafting densities. Wang *et al*[69] found that the PEG crystalline helical conformation forms stronger hydrogen bonds with the water molecules, whereas the planar structure allows for weaker hydrogen bonds. The crystalline helical PEG chains conformation was found to repel proteins. Therefore, conformationally flexible PEG chains may not be a necessary condition for PEG protein

resistance. Harder and coworkers[70] compared fibrinogen adsorption on crystalline helical, amorphous, and planar conformations of oligo(ethylene oxide)-terminated SAMs comprised of 3 or 6 ethylene oxide units. They found that the SAMs deposited on gold and comprised of 6 ethylene oxide units with a hydroxyl end group exhibited increased crystallinity (densely packed helices) when immersion time was 2 hours. However, when immersion time was decreased to 1 min, amorphous conformations occurred due to higher gauche defect concentration. Both the densely packed crystalline helical and the amorphous conformations for these SAMs were resistant to fibrinogen adsorption after 15 min of immersion in the protein solution. However, the planar zig-zag conformation adsorbed fibrinogens.

This section has emphasized the importance of several factors that may play a role in the ability of PEGylated surfaces to repel proteins in solution. These factors include the thickness of the grafted PEG chains (number of ethylene glycol monomers), PEG surface density (grafting density), and PEG conformation (dense brush, intermediate brush, planar zig-zag, amorphous, and crystalline helical conformations). These factors may be interdependent such as increasing PEG surface density leads to overlapping brush conformation.

Although PEG is an attractive and recognized biocompatible polymer, the mechanisms involved in its resistance to adsorb biological molecules such as proteins are not yet fully understood. Possible mechanisms are outlined next.

*b) Possible mechanisms responsible for protein adsorption resistance*

Lee and coworkers reported that several factors may play a role in the protein-resistant properties of PEG-modified surfaces[71]. These include PEG's minimal interfacial free energy with water, PEG's steric stabilization, and the unique solution properties of PEG in water. PEG's interfacial free energy with water is minimal. This results in a low driving force for non specific protein adsorption. Other polymers exhibit similar interfacial free energy (i.e. low water contact angle or hydrophilic properties) although

their protein resistance properties are less than those of PEG. Steric repulsion is generally related to a neutral and hydrophilic polymer in aqueous solution. PEG's steric stabilization arises from the change in Gibbs free energy occurring at the protein-PEG interface. As mentioned earlier in Section A. 3. c), if $\Delta G>0$ adsorption will not take place spontaneously, but if $\Delta G<0$ spontaneous adsorption will occur. The distinction between 2 types of steric effects is made. First, a volume restriction effect is based on a conformational entropy loss due to a compression by an approaching protein for instance. Fewer chain configurations are thus available for these compressed chains, which makes protein adsorption unfavorable. This decrease in entropy leads to a $\Delta G$ increase due to:

$$\Delta G = -T\Delta S \tag{6}$$

where $\Delta G$ is the Gibbs free energy change at the PEG-protein interface, $T$ is the temperature, and $\Delta S$ is the entropy change at the same interface. The enthalpy change is neglected in this case.

Also, steric effects may be characterized by an excluded-volume effect based on osmotic pressure repulsion, where the PEG and protein are allowed to overlap. This overlap creates an enthalpy of mixing $\Delta H$ (i.e. change in PEG-water mixing), and together with the decreased conformational entropy, it contributes to increasing $\Delta G$. This increased free energy ( $\Delta G = \Delta H - T\Delta S$ ) is also unfavorable to protein adsorption. Lee and coworker pointed out that steric repulsion may not entirely explain PEG protein resistance because other neutral and hydrophilic grafted polymers exhibit poorer protein resistance[71]. Finally, a third factor is considered, i.e. PEG aqueous solution properties related to PEG chains mobility in water. The mobility of hydrated PEG chains has been found to increase with PEG chains length up to 100.

Dipole relaxation measurements and Nuclear Magnetic Resonance (NMR) proton relaxation rate studies have been performed to study the mobility of PEG dissolved in water solutions[72]. It was found that longer PEG chains, i.e. with chain lengths superior to ~100, have relaxation rates that are not affected by end group dynamics. However,

shorter PEG chain's relaxation rates may be affected by end group contributions. Additionally, PEG chains with chain lengths superior to ~100 were found to have segmental motions that were independent of PEG molecular weight. On the contrary, smaller molecular weights had relaxation rates that depended on end group dynamics. Segmental motions may also depend on PEG chain length. Thus, generally, PEG chains with chain lengths superior to ~100 have higher mobility and this mobility is independent of molecular weights[72, 73]. Note that similar mobility trends were found for hydrated PEG films, meaning that grafted PEG chains may relax similarly than unattached PEG chains in aqueous solution. Below chain length of ~100, mobility (or relaxation rates) may be lower and generally depends on PEG molecular weight and end group dynamics.

**References:**


1. Ratner, B. D., *Biomaterials science: an introduction to materials in medicine*, ed. B. D. Ratner. 2004: Elsevier Academic Press.
2. Weser, U.; Kaup, Y.; Etspüler, H.; Koller, J.; Baumer, U., *Embalming in the Old Kingdom of pharaonic Egypt.* Analytical Chem., 1998. **70**: p. 511A-516A.
3. Artico, M.; Ferrante, L.; Pastore, F. S.; Ramundo, E. O.; Cantarelli, D.; Scopelliti, D.; Iannetti, G., *Bone autografting of the calvaria and craniofacial skeleton historical background, surgical results in a series of 15 patients, and review of the literature* Surgical Neurology, 2003. **60**: p. 71-79.
4. Davis, J. S., *Plastic Surgery in World War I and in World War II* Ann. Surg., 1946. **123**: p. 610–621.
5. Anderson, J. M.; Cook, G.; Costerton, B.; Hanson, S. R.; Hensten-Pettersen, A.; Jacobsen, N.; Johnson, R. J.; Mitchell, R. N.; Pasmore, M.; Schoen, F. J.; Shirtliff, M.; Stoodley, P., *Host Reactions to Biomaterials and Their Evaluation*, in *Biomaterials Science*, B.D. Ratner, Hoffman, A. S.; Schoen, F. J.; Lemons, J. E., Editor. 2004, Academic Press. p. 293-354.
6. Ball, V.; Schaaf, P.; Voegel, J.-C., *Mechanism of Interfacial Exchange Phenomena for Proteins Adsorbed at Solid-Liquid Interfaces*, in *Biopolymers at interfaces*, M. Malmsten, Editor. 2003, Marcel Dekker, Inc.
7. Basmadjian, D.; Sefton, M.; Baldwin, S., *Coagulation on biomaterials in flowing blood: some theoretical considerations.* Biomaterials, 1997. **18**: p. 1511-1522
8. Michal, G., *Blood Coagulation and Fibrinolysis*, in *Biochemical Pathways*, G. Michal, Editor. 1999, Wiley Spektrum. p. 251-257.
9. Derand, H.; Malmsten, M., *Protein Interfacial Behavior in Microfabricated Analysis Systems and Microarrays*, in *Biopolymers at interfaces*, M. Malmsten, Editor. 2003, Marcel Dekker, Inc.
10. Norde, W., *Driving Forces for Protein Adsorption at Solid Surfaces*, in *Biopolymers at interfaces*, M. Malmsten, Editor. 2003, Marcel Dekker, Inc. p. 21-44.
11. Bordbar, A.-K.; Sohrabi, N.; Gharibi, H., *Binding Set Analysis for Interaction of Human Serum Albumin with Cethyl Trimethylammonium Bromide.* Bull. Korean Chem. Soc., 2004. **25**: p. 791-795.
12. Akkas, P.; Sari, M.; Sen, M.; Guven, O., *The effect of external stimuli on the Bovine Serum Albumin adsorption capacity of poyl(acrylamide/maleic acid) hydrogels prepared by gamma rays.* Radiation Physics and Chemistry, 1999. **55**: p. 717-721.
13. Su, T. J.; Lu, J. R.; Thomas, R. K.; Cui, Z. F., *Effect of pH pn the Adsorption of Bovine Serum Albumin at the Silica/Water Interface Studied by Neutron Reflection.* J. Phys. Chem. B, 1999. **103**: p. 3727-3736.
14. Li, S.; Hu, J.; Liu, B., *A study on the adsorption behavior of protein onto fonctional microspheres.* J. Chem. Technology & Biotechnology, 2005. **80**: p. 531-536.
15. Thierry, B., *Bioactive Coatings of Endovascular Stents Based on Polyelectrolyte Multilayers.* Biomacromolecules, 2003. **4**: p. 1564-1571.

16. Hardhammar, P. A.; Van Beusekom, H. M. M.; Albertsson, P. A.; Verdouw, P. D.; Boersma, E.; Serruys, P. W.; Van der Giessen, W. J., *Reduction in thrombotic events with heparin-coated Palmaz-Schatz stents in normal porcine coronary arteries.* Circulation, 1996. **93**: p. 423-430.
17. Rogers, C.; Welt, F. G. P.; Karnovsky, M. J.; Edelman, E. R., *Monocyte recruitment and neointimal hyperplasia in rabbits Coupled inhibitory effects of heparin.* Arteriosclerosis, Thrombosis, and Vascular Biology, 1996. **16**: p. 1312-1318.
18. Raizner, A. E.; Oesterle, S. N.; Waksman, R.; Serruys, P. W.; Colombo, A.; Lim, Y.-L.; Yeung, A. C.; Van der Giessen, W. J.; Vandertie, L.; Chiu, J. K.; White, L. R. ; Fitzgerald, P. J.; Kałuz, G. L.; Ali, N. M., *Inhibition of Restenosis With b-Emitting Radiotherapy Report of the Proliferation Reduction With Vascular Energy Trial.* Circulation, 2000. **102**: p. 951-958.
19. Klugherz, B. D.; Jones, P. L.; Cui, X.; Chen, W.; Meneveau, N. F.; DeFelice, S.; Connolly, J.; Wilensky, R. L.; Levy, R. J., *Gene delivery from a DNA controlled release stent in porcine coronary arteries.* Nature biotechnology, 2000. **18**: p. 1181- 1184.
20. Berry, J. L.; Yazdani, S. K., *Vessel wall stress created by thin strut versus thick strut stents.* Am. J. Cardiol., 2004. **94**: p. 156E.
21. Rolland, P. H.; Mekkaoui, C.; Vidal, V. ; Berry, J. L.; Moore, J. E.; Moreno, M.; Amabile, P.; Bartoli, J. M., *Compliance matching stent placement in the carotid artery of the swine promotes optimal blood flow and attenuates restenosis.* Eur. J. Vasc. Endovasc. Surg., 2004. **28**: p. 431-438.
22. Vienken, J., *Polymers in nephrology: Characteristics and needs* The Intern. J. of Artif. Organs, 2002. **25**: p. 470-479.
23. Higuchi, A.; Shirano, K.; Harashima, M.; Yoon, B. O.; Hara, M.; Hattori, M.; Imamura, K., *Chemically modified polysulfone hollow fibers with vinylpyrrolidone having improved blood compatibility* Biomaterials, 2002. **23**: p. 2659-2666.
24. Elam, J. H.; Karlsson, C.; Nygren, H., *Pre-adsorption of a cellulose ether onto polymer surfaces: adsorption of adhesins and platelet activation* Biomaterials, 1993. **14**: p. 233-237.
25. Renugopalakrishnan, V.; Lewis, R. V., *Bionanotechnology*, ed. V. Renugopalakrishnan, Lewis, R. V. 2006: Springer.
26. Langmuir, I., *The Constitution and fundamental properties of solids and liquids. II. Liquids.* J. Am. Chem. Soc. , 1917. **39**: p. 1848-1906.
27. Langmuir, I., *The Mechanism of the Surface Phenomena of Flotation.* Trans. Faraday Soc., 1920. **15**: p. 62-74.
28. Hamachi, I.; Noda, S.; Kunitake, T., *Layered Arrangement of Oriented Myoglobins in Cast Films of a Phosphate Bilayer Membrane.* J. Am. Chem. Soc., 1990. **112**: p. 6744-6745.
29. Prime, K. L.; Whitesides, G. M., *Adsorption of proteins onto surfaces containing end-attached oligo(ethylene oxide): A model system using self-assembled monolayers.* J. Am. Chem. Soc., 1993. **115**: p. 10714-10721.
30. Ventra, M. D.; Evoy, S.; Heflin, J. R. Jr., *Introduction to Nanoscale Science and Technology*, ed. M.D. Ventra, Evoy, S.; Heflin, J. R. Jr. 2004: Springer.

31. Decher, G.; Hong, J. D.; Schmitt, J., *Buildup of ultrathin multilayer films by self-assembly process: III. Consecutively alternating adsorption of anionic and cationic polyelectrolytes on charged surfaces* Thin Solid Films, 1992. **210-211**: p. 831-835.
32. Iler, R. K., *Multilayers of Colloidal Particles.* J. Colloid Inter. Sci. , 1966. **21**: p. 569-594.
33. Liu, Y.; Claus, R. O., *Layer-by-Layer Electrostatic Self-Assembly of Nanoscale Fe304 Particles and Polyimide Precursor on Silicon and Silica Surfaces.* Appl. Phys. Lett., 1997. **71**: p. 2265-2267.
34. Wang, Y.-X.; Du, W.; Spillman, W. B., Jr.; Claus, R. O., *Biocompatible thin film coatings fabricated using the electrostatic self-assembly process.* Proceedings of SPIE, 2001: p. 142-151.
35. Lvov, Y.; Decher, G.; Sukhorukov, G., *Assembly of Thin Films by Means of Successive Deposition of Alternate Layers of DNA and Poly(allylamine).* Macromolecules, 1993. **26**: p. 5396-5399.
36. Keller, S. W.; Kim, H.-N.; Mallouk, T. E., *Layer-by-Layer Assembly of Intercalation Compounds and Heterostructures on Surfaces: Toward Molecular "Beaker" Epitaxy.* J. Am. Chem. Soc., 1994. **116**: p. 8817-8818.
37. Feldheim, D. L.; Grabar, K. C.; Natan, M. J.; Mallouk, T. E., *Electron Transfer in Self-Assembled Inorganic Polyelectrolyte/Metal Nanoparticle Heterostructures.* J. Am. Chem. Soc., 1996. **118**: p. 7640-7641.
38. Liu, Y. W.; Y.-X.; Claus, R. O., *Layer-by-layer ionic self-assembly of Au colloids into multilayer thin-films with bulk metal conductivity.* Chem. Phys. Lett., 1998. **298**: p. 315-319.
39. Eckle, M.; Decher, G., *Tuning the Performance of Layer-by-Layer Assembled by Controlling the Position of Isolating Clay Barrier Sheets* Nano Letters, 2001. **1**: p. 45-49.
40. Kunitake, T., *Anisotropic Incorporation of Functional Molecules and Synthesis of Low-Dimensional Clusters in Cast Multibilayer Films.* Mol. Cryst. Liq. Cryst. , 1994. **255**: p. 7-16.
41. Lvov, Y.; Decher, G.; Mohwald, H., *Assembly, Structural Characterization, and Thermal Behavior of Layer-by-Layer Deposited Ultrathin Films of Poly(vinyl sulfate) and Poly(allylamine).* Langmuir, 1993. **9**: p. 481-486.
42. Schmitt, J.; Grunewald, T.; Decher, G.; Pershan, P. S.; Kjaer, K.; Losche, M. , *Internal Structure of Layer-by-Layer Adsorbed Polyelectrolyte Films: A Neutron and X-Ray Reflectivity Study.* Macromolecules, 1993. **26**: p. 7058-7063.
43. Reed, M. A.; Zhou, C.; Muller, C. J.; Burgin, T. P.; Tour, J. M., *Conductance of a Molecular Junction.* Science, 1997. **278**: p. 252-254.
44. Salomon, A.; Cahen, D.; Lindsay, S.; Tomfohr, J.; Engelkes, V. B.; Frisbie, D., *Comparison of Electronic Transport Measurements on Organic Molecules.* Adv. Mater. , 2003. **15**: p. 1881-1890.
45. Selzer, Y.; Salomon, A.; Cahen, D., *The Importance of Chemical Bonding to the Contact for Tunneling through Alkyl Chains.* J. Phys. Chem. B, 2002. **106**: p. 10432-10439.

46. Beebe, J. M.; Engelkes, V. B.; Miller, L. L.; Frisbie, C. D., *Contact Resistance in Metal-Molecule-Metal Junctions Based on Aliphatic SAMs: Effects of Surface Linker and Metal Work Function.* J. Am. Chem. Soc., 2002. **124**: p. 11268-11269.
47. Liu, Y.-L.; Yu, H.-Z., *Alkyl Monolayer-Passivated Metal ±Semiconductor Diodes: Molecular Tunability and Electron Transport.* ChemPhysChem, 2002. **3**: p. 799-802.
48. Ringler, P.; Schulz, G. E., *Self-Assembly of Proteins into Designed Networks.* Science, 2003. **302**: p. 106-109.
49. Jiang, X.; Ferrigno, R. ; Mrksich, M.; Whitesides, G. M., *Electrochemical Desorption of Self-assembled Monolayers Noninvasively Releases Patterned Cells from Geometrical Confinements.* J. Am. Chem. Soc., 2003. **125**: p. 2366-2367.
50. Di, V. M.; Zolak, M., *DNA electronics*, in *Encyclopedia of Nanoscience and Nanotechnology*, H.S. Nalwa, Editor. 2004, American Scientific Publisher.
51. Sánchez-Pomales, G.; Rivera-Vélez, N. E.; Cabrera, C. R., *DNA-mediated self-assembly of carbon nanotubes on gold.* J. Phys. Conference Series, 2007. **61**: p. 1017–1021.
52. Tamm, L. K.; McConnell, H. M., *Supported Phospholipid Bilayers.* Biophys. J., 1985. **47**: p. 105-113.
53. Cremer, P. S.; Boxer, S. G., *Formation and spreading of lipid bilayers on planar glass surfaces.* J. Phys. Chem. B., 1999. **103**: p. 2554-2559.
54. Yang, T.; Jung, S. Y.; Mao, H.; Cremer, P. S. , *Fabrication of phospholipid bilayer coated microchannels for on chip immunoassays.* Analytical Chem., 2001. **73**: p. 165-169.
55. Castellana, E. T.; Cremer, P. S., *Solid supported lipid bilayers: From biophysical studies to sensor design.* Surface Science Reports, 2006. **61**: p. 429–444.
56. Kang, X.-F.; Cheley, S.; Rice-Ficht, A. C.; Bayley, H., *A Storable Encapsulated Bilayer Chip Containing a Single Protein Nanopore.* J. Am. Chem. Soc., 2007. **129**: p. 4701-4705.
57. Kwon, G. S.; Okano, T., *Polymeric micelles as new drug carriers.* Advanced Drug Delivery Reviews, 1996. **21**: p. 107-116.
58. Nishiyama, N.; Kataoka, K., *Nanostructured Devices Based on Block Copolymer Assemblies for Drug Delivery: Designing Structures for Enhanced Drug Function.* Adv. Polym. Sci., 2006. **193**: p. 67–101.
59. Taillefer, J.; Jones, M.; Brasseur, N.; Van Lier, J. E.; Leroux, J., *Preparation and characterization of ph-responsive polymeric micelles for the delivery of photosensitizing anticancer drugs.* J. Pharm. Sci., 2000. **89**: p. 52–62.
60. Haag, R., *Supramolecular drug-delivery systems based on polymeric core-shell architectures.* Angew. Chem. Int. Ed. Engl., 2004. **43**: p. 278-282.
61. Boncheva, M.; Bruzewicz, D. A.; Whitesides, G. M., *Millimeter-scale self-assembly and its applications.* Pure Appl. Chem., 2003. **75**: p. 621-630.
62. Oyabu, N.; Custance, O.;Yi, I.; Sugawara, Y.; Morita, S., *Mechanical Vertical Manipulation of Selected Single Atoms by Soft Nanoindentation Using Near Contact Atomic Force Microscopy.* Phys. Rev. Lett., 2003. **90**: p. 1761021-1761024.

63. Bodin, A.; Backdahl, H.; Fink, H.; Gustafsson, L.; Risberg, B.; Gatenholm, P., *Influence of Cultivation Conditions on Mechanical and Morphological Properties of Bacterial Cellulose Tubes.* Biotechnol. Bioeng., 2007. **97**: p. 425–434.
64. Harris, J. M., *Poly(ethylene glycol) chemistry: biotechnical and biomedical applications*, ed. J.M. Harris. 1992: Plenum Press.
65. Jeon, S. I.; Lee, J. H.; Andrade, J. D.; De Gennes, P. G., *Protein-Surface Interactions in the Presence of Polyethylene Oxide. I. Simplified Theory.* J. Colloid Interface Sci., 1991. **142**: p. 149-158.
66. Jeon, S. I.; Andrade, J. D., *Protein-Surface Interactions in the Presence of Polyethylene Oxide. II. Effect of Protein Size.* J. Colloid Interface Sci., 1991. **142**: p. 159-166.
67. Sofia, S. J., Premnath, V.; Merrill, E. W., *Poly(ethylene oxide) Grafted to Silicon Surfaces: Grafting Density and Protein Adsorption.* Macromolecules, 1998. **31**: p. 5059-5070.
68. Irvine, D. J.; Mayes, A. M.; Satija, S. K.; Barker, J. G.; Sofia-Allgor, S. J.; Griffith, L. G., *Comparison of tethered star and linear poly(ethylene oxide) for control of biomaterials surface properties.* J. Biomed. Mater. Res., 1998. **40**: p. 498-509.
69. Wang, R. L. C.; Kreuzer, H. J.; Grunze, M., *Molecular Conformation and Solvation of Oligo(ethylene glycol)-Terminated Self-Assembled Monolayers and Their Resistance to Protein Adsorption.* J. Phys. Chem. B, 1997. **101**: p. 9767-9773.
70. Harder, P.; Grunze, M.; Dahint, R.; Whitesides, G. M.; Laibinis, P. E., *Molecular Conformation in Oligo(ethylene glycol)-Terminated Self-Assembled Monolayers on Gold and Silver Surfaces Determines Their ability to Resist Protein Adsorption.* J. Phys. Chem. B, 1998. **102**: p. 426-436.
71. Lee, J. H.; Lee, H. B.; Andrade, J. D., *Blood compatibility of polyethylene oxide surfaces.* Prog. Polym. Sci. , 1995. **20**: p. 1043-1079.
72. Liu, K. J.; Ullman, R., *Proton Magnetic Relaxation in Polyethylene Oxide Solutions.* J. Chem. Phys., 1968. **48**: p. 1158-1168.
73. Hammes, G. G.; Roberts, P. B., *Cooperativity of Solvent-Macromolecule Interactions in Aqueous Solutions of Polyethylene Glycol and Polyethylene Glycol-Ureal.* J. Am. Chem. Soc., 1968. **90**: p. 7119-7122.

# CHAPTER II.

## ANALYTICAL TOOLS USED TO CHARACTERIZE MOLECULAR STRUCTURE & OVERLAYER THICKNESS, DENSITY, AND WETTABILITY

### A. *Nuclear Magnetic Resonance (NMR) Spectroscopy*

#### 1. Principles

The atomic nuclei of certain elements exhibit a magnetic moment due to the spins of protons and neutrons[1]. However, some nuclei like $^{12}C$ and $^{16}O$ have no magnetic moment although their nuclei are positively charged because of the cancellation of the proton and neutron spins. Thus, if the sum of the number of protons and neutrons of a nucleus is an odd number, or if both the number of protons and the number of neutrons are odd numbers, this nucleus will exhibit a magnetic moment. The former corresponds to a half-integer spin quantum number, while the latter corresponds to an integer spin quantum number. $^{1}H$, $^{13}C$, and $^{29}Si$ all have a spin equals to ½, while $^{12}C$ has a 0 spin. The nuclei that do not behave like a magnet have a spin quantum number equal to 0.

When there is no external magnetic field, the nuclei of a given "magnetic" element are randomly oriented, whereas whenever a static external magnetic field $B_0$ is applied, some nuclei align with the external field (low energy configuration), while others absorb some energy and orient themselves in opposite direction to the field (high energy configuration)[1]. The nuclei that are aligned with $B_0$ are in slight excess compared to those oriented in opposite direction to $B_0$. The difference in energy between these 2 energy levels $\Delta E$ depends on the element and corresponds to a particular frequency $\nu$ given by:

$$\Delta E = h\nu \qquad (1)$$

Figure 2.1 illustrates the general NMR spectrometer set-up and the magnetic nuclei orientations or configurations in the presence of an external field.

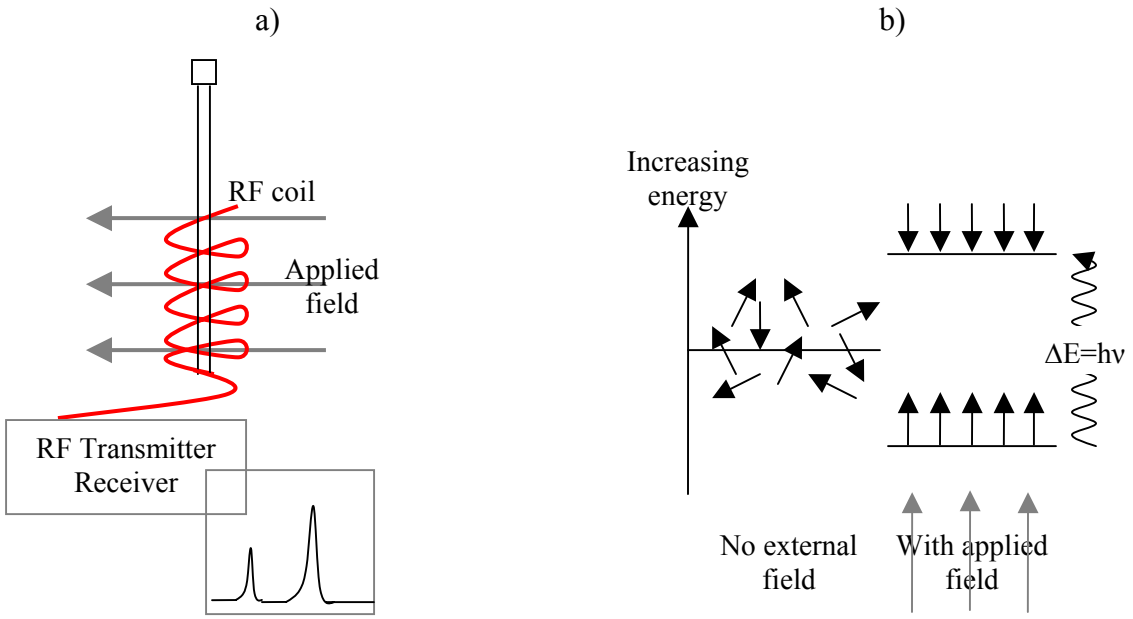


**Figure 2.1: a) General experimental set-up showing the applied static magnetic field and the RF coil through which an orthogonal field is applied, and b) radiofrequency energy absorption and emission by nuclei illustrating energy transitions between 2 orientations, i.e. aligned with and opposite to the applied external magnetic field.**

When this particular frequency *v* which is in the radiofrequency range is utilized as the irradiation source, these nuclei will be "in resonance" and absorption/emission transitions will occur. Thus these nuclei orientation will switch from being aligned with the field to being opposite and vice versa. Thus, with an external field of 9.39 T and at a radiofrequency of 400 MHz, the energy transition during proton ($^{1}$H) resonance will be detected, while at a frequency of 100 MHz, the transitions associated with $^{13}$C will be observed. The study of nuclear magnetic resonance (NMR) is concerned with these energy states and with the absorbed radiofrequency during resonance, which is detected by the NMR spectrometer.

2. Chemical shifts

Not all $^{13}C$ resonate at exactly 100 MHz, and not all $^{1}H$ resonate at 400 MHz in the presence of a 9.39 T external magnetic field. The direct chemical environment of these carbon and proton affects these nuclei resonance frequency by a few parts per million due to different electron densities that surround these nuclei. This corresponds to the phenomenon called "chemical shift", and constitutes the reason why NMR is used as an analytical tool to predict molecular structure[1]. While the 3 protons within a methyl group ($CH_3$) resonate at about 130 Hz (i.e. 1.3 ppm) above the proton resonant frequency of 400 MHz, a proton belonging to a hydroxyl group (OH) resonate at about 400 Hz (or 4 ppm) above 400 MHz. These chemical shifts are represented by peaks on an NMR spectrum as shown in Figure 2.2.

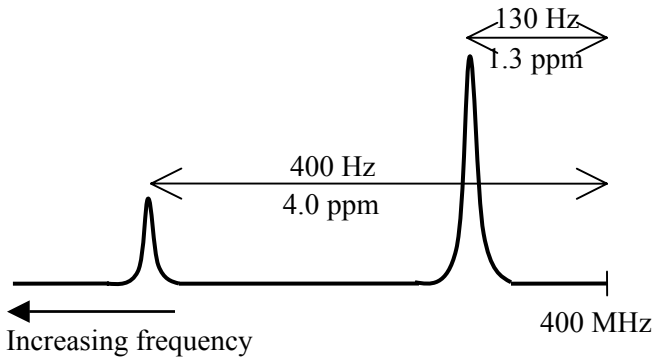


**Figure 2.2: Chemical shift for a proton NMR spectrum showing the methyl (CH3) protons shifted by 1.3 ppm while the hydroxyl (OH) protons are shifted by 4 ppm relatively to the resonant frequency of 400 MHz.**

Therefore, an NMR spectrum gives the radiofrequency absorption of proton, carbon, silicon and other magnetic nuclei as a function of frequency shift (Hz) or chemical shift (ppm). Additionally, signal intensity is proportional to the number of elements (protons for instance) within a molecule which have the particular chemical environment corresponding to this precise peak frequency or chemical shift. $^{1}H$ NMR is especially well suited for quantitative studies to determine molecular structures because $^{1}H$ has a 99.98% natural abundance, whereas $^{29}Si$ and $^{13}C$ only have 4.7 and 1.1%, respectively.

Additionally, nuclear spin gives rise to gyromagnetic ratio, which is the ratio between the nuclear magnetic dipole and the spin angular momentum. The natural abundance of a nucleus along with its gyromagnetic ratio determines the sensitivity of this nucleus. Consequently, if $^{1}H$ has a sensitivity of 1, $^{29}Si$ and $^{13}C$ would have an absolute sensitivity of $3.7x10^{-4}$ and $1.8x10^{-4}$, respectively[1]. This gives $^{1}H$ NMR the highest sensitivity, and therefore, proton NMR is one of the most appropriate nuclei for quantitative studies. Table 1 recapitulates some important nuclear magnetic properties for $^{1}H$, $^{29}Si$, and $^{13}C$ magnetic nuclei.

**Table 2.1: Properties of some magnetic nuclei relative to NMR spectroscopy.**

| **Isotope** | **Spin** | **Natural abundance (%)** | **Gyromagnetic ratio (rad $T^{-1}$ $s^{-1}$)** | **Absolute sensitivity** | **Resonant frequency @ $B_0$=9.39 T (MHz)** |
|---|---|---|---|---|---|
| $^{1}H$ | ½ | 99.980 | 26.75 | 1.00 | 400 |
| $^{29}Si$ | ½ | 4.700 | -5.30 | $3.7x10^{-4}$ | 79.5 |
| $^{13}C$ | ½ | 1.108 | 6.73 | $1.8x10^{-4}$ | 100 |

### 3. Pulsed radiofrequency and Fourier Transform

Typically, there is a slight excess of nuclei that are aligned with the external field compared to the number of nuclei that are aligned in opposite direction to this field. A strong magnetic field $B_1$ that is orthogonal to $B_0$ is then applied through the radiofrequency coil seen in Figure 2.1a. This causes the nuclear dipole excess which was originally aligned with $B_0$ to align with $B_1$. $B_1$ is then turned off which induces the nuclei to resonate or precess around the static $B_0$ field. This is known as the nuclei relaxation process and is characterized by an exponential decay. This excitation/relaxation process constitutes 1 scan. About 32 scans are usually recorded for $^{1}H$ NMR, while about 1000 scans are needed for $^{13}C$ and $^{29}Si$ in order to increase the signal to noise ratio due to the low sensitivity of these nuclei. In order to obtain the resonance fingerprint of all the represented nuclei, all the frequencies around the resonant frequency are excited

simultaneously and recorded as 1 composite signal. This signal exhibits an exponential decay due to all the nuclei that are undergoing relaxation simultaneously. A Fourier Transform (FT) is used as a way to deconvulate this composite signal into individual frequencies or resonant peaks as shown in Figure 2.3.

Tetramethyl silane ($Si(CH_3)_4$) may be used as a reference peak for proton and silicon NMR. For proton NMR, tetramethyl silane peak is set a 0 ppm by definition because tetramethyl silane has one of the lowest precessional frequencies. This is due to silicon which is more electropositive than carbon, concentrating the electron density towards the methyl protons, thus shielding them. Contrarily, as the electron density around the nucleus is decreased, the nucleus appears deshielded and consequently, the chemical shift increases due to increased precessional frequency.

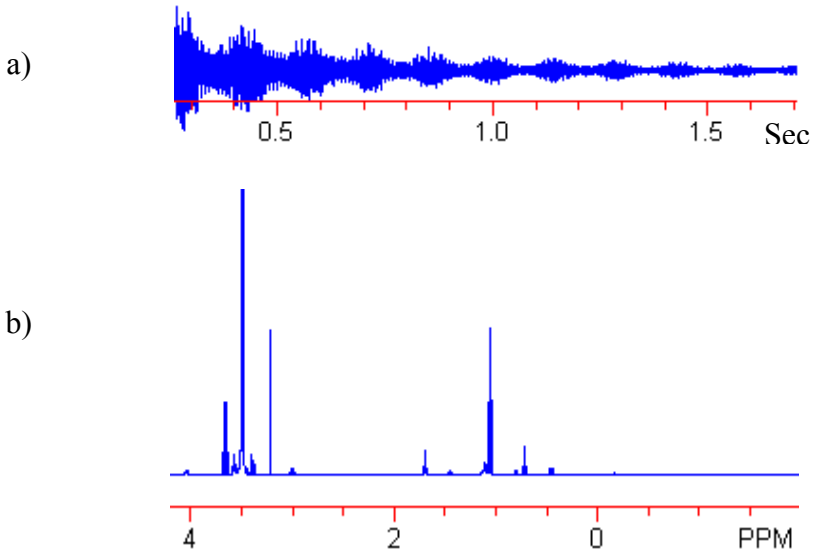


**Figure 2.3: NMR signal recorded after a pulsed radiofrequency excitation. a) Shows the exponential decay of all nuclei relaxation after radiofrequency excitation. b) Shows the individual chemical shift peaks after application of a Fourier Transform to deconvulate the signal.**

In summary, in the presence of an external magnetic field, magnetic nuclei have a magnetic moment $\mu$, which depends on the gyromagnetic ratio $\gamma$ and on the spin angular momentum I, and which is given by:

$$\mu = \gamma I \tag{2}$$

The gyromagnetic ratio $\gamma$ differs for each nucleus. Under an external magnetic field, the frequency of precession $\nu$ around $B_0$ (at which the orientation changes) is given by:

$$\nu = \frac{\gamma}{2\pi} B_0 \tag{3}$$

This constitutes the NMR spectroscopy key equation. $^{1}H$, $^{29}Si$, and $^{13}C$ NMR spectroscopy were used to characterize the structures of the linear and star-shaped PEG derivatives in dilute solution, synthesized for this research project (see Chapter III).

## B. *X-Ray Photoelectron Spectroscopy (XPS)*

### 1. Principles

X-Ray Photoelectron Spectroscopy (XPS) is recognized as a powerful surface chemistry sensitive analytical tool, which is based on photoemitted electrons during irradiation of a sample by monochromatic X-rays and on the measurement of binding energies of the corresponding core-level electrons. These photoelectron binding energies decay exponentially as a function of traveled distance within the sample thickness, and consequently, only the electrons emitted from the outermost few monolayers are considered. The binding energy of photoemitted electrons is described in function of its kinetic energy by the equation:

$$E_k = h\nu - BE - \Phi \tag{4}$$

where $E_k$ is the measured photoelectron kinetic energy, $h\nu$ is the x-ray source irradiation energy (1253.6 eV for Mg $K_\alpha$), $BE$ is the photoelectron binding energy, and $\Phi$ is the work

function (~4.9 eV). The mean photoelectron escape depth depends on the sample surface orientation compared to the detector and is given by:

$$d = \lambda \sin\theta \tag{5}$$

where $d$ is the sampling depth, $\lambda$ the electron effective attenuation length which can be calculated based on the overlayer composition and on the photoelectron nature, and θ the take-off-angle, i.e. the photoelectron emission angle between the surface plane and the detector. Figure 2.4 summarizes XPS instrumentation, sampling depth, and the binding energy calculation based on kinetic energy measurements. For the XPS studies that were conducted here and that are reported in Chapter IV, $\lambda$ was calculated using the NIST Standard Reference Database (version 1.1) and found to be equal to 2.90 nm for the C 1s photoelectrons. This agrees very well with values reported in the literature for PEG films[2]. Some possible sampling depths were calculated and are reported in Table 2.

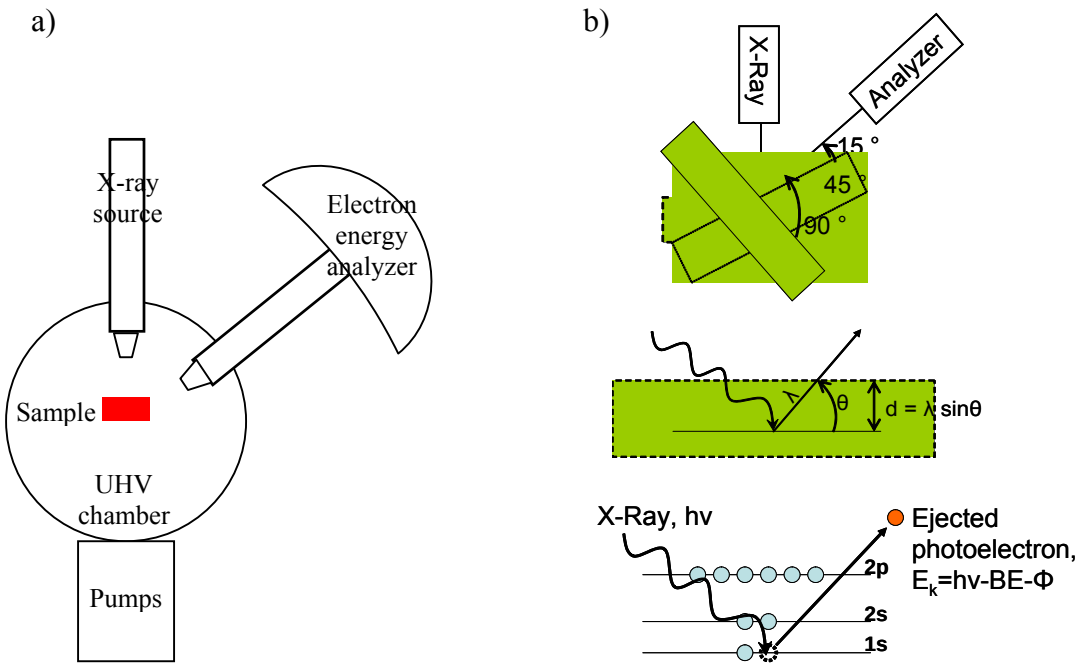


**Figure 2.4: a) XPS experimental set-up, and b) mean escape depth *d* which is a function of the take-off-angle *θ* shown as 15°, 45°, and 90°, and expression of the emitted photoelectron kinetic energy $E_k$.**

**Table 2.2: Calculation of the mean escape depth *d* at various take-off-angles *θ* for the PEGylated surfaces studied in Chapter IV.**

| Take-off-angle *θ* (°) | Mean escape depth *d* (nm) |
|---|---|
| 15 | 0.75 |
| 45 | 2.05 |
| 90 | 2.90 |

2. Binding energies

Polymeric films are composed of light elements which include carbon, oxygen, nitrogen, and silicon, whose binding energies are well known and documented. Traditionally, the binding energy of the C 1s electron is used as a spectrum reference. Specifically, the C-C or C-H bond is set at 285 eV. Various elements bound to C will induce different binding energy shifts. Thus, while C-NH and C-O-C bonds shift the C1s binding energy to higher energies (relatively to 285 eV) to about 285.5 and 286.5 eV respectively, $SiO_x$-$C_y$ binding energies are shifted down. This is due to differences in electronegativity of N, O, and Si. Figure 2.5 shows a C 1s spectrum obtained for a linear PEG layer deposited on a silicon wafer (see Chapter IV) and illustrate some binding energy upper and down shifts relatively to the 285 eV reference.

3. Overlayer thickness and density calculations

Binding energy signal intensity is proportional to the amount of a particular element chemical environment at this particular binding energy shift. Additionally, XPS signal intensities are known to decay exponentially with film thickness, resulting in the following relationship[3]:

$$I \propto \exp\left(\frac{-d}{\lambda \sin\theta}\right) \qquad (6)$$

where $I$ is the signal intensity, $d$ the overlayer thickness, $\lambda$ the photoelectron attenuation length through the overlayer, and $\theta$ the take-off-angle used when measuring the corresponding signal intensity (i.e. angle between surface plane and detector).

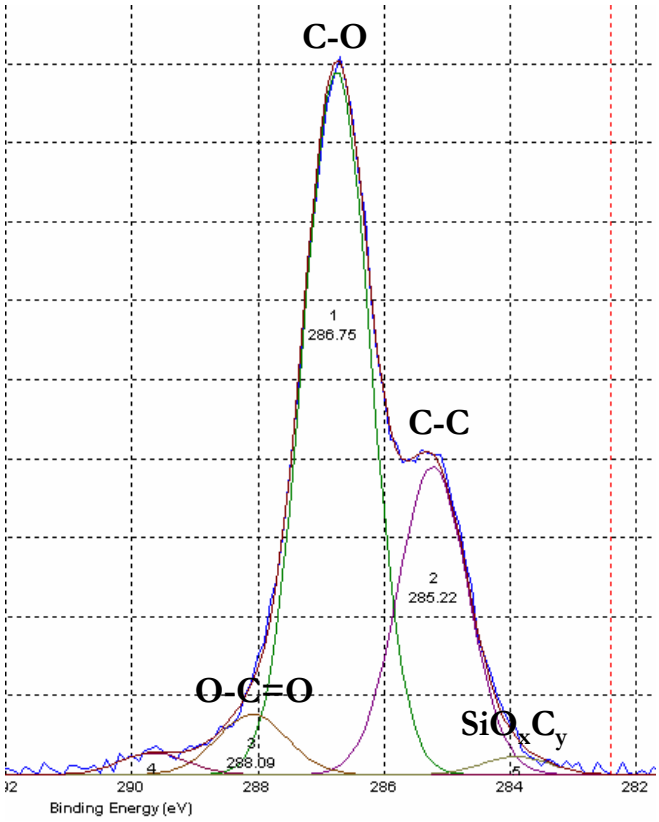


**Figure 2.5: XPS C 1s spectrum obtained for a PEGylated silicon wafer substrate showing various binding energy shifts compared to the C-C 285 eV reference. A binding energy down shift is seen for carbon bound to siloxane ($SiO_xC_y$) bridges whereas upper shifts are observed for ether (C-O) and carbonyl (O-C=O) bonds.**

The thickness of ultra-thin overlayers (i.e. less than about 10 nm in thickness) can be calculated using the relationship[2]:

$$\frac{I}{I_0} = 1 - \exp\left(\frac{-d}{\lambda \sin\theta}\right) \tag{7}$$

where $I$ is the intensity of a particular peak for overlayer of interest, $I_0$ is the intensity of the same peak obtained for a film thicker than the sampling depth (~2 nm at 45 ° take-

off-angle), $d$ is the thickness of the overlayer of interest, $\lambda$ is the photoelectron attenuation length through the overlayer of interest, and $\theta$ is the take-off-angle used when measuring the corresponding signal intensities (i.e. angle between surface plane and detector). It is well accepted that this equation is only valid for overlayers with thicknesses below 10 nm[3]. This equation was used to calculate the linear and star PEG layers thickness synthesized in Chapter IV as their thickness was found to be significantly below 10 nm using an ellipsometer.

An overlayer grafting density, defined as the area per anchored molecule ($nm^2$/chain), may also be calculated and is defined by[4]:

$$\sigma = 1/d^2 = \left( \frac{h\rho N_A}{M} \right) \tag{8}$$

where $h$ is the overlayer thickness measured by ellipsometry, $\rho$ the molecular mass density, $N_A$ the Avogadro's number, and $M$ the molecular weight. These thin-layer thickness and density calculations were applied to the linear and PEG derivatives synthesized for this research project (see Chapter IV).

## C. *Ellipsometry*

### 1. Principles

The ellipsometer measures the complex ratio $r$ of amplitude reflectivities for $p$ and $s$ polarized light ($r_p$ and $r_s$, respectively):

$$r = \frac{r_p}{r_s} = r_r + ir_i \tag{9}$$

When a thin overlayer is deposited on a substrate, the amplitude reflectivities of *p* and *s* polarized light changes and are functions of η according to:

$$r_i = \mathrm{Im}\left[\frac{r_p}{r_s}\right] = \frac{\pi}{\lambda}\left(\frac{\sqrt{\varepsilon_1 + \varepsilon_2}}{\varepsilon_1 - \varepsilon_2}\right)\eta \tag{10}$$

with

$$\eta = \frac{(\varepsilon_0 - \varepsilon_1)(\varepsilon_0 - \varepsilon_2)}{\varepsilon_0} h \tag{11}$$

and

$$\varepsilon_i = \eta_i^{\,2} \tag{13}$$

where $\lambda$ is the incident laser light wavelength, $\varepsilon_0$, $\varepsilon_1$, and $\varepsilon_2$ the dielectric constants of the incident, reflecting, and layer media, $\eta$ the measured refractive index, $h$ the layer thickness, and $\eta_i$ the refractive indices of the incident, reflecting, and layer media. In practice, $r_i$ is measured at the Brewster angle when $r_r$ equals 0. Given the value $r_i$ it is then possible to calculate the layer thickness $h$. The Brewster angle is a particular incident angle at which light with a particular polarization is not reflected.

### 2. Application to a 3-medium interface

These equations hold for a 3-medium interface, which will be applied to the air-PEG/$SiO_2$-Si system studied in Chapter IV. Because PEG and $SiO_2$ have similar refractive indices, it was possible to model the PEG layer and the $SiO_2$ layer as a single layer with a refractive index of 1.455. Measuring the reflectivity of a bare silicon wafer allowed to calculate the $SiO_2$ thickness, which was then subtracted from the thickness

found when measuring the reflectivity of the PEG overlayer containing system. This allowed to obtain PEG thickness values. Figure 2.6 shows a representation of this model.

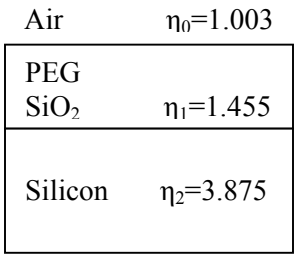


**Figure 2.6: A 3-medium interface system similar to that studied in Chapter IV, comprised of a PEG overlayer deposited on SiO2/Si and studied in ambient air.**

## D. *Water contact angle*

### 1. Definition:

A contact angle represents the thermodynamic equilibrium between the interfacial energies of 3 phases, generally a solid surface, a liquid drop, and a gas/vapor as shown in Figure 2.7. In turn, at equilibrium we can write the following equation known as the Young condition[5]:

$$\gamma_{Sol/Vap} - \gamma_{Sol/Liq} - \gamma_{Liq/Vap}\cos\theta = 0 \qquad (14)$$

where $\gamma_{Sol/Vap}$ is the interfacial energy at the solid/vapor interface, $\gamma_{Sol/Liq}$ the interfacial energy at the solid/ liquid interface, and $\gamma_{Liq/Vap}$ the interfacial energy (surface tension) at the liquid/vapor interface, and $\theta$ is the measured contact angle using a goniometer.

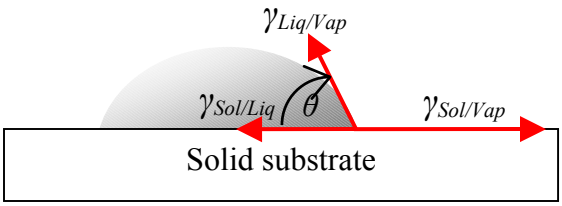


**Figure 2.7: Thermodynamic equilibrium between 3 interfacial energies.**

It is well accepted that the chemical composition of the solid substrate and that of the liquid both affect the contact angle or wettability of the substrate[5]. There are high cohesive energy and low cohesive energy surfaces (with high and low surface tension), where hard substrates characterized by covalent, ionic, or metallic bonds generally result in high energy surfaces, while soft molecular substrates characterized by van der Waals or hydrogen bonds result in low energy surfaces. High energy surfaces may give rise to complete wetting with most liquids, while molecular soft surfaces which have lower surface tension may result in partial wetting to complete wetting.

2. Static sessile water drop:

The water contact angle $\theta$ of a particular flat solid substrate in ambient air is measured by dropping a small water droplet on that surface and measuring the angle formed between the substrate/water interface and the water/air interface. Therefore, $\theta$ is a measure of the solid/liquid and liquid/gas interfacial energies. Lower water contact angles between 0 and 90 º characterize hydrophilic surfaces, while higher water contact angles between 90 and 180 º are hydrophobic. The sessile drop method measures the static water contact angle using a goniometer. The static sessile water drop technique was used to measured water contact angle of the tethered linear and star-shaped PEG molecules, before and after protein adsorption (see Chapter IV).

**References:**


1. Kemp, W., *NMR in Chemistry*, ed. W. Kemp. 1986: McMillan.
2. Sofia, S. J.; Premnath, V.; Merrill, E. W., *Poly(ethylene oxide) Grafted to Silicon Surfaces: Grafting Density and Protein Adsorption.* Macromolecules, 1998. **31**: p. 5059-5070.
3. Powell, C. J.; Jablonski, A., *Electron effective attenuation lengths for applications in Auger electron spectroscopy and x-ray photoelectron spectroscopy.* Surf. Interface. Anal., 2002. **33**: p. 211-229.
4. Irvine, D. J.; Mayes, A. M.; Satija, S. K.; Barker, J. G.; Sofia-Allgor, S. J.; Griffith, L. G., *Comparison of tethered star and linear poly(ethylene oxide) for control of biomaterials surface properties.* J. Biomed. Mater. Res., 1998. **40**: p. 498-509.
5. De Gennes, P. G., *Wetting: statics and dynamics.* Review of Modern Physics, 1985. **57**: p. 827-863.

# CHAPTER III.

## SYNTHESIS AND CHARACTERIZATION OF MATCHING MOLECULAR WEIGHT LINEAR AND STAR-SHAPED CORE-FUNCTIONALIZED POLYETHYLENE GLYCOL DERIVATIVES

### A. *Introduction*

Protein adsorption properties of tethered polyethylene glycol (PEG) have been extensively studied over the past decades, and PEG-tethered surfaces have emerged as protein resistant surfaces. Several mechanisms have been envisioned to make sense of the unique properties exhibited by PEG. Traditionally, the mechanisms regarded as factors necessary to hinder protein adsorption are i) steric exclusion arising from the compression of longer chains, ii) grafting density contribution which may provide shielding from the underlying material, and iii) PEG-water dissolution properties[1-4].

Studies have looked at studying grafted PEG chains with various architectures. These have included linear and star-shaped PEG molecules[5, 6]. Star molecules are characterized by the junction of a certain number of linear PEG chains, which we call the arms of a star molecule. By definition, star-shaped molecules have an increased number of chains per unit volume in comparison to linear molecules, a property which is conserved when these molecules are grafted onto a surface. The junction of star molecules forms the star core and the arms are forced to extending out from the higher density core. Although star-shaped molecules have been of great interest due to their specific rheological and diffusion properties, they have been a great way to assess if increased PEG density correlated with increased protein resistance due to high functional density. It was found that PEG stars overlapping is necessary in order to repel protein adsorption, just like it is the case for grafted linear PEG chains. Additionally, achieving

overlapping grafting densities for PEG stars was found to be challenging because the solvent quality was demonstrated to greatly affect the grafted PEG star density. Poor solvent conditions occur with increased ionic strength whereas good solvent conditions happen when no salt is added. Irvine[6] demonstrated that poor solvent conditions achieved with 5% (w/w) PEG star solution and 0.4M $K_2SO_4$ added salt led to grafting point separation down to 200 Å, while a 15% (w/w) PEG star solution with good solvent conditions, i.e. with no added salt, led to a 25 % increase in surface coverage and anchor separation of around 140 Å. The 0.4M $K_2SO_4$ added salt in the 5% solution resulted in phase separation at room temperature due to lowering of the cloud point of the star solution, which was not the case with increased solution concentration (15%) and no added salt. Therefore, for these star molecules, good solvent conditions and a solution concentration slightly greater than the overlap concentration led to stars overlap and were preferable for maximized surface coverage or grafting density. Contrarily, they found that poor solvent conditions with 0.4M $K_2SO_4$ added salt led to linear molecules overlap and maximized surface coverage for linear PEG molecules. Sofia[5] achieved linear PEG molecules overlap with grafting densities slightly below those obtained by Irvine[6] (0.06 and 0.03 chain/$nm^2$ vs. 0.09 and 0.06 chain/$nm^2$ for similar PEG molecular weights) using linear PEG solution concentration above the overlap concentration and no added salt. These slightly lower linear PEG grafting density still resisted protein (of similar sizes) adsorption, which was the point. Therefore, based on these 2 studies, both linear PEG molecules and hard-sphere like PEG star molecules, dissolved in a good solvent, i.e. without added salt, at concentrations above their respective overlap concentrations seems to be necessary to fully repel proteins.

The PEG star molecules which were used in these studies have very high PEG densities. In fact they are comprised of 20, 24, 70 and 72 arms. As mentioned earlier, this many number of arms result in a specific structure which is known as a hard-sphere like structure due to the steric hindrance arising from the large number of arms in a small area. In contrast, linear PEG chains are modeled as random coils. It was showed that this hard-sphere like structure forces the extension of arms, increasing the PEG segment density away from the substrate, while lowering it near the substrate[6]. Therefore,

although the stars are overlapping, protein adsorption may occur between the stars near the substrate, where the PEG segment density is lower. Overlapping tethered linear molecules present higher PEG segment density near the substrate and better resist protein adsorption. Additionally, these studies have compared protein adsorption on tethered linear with molecular weights several orders of magnitude smaller than those of tethered star-shaped PEG molecules (i.e. 10 000 and 20 000 g/mol vs. 200 000, 233 000, 350 000, and 360 000 g/mol for linear and star molecules, respectively).

Here, it is proposed to considerably lower the density of PEG stars by significantly decreasing the number of arms targeting around 6 arms per star molecules instead of 20 to 72 arms like in the previous cases. This decreased chain density should decrease the steric hindrance at the core and therefore these star molecules should have more of a random coil structure and less of a hard sphere behavior. In turn, this should allow to achieve higher grafting densities and lower anchor separation more easily, while still conserving higher PEG chain concentration compared to linear molecules. Additionally, we want to synthesize core-functionalized PEG stars as opposed to end-functionalized star molecules like those considered by Sofia[5] and Irvine[6], to vary the anchor points position which free up chains next to the surface, and may therefore increase protein resistance next to the surface. Thirdly, matching molecular weights between linear and star molecules will allow to study the effects of linear and star-shaped PEG molecules architecture on protein adsorption without orders of magnitude of difference in molecular weights.

To achieve these goals, we have synthesized matching molecular weights (around 3000 g/mol) linear and star-shaped PEG derivatives with ethoxysilane functionalization. The synthesis of star molecules leads to core-functionalized molecules. In Chapter V, both of these functionalized PEG derivatives have been grafted onto solid substrates and their resistance towards human albumin was studied. The PEG hydroxyl group at one chain end permitted to attach a triethoxysilane functionality, and then hydrolysis and condensation of these linear molecules led to core-functionalized PEG star molecules. These hydrolysis and condensation reactions have been reported before although

trimethoxysilane functionalized polystyrene was used instead of triethoxysilane functionalized PEG here[7].

## B. *Materials and Methods*

### 1. Synthesis of triethoxysilane functionalized linear PEG molecules

Monomethylether polyethylene glycol (MPEG) with molecular weights of 550 and 1900 g/mol were obtained from Sigma-Aldrich and Alfa Aesar, respectively. These were stored in a dry place and replaced often to avoid premature hydroxyls reaction. Sure-seal anhydrous tetrahydrofuran (THF) and 3-isocyanatopropyl triethoxysilane (IPTES) were obtained from Sigma-Aldrich. Dibutyltin dilaurate (DBTL) was obtained from Sigma-Aldrich and used without further modification as the catalyst. A 70°C oil bath and a condenser were used to carry the functionalization reaction of linear PEG molecules. Great care was taken during this functionalization reaction and glassware was dried for at least 24 hours in a 105°C oven prior to use to eliminate the possibility of water contamination during the reaction which would have affected reaction yield and product.

The general strategy was to synthesize 2 linear PEG derivatives including one starting with MPEG 550 (550 g/mol) and another one starting with MPEG 1900 (1900 g/mol). The smaller molecular weight linear PEG molecules were subsequently utilized to form the star-shaped PEG molecules, the goal being to obtain star molecules with molecular weight similar to that of the higher molecular weight linear derivative. Figure 3.1 illustrates this general strategy along with the number-average molecular weights corresponding to Linear i) and ii) as well as 3, 4, 5, and 6-arm stars. These molecular weights were calculated based on the proposed reactions and expected structures of these derivatives. Because hydrolysis and condensation reactions may result in a statistical distribution of stars with various numbers of arm, 3, 4, 5, and 6-arm stars are represented in Figure 3.1.

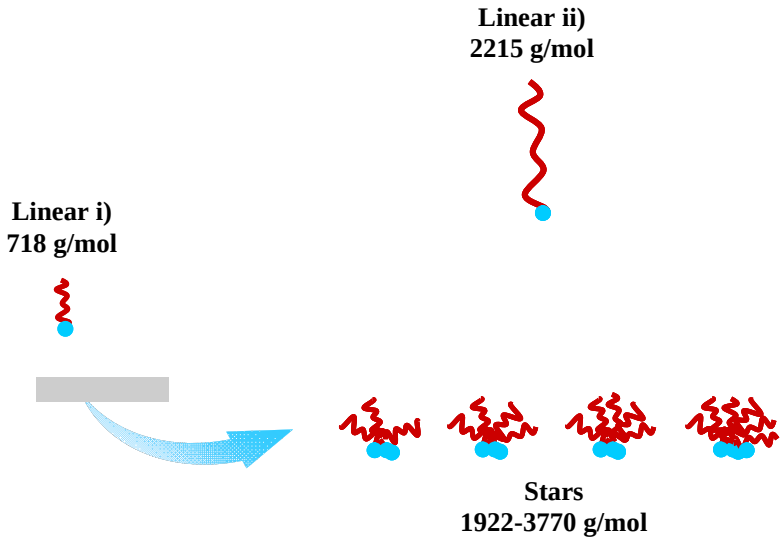


**Figure 3.1: General strategy used to synthesize linear and star-shaped functionalized PEG derivatives shown with their expected number-average molecular weights. The molecular weights listed below each figure were calculated based on the predicted structures shown in Figures 3.2-3.3.**

The synthesis of triethoxysilane-functionalized linear PEG derivatives was carried out by reacting IPTES with MPEG in slight excess to ensure full reaction of IPTES. The molar ratio of 1.01:1 [MPEG]:[IPTES] was used and a nitrogen atmosphere was allowed during the reaction. To create the lower molecular weight linear PEG derivative, which will be referred to as "Linear i)", MPEG (550 g/mol) (4.46 g, 8.1 mmol) was added to a 100 ml round bottom flask, septum sealed and under nitrogen. Dry THF (22 ml) was added to make a 20 wt % solution, and stirred for 20 min at room temperature. The reaction flask was equipped with a water condenser and was immersed in an oil bath at 70°C. IPTES (1.98 g, 8.019 mmol) was added very slowly using a syringe, and stirred for about 10 min. 0.34 mmol of DBTL was then added to the reaction and the reaction was stirred at 70°C for 1 hour. The same reaction was carried out with the higher MPEG molecular weight (1900 g/mol) in order to synthesize the linear triethoxysilane-functionalized PEG derivatives which we will refer to as "Linear ii)". A rotary evaporator was used to evaporate the solvent, THF, after functionalization of both linear products. Anhydrous hexane and ethyl ether (Sigma-Aldrich) were used to precipitate these linear products and

remove DBTL which dissolve in hexane, which were then dried overnight in a vacuum oven at 29 inHg and room temperature. The chemical reactions for synthesizing both Linear i) and Linear ii) should go according to the schematic shown in Figure 3.2:

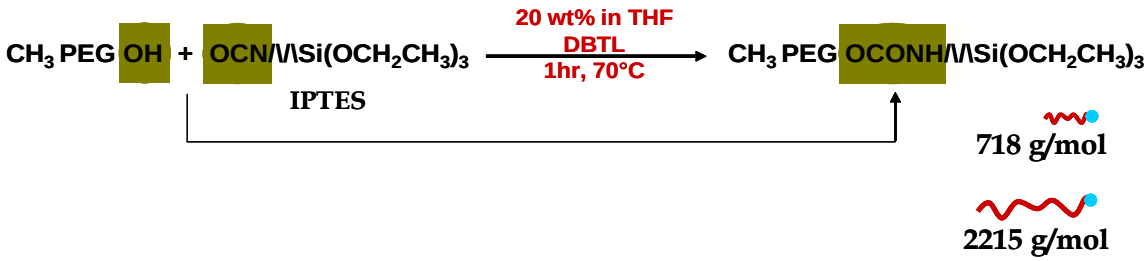


**Figure 3.2: Synthesis of Linear i) and Linear ii) PEG molecules.**

2. Synthesis of core-functionalized star-shaped PEG molecules

Hydrolysis and condensation was conducted only on the linear product synthesized from the 550 g/mol MPEG because the goal was to match the overall molecular weight of the linear and star-shaped products. Therefore we used smaller molecular weight linear molecules to synthesize the stars, whose final molecular weight was targeted to be around 3000 g/mol. Triethoxysilane linear PEG (5 g) was added to a 100 ml round bottom flask containing 25 ml of dry THF to make a 20 wt % solution. The solution was stirred and 0.6 ml of 1N HCl was added to the solution and stirred for 20 hours. This amount of acidic water ensured that there was a 4-fold molar excess of water compared to linear PEG molecules. 1N HCl solution was made with deionized water with a resistivity of 18 MΩ/cm at 25°C (Barnstead NANOpure water system) and hydrochloric acid (HCl) (37%). The 37% HCl solution was diluted 12 fold with deionized water to make a 1N HCl solution and used as the hydrolysis catalyst. Hydrolysis and condensation were observed to occur within 20 hours based on GPC and $^{29}$Si NMR data. After hydrolysis/condensation reaction, THF and HCl were rotavaped, and the triethoxysilane-functionalized PEG stars were vacuum dried overnight at 29 inHg and room temperature to remove water. Figure 3.3 illustrates the synthesis route for star molecules.

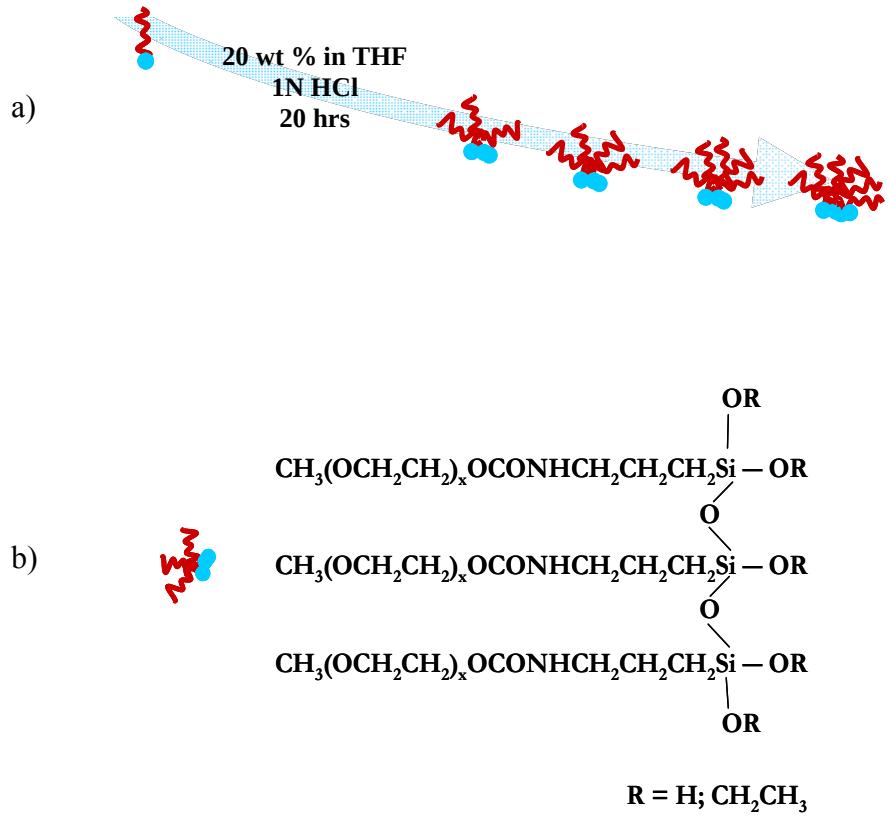


**Figure 3.3: a) Synthesis of core-functionalized star-shaped PEG derivatives with various numbers of arms, shown as ranging from 3 to 6 on this schematic, and b) detail of a 3-arm star structure. Because MPEG 550 was used, *x*, the number of ethylene glycol units, can be considered close to 10.**

## 3. Characterization of functionalized linear and star-shaped PEG molecules

### *a) Nuclear Magnetic Resonance Spectroscopy*

Both linear functionalized PEG molecules structures and number-average molecular weights were characterized using $^{1}$H NMR spectroscopy of polymers dissolved in deuterated chloroform ($CDCl_3$) to make a ~2 wt % solution. Unwanted condensation reaction between triethoxyxilane was avoided using chloroform. A Varian Inova at 400 MHz was used to record the data. $^{13}$C and $^{29}$Si NMR spectroscopies were carried out using a Varian Unity spectrometer at 100 and 79.5 MHz, respectively. 20 wt % solutions dissolved in $CHCl_3$ were used, confirming reaction yields as well as the structure of star

molecules. $Cr(acac)_3$ (0.06M) was added to the polymers dissolved in $CHCl_3$ to reduce the relaxation times.

### *b) Gas Permeation Chromatography*

Number-average molecular weights and their respective distributions were determined for linear and star-shaped PEG molecules using a Gas Permeation Chromatography (GPC) column equipped with an Evaporative Light Scattering Detector (ELSD) detector which is not sensitive to temperature changes like a refractive index detector would be. The experiments were conducted at room temperature, in THF, with a 1ml/min flow rate.

### *c) Liquid Chromatography-Mass Spectroscopy*

The molar mass distributions of both linear PEG molecules were studied using a methanol solution at 1 μg/ml and the electrospray ionization method at 2500 V in the positive mode. This allowed to observe several ionized mass distributions which included $[m+H]^+$, $[m+Na]^+$, and $[m+K+Na]^+$.

### *d) Modulated Differential Scanning Calorimetry*

The melting temperatures of linear and star-shaped PEG polymers were studied using Modulated Differential Scanning Calorimetry (MDSC) under nitrogen. Modulated runs allow to remove non reversible transitions as the temperature is oscillated.

### *e) Dynamic Light Scattering*

The average hydrodynamic radius was determined in THF for linear and star-shaped PEG molecules using a dynamic light scattering (DLS) equipped with an ALV/LSE 5003 correlator and a 632.8 nm laser light. Data were obtained for a 90° angle and at 25°C. Multiple 30 sec. runs were conducted and ALV and DTS Nano softwares were used to plot the hydrodynamic radius data.

## C. *Results and Discussion*

### 1. Linear PEG derivatives

The triethoxysilane functionality was chosen because it readily undergoes hydrolysis and condensation reaction in the presence of water. This constitutes an easy synthetic route to form star molecules, and provides the opportunity to graft these molecules onto hydroxylated substrates. As mentioned previously, this has been conducted and is reporting in Chapter IV. Linear triethoxysilane-functionalized PEG derivatives were synthesized by allowing reaction between the hydroxyl present at 1 end of MPEG and the IPTES isocyanate group. This is known to be a relatively fast reaction in the presence of DBTL catalyst[8] creating an urethane linkage, i.e. OC(O)NH.

$^1$H NMR spectroscopy was used to confirm the structure of these linear molecules. Figure 3.4 represents a proton NMR spectrum obtained for Linear i) which shows various resonance peaks where they would be expected based on the structure. The resonance peaks arising from the PEG moiety are seen at 3.33, 3.60, and 4.16 ppm (resonances *a*, *b*, and *c*, respectively), as well as those arising from the triethoxysilane moiety at 3.10, 1.56, 0.57, 3.77, 1.17 ppm (resonances *e*, *f*, *g*, *h*, and *i*, respectively). Additionally, the 5.02 ppm resonance (peak *d*) is characteristic of the newly created urethane bond and is therefore characteristic of the Linear i) and ii) molecules. The number-average molecular weight of these linear derivatives was calculated based on the integral values of resonances *b* and *i* according to:

$$M_n = 44\left(\frac{\int b}{4\left(\frac{\int i}{9}\right)}\right) + 267 \text{ (g/mol)} \qquad (1)$$

where 44 is the molecular weight of 1 ethylene glycol unit, 4 the number of protons associated with the resonance *b* integral, 9 the number of protons associated with the resonance *i* integral, and 267 is the calculated molecular weight of the functionalized linear molecules without accounting for the ethylene glycol units, which are accounted for in the 1st term of equation 1. These are reported in Table 3.2.

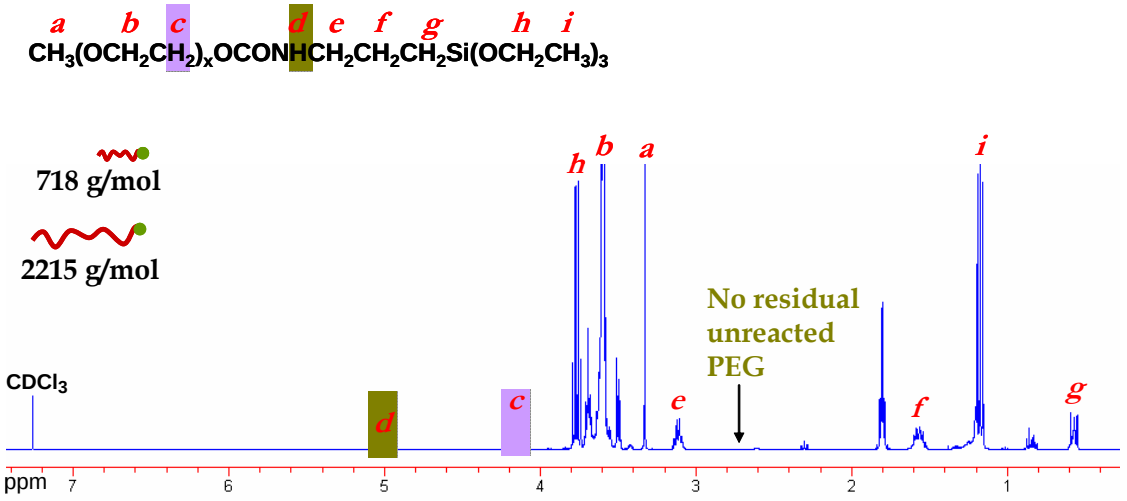


**Figure 3.4: $^{1}$H NMR spectrum obtained for both Linear i) and Linear ii) dissolved in $CDCl_3$ at a 2 wt % concentration and showing the resonance *d* that is characteristic of the derivatized linear PEG molecules, and also showing that MPEG has been quantitatively modified as residual hydroxyls would have resulted in a resonance peak around 2.40-2.80 ppm.**

Several observations led to the conclusion that this functionalization reaction yield was 100%; i) there was no residual hydroxyl peak whose resonance is known to be around 2.40-2.80 ppm[8]; ii) resonances *e*, *f*, *g*, *h*, and *i* were fully shifted towards lower frequencies compared to resonances *e*', *f*', *g*', *h*', and *i*' characteristic of unreacted IPTES by about 0.18, 0.15, 0.10, 0.05, and 0.05, respectively (see Figure 3.5), iii) the $^{13}$C NMR spectra shown in Figure 3.6 illustrate the disappearance of the IPTES isocyanate resonance *j* at 121.50 ppm along with the appearance of the urethane carbon as resonance *d* occurs at 155.83 ppm, and iv) the $^{29}$Si NMR spectrum for Linear i) shows that the silicon resonance peak is shifted to higher frequencies comparatively to that of unreacted IPTES by about 0.70 ppm (see Figure 3.7). Similar down field shifts have been reported in the literature[7, 9] which confirm the functionalization reaction went as expected and

that the cleavage of ethoxysilane via hydrolysis or alcoholysis did not occur as this would have resulted in even higher frequencies shifts. It is well known that the hydrolysis of ethoxy groups into hydroxyls would be characterized by $^{29}$Si resonance shift towards lower fields by about 1-2 ppm per hydrolyzed ethoxy group[10, 11]. Linear ii) exhibited similarly shifted resonance peaks position and shifts than Linear i), and thus the same conclusions can be drawn for both functionalized linear molecules. Lower frequency shifts observed for proton nuclei for Linear molecules i) and ii) may be explained by increased shielding around the nuclei due to increased electronic densities compared to unreacted IPTES. Higher frequency shifts observed for the silicon spectrum may arise from decreased shielding and electronic densities. Resonance shifts associated with protons can only arise from s-electrons which are symmetrically distributed around the nucleus and therefore induce a diamagnetic field (in opposition to the external field), lowering the frequency and chemical shift. On the contrary, carbon and silicon have electrons that are not symmetrically distributed (in addition to s-electrons), which affect the external field in many directions. Considering the proton shifts only described in Figure 3.5, we can see that as protons are located further away from the urethane linkage (resonances *e*, *f*, *g*, *h*, and *i*, respectively) their resonance shifts decrease, which may be due to various shielding influence arising from neighboring protons.

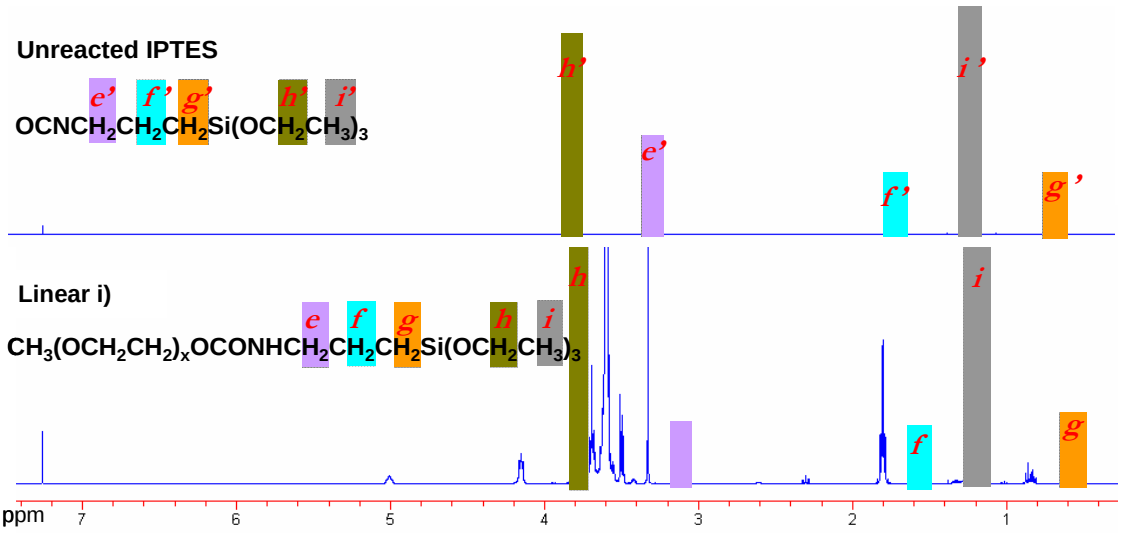


**Figure 3.5: $^{1}$H NMR spectra of unreacted IPTES compared to that obtained for Linear i) showing that the resonances *e'*, *f'*, *g'*, *h'*, and *i'* are fully shifted towards lower frequencies for Linear i), indicating high triethoxysilane functionalization yield (2 wt % solutions in $CDCl_3$).**

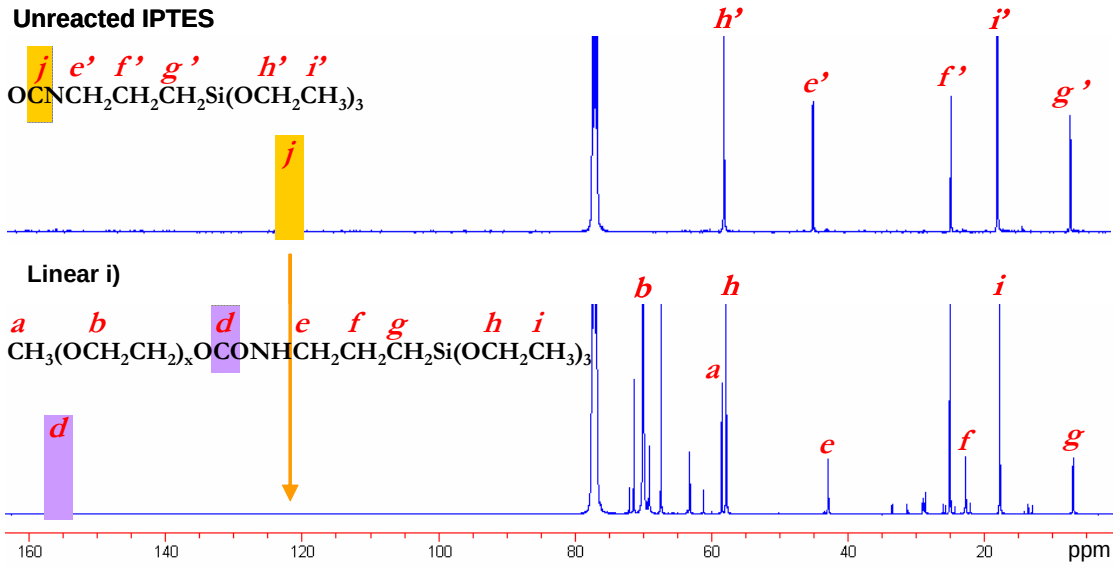


**Figure 3.6: $^{13}$C NMR spectra of unreacted IPTES compared to that obtained for Linear i) showing that the resonance *j* characteristic of the IPTES isocyanate reactive group fully disappears, and also showing an additional resonance *d* which appears at 155.83 ppm (20 wt % solutions in $CHCl_3$ with 0.06M $Cr(acac)_3$).**

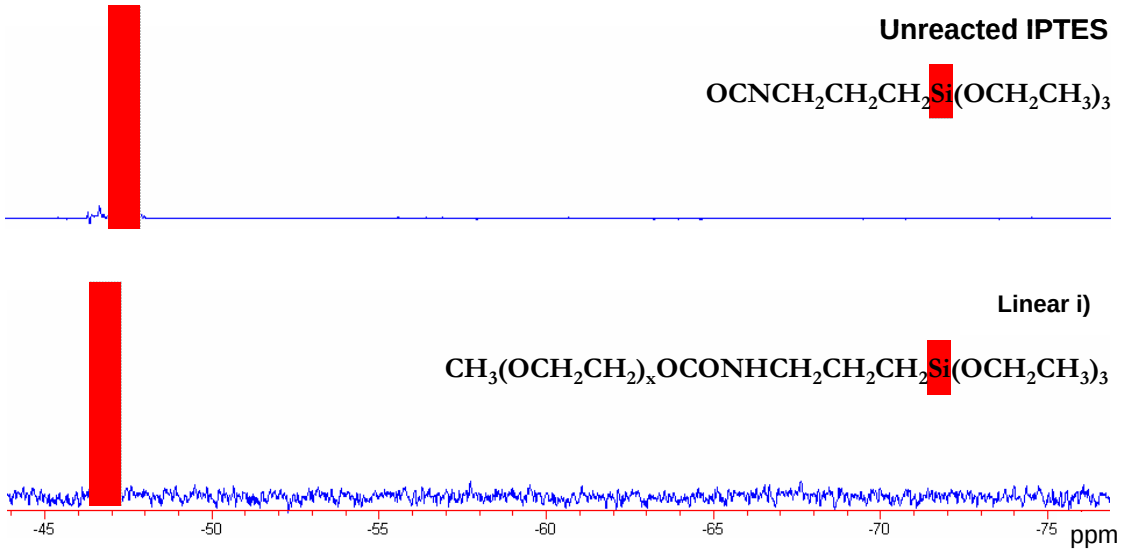


**Figure 3.7: $^{29}$Si NMR spectra of unreacted IPTES compared to that obtained for Linear i). This shows that the silicon resonance characteristic of Linear i) is shifted towards higher frequencies by about 0.70 ppm compared to that of unreacted IPTES (20 wt % solutions in $CHCl_3$ with 0.06M $Cr(acac)_3$).**

The gas permeation chromatography (GPC) system was calibrated using 5 PEG standards with a wide range of molecular weights, specifically 550, 1000, 2000, 4600, and 8000 g/mol. The expected linear relationship between the logarithm of PEG $M_n$ and their corresponding measured retention times through the GPC column was observed as shown in Figure 3.8. This linear relationship allowed to back calculate the $M_n$ of the synthesized products given their measured retention times. Linear i) was found to have a molecular weight of 757 ± 7 g/mol, while that of Linear ii) was 2393 ± 28 g/mol. This was based on data collected from at least 3 different batches, therefore showing the good repeatability of the synthesis.

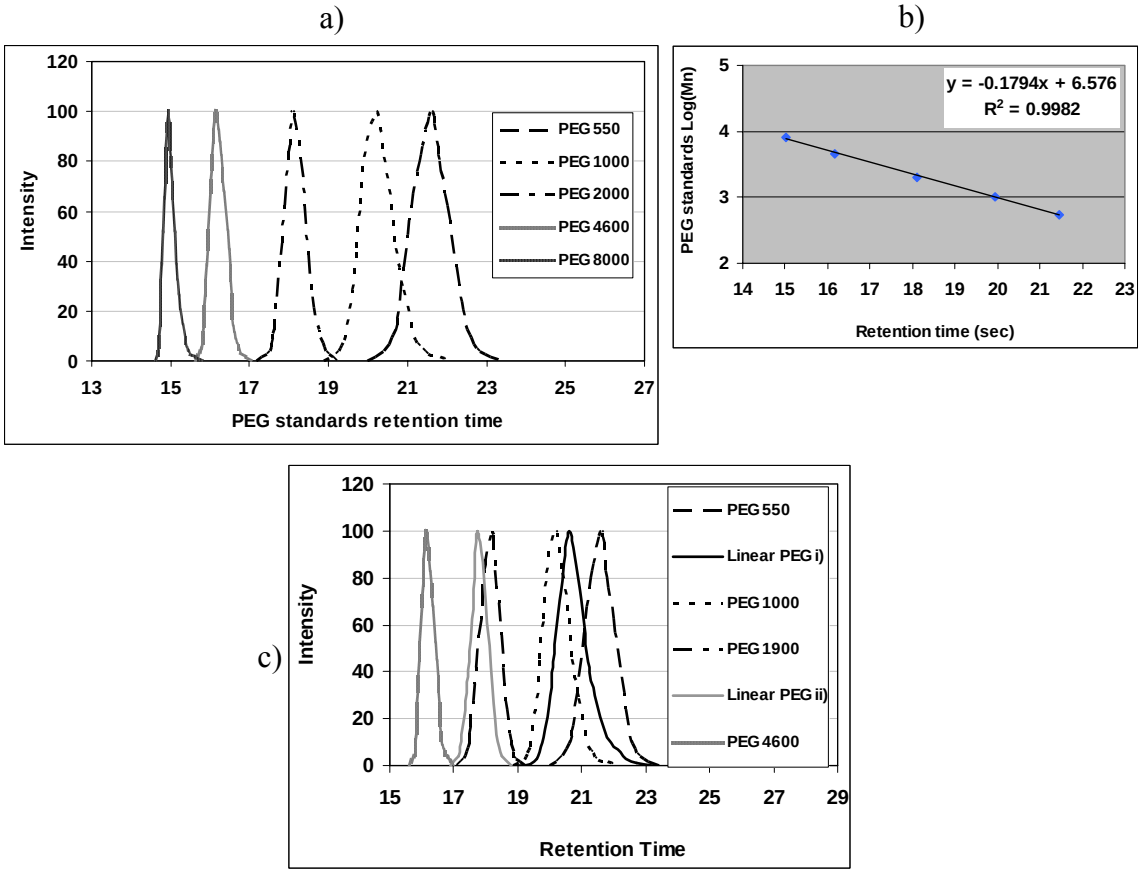


**Figure 3.8: a) Retention time characteristic of the PEG standards used to calibrate the GPC system, b) plot of the logarithm of the known $M_n$ vs. the measured retention time. A linear fit to these data points gave the relationship existing between PEG's molecular weight and retention time. c) Shows the molecular weight monodistributions obtained for Linear i) and Linear ii).**

**Table 3.1: Predicted and measured (by NMR and GPC) molecular weights for Linear i) and ii).**

| Architecture | Predicted $M_n$ (g/mol) | NMR $M_n$ (g/mol) | GPC $M_n$ (g/mol) |
|---|---|---|---|
| Linear i) | 718 | 799 ± 65 | 757 ± 07 |
| Linear ii) | 2215 | 2283 ± 375 | 2393 ± 28 |

Liquid Chromatography Mass Spectroscopy (LC-MS) revealed an isotope pattern similar to the calculated one using the Sheffield ChemPuter Isotope Patterns calculator given the molecular chemical composition. As shown in Figure 3.9, the isotope pattern for linear molecules shows 4 isotope masses m+1, m+2, m+3, and m+4 with respective intensities of 100, 40.3, 14.1, and 3.3%. Fragmentation was observed as 3 distinct mass distributions were seen in the positive mode. These 3 mass distributions were consistent with [m+H], [m+Na], and [m+Na+K]. The possibility of these distributions corresponding to side products was eliminated because i) GPC mass distributions are monodistributed without any unreacted or side products, and ii) NMR data showed full resonance shifts and 100 % reaction yield.

The melting temperatures ($T_m$s) of Linear i) and ii) were measured using Modulated Differential Scanning Calorimetry (MDSC) in order to ensure that PEG had not been degraded during the functionalization reaction. The data presented here are the averages of 3 measurements. Because the presence of any solvent may significantly decrease the observed $T_m$ values, Linear i) and ii) samples were dried in a vacuum oven at 29 inHg and at 30°C for about 16 hrs, which was sufficient to remove residual THF. Most of the solvent had previously been removed using the rotary evaporator. Table 3.1 lists the obtained Tm values for Linear i and ii) as well as for MPEG 550 and 1900, their respective reagents. Figure 3.10 shows a plot of these measured $T_m$ values. It is noticed that both linear molecules have $T_m$ values which are close to those of their respective MPEG reagents. Thus, the MPEG's $T_m$s can be regarded as the "before functionalization" $T_m$s while those of Linear i) and ii) would be the "after functionalization" values.

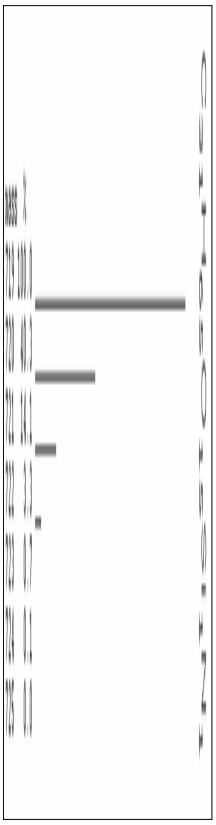

**Figure 3.9: Calculated Isotope pattern for Linear i) PEG molecules using the Sheffield ChemPuter Isotope Patterns calculator.**

Although the standard deviation associated with MPEG 550 is significantly larger than those associated with MPEG 1900, Linear i) and Linear ii), the triethoxysilane functionalization of the MPEG molecules appears lower both MPEG $T_m$s, which may be expected as the functionalization reaction forms a flexible urethane linkage. $T_m$ values decrease more significantly for MPEG 550 than for MPEG 1900 as $\Delta T_m$ equals 6.12 and 1.81°C for Linear i) and ii), respectively, and may be expected as different ratios existed between the functionality and the number of ethylene glycol units. In general, $T_m$ values measured by DSC type techniques are regarded as a distribution of $T_m$ values rather than absolute $T_m$ values[12]. $T_m$ distributions arise from the melting of crystallites (formed of lamellar folded chains) of various thicknesses, which may depend on the crystallites chemistry, crystallization kinetics, and thermal and mechanical properties. As expected, the melting temperature distributions observed for Linear i) were broad with a FWHM (full width half maximum) of about 10°C due to the crystalline nature of PEG chains

which is known to cause broad $T_m$ distributions[12]. Similarly broad $T_m$ distributions were as expected observed for MPEG 550[13], indicating that the functionalization reaction was not responsible for these wide $T_m$ distributions. Figure 3.11 shows the reverse heat flow as a function of temperature obtained for Linear i) and ii). Contrarily to Linear i), Linear ii) only had a FWHM of about 4.5°C, and which was similar to that of MPEG 1900.

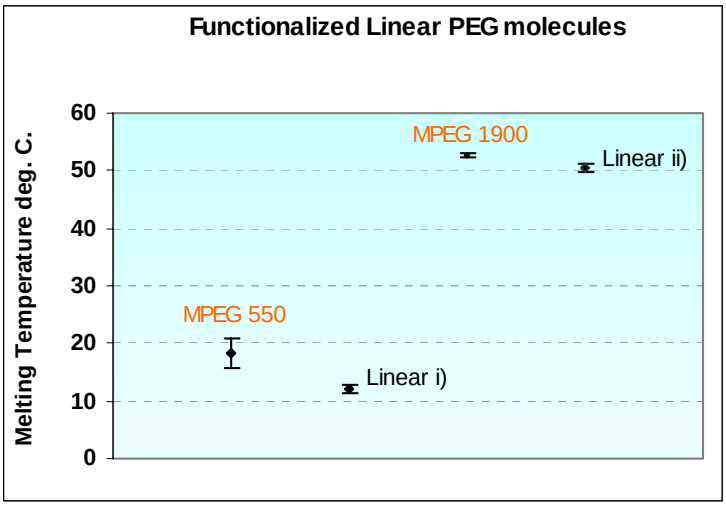


**Figure 3.10: Melting Temperatures ($T_m$s) for Linear i) and ii) PEG functionalized molecules as measured with MDSC. These values are compared to those obtained for the MPEG reagents, which were used to synthesize Linear i) and ii).**

These narrower $T_m$ distributions seen with MPEG 1900 and Linear ii) may be attributed to the fact that at these higher molecular weights, PEG chains are able to fold in better resulting in a more homogenous size distribution.

2. Star-shaped PEG derivatives:

Ethoxy hydrolysis and condensation reactions were conducted in acidic water and at room temperature, which were found to successfully create star-shaped PEG molecules with various numbers of arms. $^{29}$Si NMR spectra comparison was primarily conducted to

confirm the hydrolysis and condensation of linear i) into star-shaped molecules. These spectra are shown in Figure 3.12.

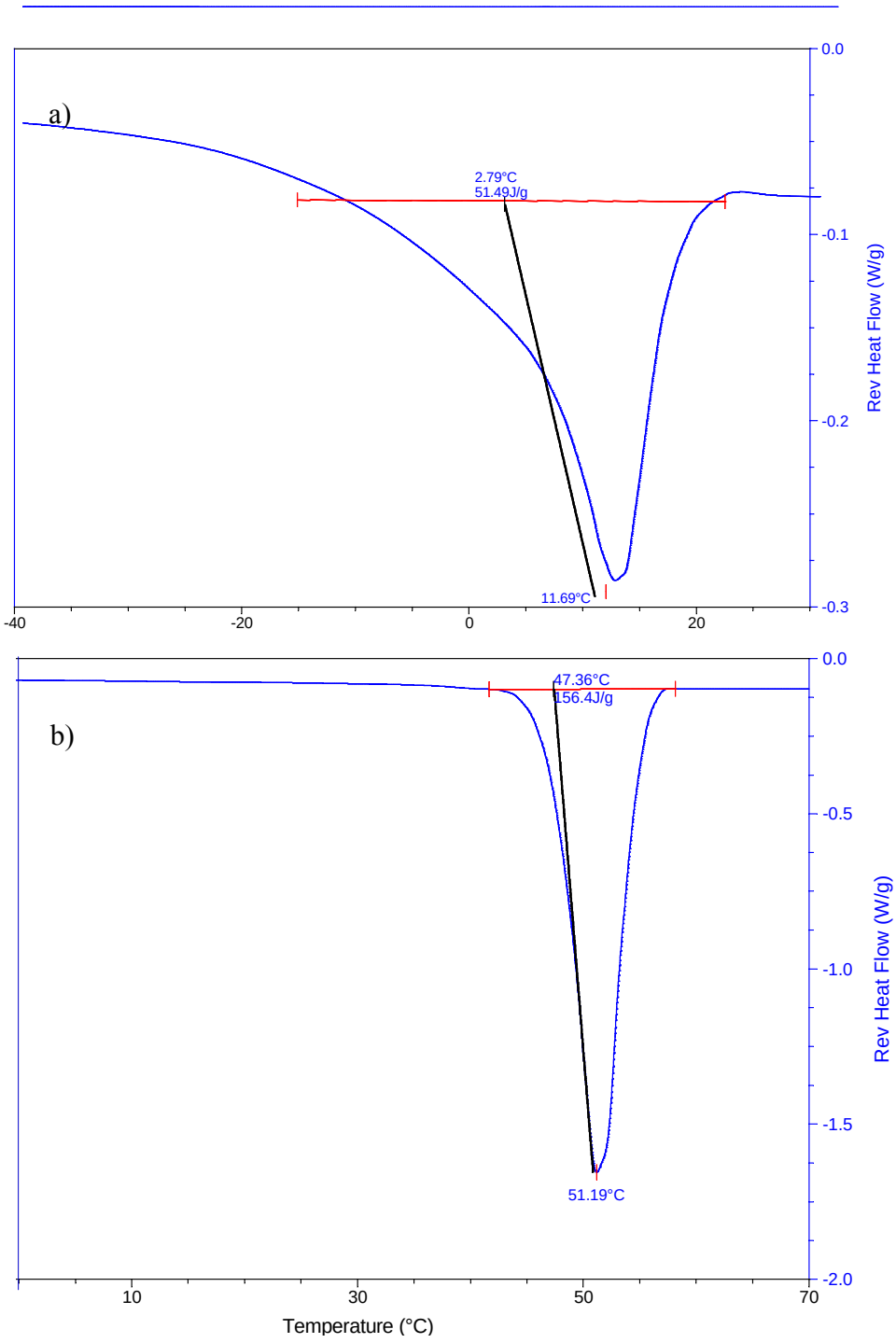


**Figure 3.11: MDSC reverse heat flow vs. temperature showing a) a broad melting peak obtained for Linear i) and b) a narrower peak obtained for Linear ii).**

$T_x$ stands for trifunctional propyl silane ($-(CH_2)_3Si(OR)_3$) where R can be H or $CH_2CH_3$, with x equals to 0, 1, 2, or 3 corresponding to 0, 1, 2, or 3 siloxane bridges per star molecule. A siloxane bridge is a Si-O-Si bond, and based on the star molecule structure shown in Figure 3.3b, several siloxane bridges should be formed. Generally, it can be seen that the silicon resonance peak characteristic of Linear i) ($T_0$) has fully disappeared from the spectra below, which were obtained from various star molecules. This signifies that all linear PEG molecules have been consumed during the making of the stars. We do not see any down shift from $T_0$ which means that there are no hydrolyzed linear molecules ($-(CH_2)_3Si(OH)_x(OCH_2CH_3)_y$ with x+y=3), that is with 1, 2, or 3 hydroxyls groups resulting from the hydrolysis of the original ethoxy groups. As mentioned before, these reactions are characterized by 1-2 ppm down shift from $T_0$ per ethoxy cleaved, i.e. a peak which would be anywhere from 40 to 45 ppm. Additionally, new resonances $T_1$, $T_2$, and $T_3$ appear around -50.22, -58.22, and -66.10 ppm, respectively. It is well known that every siloxane bridge results in 8-9 ppm upper shift[10, 11]. The relative intensities of $T_1$, $T_2$, $T_3$ are indicative of the relative amount of star molecules with 1, 2, and 3 Si-O-Si bridges. Therefore, the stars population created via hydrolysis and condensation reactions is always a statistical distribution between star populations with 1, and/or 2, and/or 3 siloxane bridges. Table 3.2 summarizes the chemical shifts values associated with $T_0$, $T_1$, $T_2$, and $T_3$.

$^1H$ NMR spectra for star-shaped PEG molecules did not show any hydroxyl proton resonance but exhibited some residual ethoxy protons peaks, which suggests that the stars had some ethoxy groups left after hydrolysis and condensation reactions. This is of interest for Chapter IV where we have covalently self-assembled these linear and star molecules onto hydroxylated substrates. Therefore, it is useful to know that both linear and star molecules have similar functionalities (i.e. ethoxy groups) when self-assembling onto substrates.

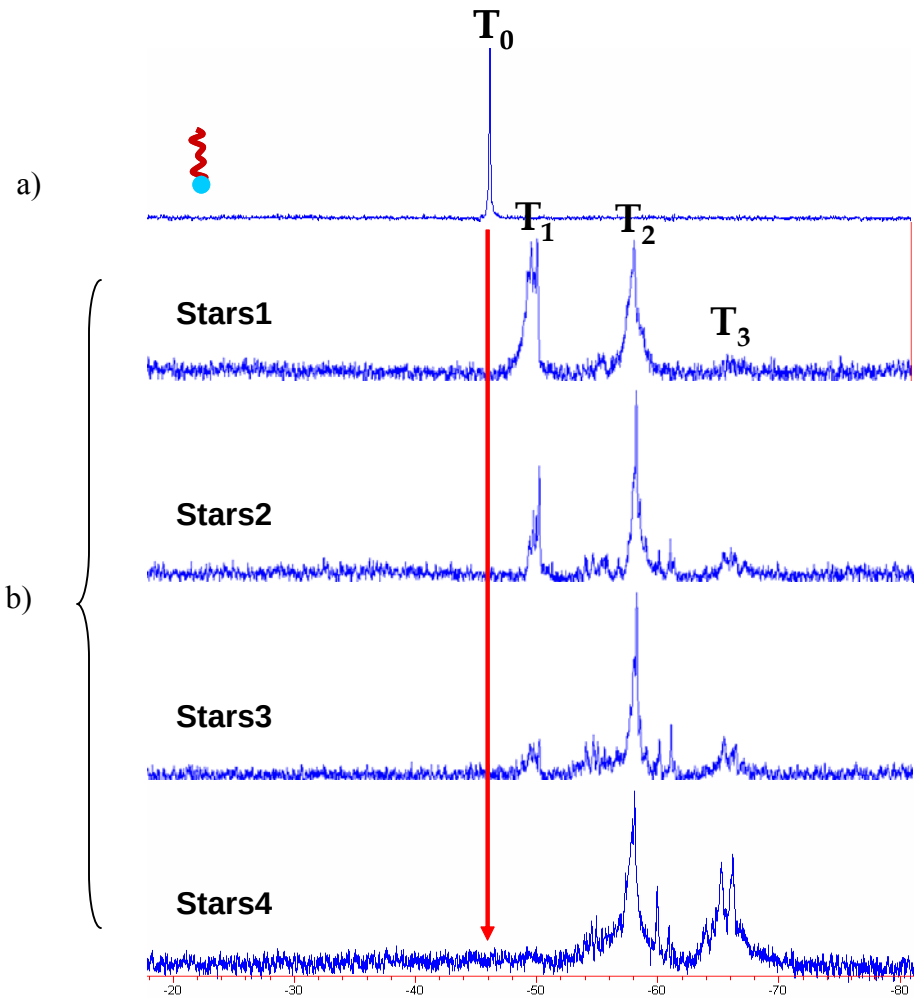


**Figure 3.12: $^{29}$Si NMR spectra obtained for a) Linear i), and b) various star-shaped PEG molecules. This shows the disappearance of the $T_0$ resonance typical of Linear i) and the appearance of several new resonances shifted towards lower frequencies, i.e. $T_1$, $T_2$, and $T_3$.**

**Table 3.2: $^{29}$Si chemical shifts and standard deviations obtained for $T_0$, $T_1$, $T_2$, and $T_3$.**

| Resonance name | $^{29}$Si NMR shifts (ppm) | St. Dev. (ppm) |
|---|---|---|
| $T_0$ Linear i) | -46.27 | 0.11 |
| $T_0$ Linear ii) | -46.07 | 0.09 |
| $T_1$ | -50.22 | 0.17 |
| $T_2$ | -58.22 | 0.12 |
| $T_3$ | -66.05 | 0.18 |

GPC retention times were obtained for various stars and their molecular weight was back calculated using the equation shown on Figure 3.8b. As shown in Figure 3.13 retention times for star-shaped PEG molecules significantly decreased, corresponding to increased molecular weights. Also, we notice that there is a smaller molecular weight tail that appears around 21.5 min, and which corresponds to MPEG 550. This tail was found to decrease as the molar ratio [MPEG]:[IPTES] during the synthesis was decreased from 1.1 to 1. This suggests that there is some unreacted MPEG within the stars population but as seen in Figure 3.13, it only accounts for about 8% of the star population. Besides this tail, all stars molecular weight distribution appear well defined and of low polydispersity. Also, Linear ii) falls within the molecular weight of the various stars we have synthesized here, satisfying our hypothesis of matching molecular weight.

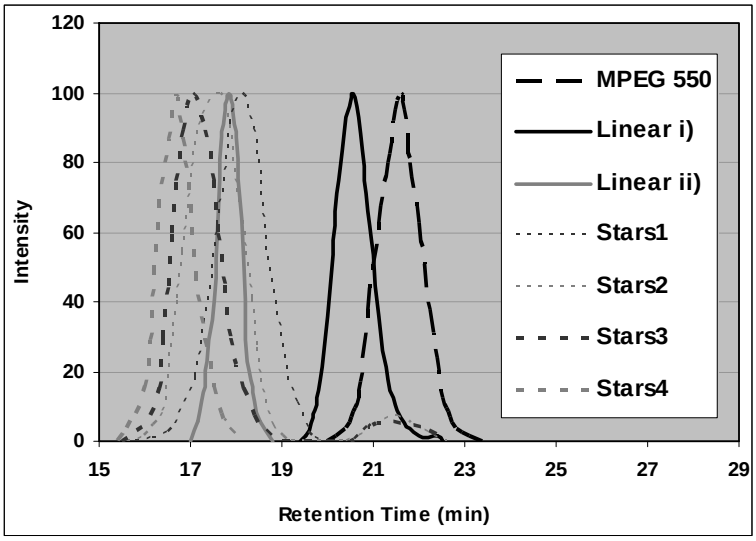


**Figure 3.13: Retention times obtained for Linear i) and ii) and various star-shaped PEG molecules as measured with GPC. The distributions are plotted along with that of MPEG 550.**

It has been reported that branched molecules, i.e. stars, which have different geometry compared to linear molecules, diffuse within a solvent at different rate[14]. GPC retention times may be affected by different diffusivities arising from various molecular geometries and care must be taken in reporting data when the system has been calibrated with linear molecules. Huang reported than 4-arm PEG stars may diffuse 18% faster than linear molecules of similar overall molecular weight[14] based on an 18% smaller $R_G$.

This implies that the star-shaped PEG molecules synthesized here may also travel about 20 % faster than Linear ii) due to smaller $R_G$. This means that the decreased seen in GPC retention times may be inflated by star's smaller $R_G$. Therefore, the molecular weight back calculated from GPC's retention times may be about 20 % higher than it really is. Table 3.3 lists the observed $M_n$ values using the equation in Figure 3.3b, the corrected $M_n$ values after applying a 20% correction factor, and the expected number of arms calculated by dividing the $M_n$ (either "observed" or "corrected") by the molecular weight of 1 arm (640 g/mol). Stars1, 2, 3, and 4 are the same stars as those represented in Figure 3.12. Considering the $^{29}$Si NMR data that we presented just above for these star molecules, the corrected molecular weights listed in Table 3.3 appear to make more sense, as even for Stars4, we observed an equivalent distribution of $T_2$ and $T_3$ resonances (see Figure 3.12). This suggests that Stars4 would be composed of 2 populations of stars with respectively 2 and 3 siloxane bridges, i.e. 3 and 4-arm stars.

**Table 3.3: Measured (by GPC) and corrected $M_n$ values obtained for various star molecules. A 20% correction factor was also applied based on the literature (see text). Stars1, 2, 3, and 4 correspond to the star molecules represented in Figure 3.12.**

| Architecture | Measured $M_n$ (g/mol) | Corrected $M_n$ (g/mol) | Expected # of arms [a] |
|---|---|---|---|
| Stars1 | 2059 ± 20 | 1647 ± 16 | 3.2 – 2.6 |
| Stars2 | 2640 ± 07 | 2112 ± 06 | 4.1 – 3.3 |
| Stars3 | 3249 ± 42 | 2600 ± 34 | 5.1 – 4.0 |
| Stars4 | 3727 ± 20 | 2982 ± 16 | 5.8 – 4.6 |

**[a] The expected number of arms listed were calculated by dividing the Measured and Corrected $M_n$ by the molecular weight of 1 arm (640 g/mol). The 1st number corresponds to the expected value based on our GPC measurements while the 2nd is the corrected after applying a correction factor (see text).**

Viswanathan[7] have characterized star-shaped polymers using $^{29}$Si NMR and found that resonances $T_1$ and $T_2$ led to star polymers with about 3.5 to 4.2 arms based on GPC molecular weight measurements. This study also suggests that there should be some errors associated with the measurement of star-shaped polymer molecular weights using a GPC system primarily calibrated with linear molecules. Based on these observations, and assuming that the data provided by $^{29}$Si NMR are more accurate than those arising from

GPC measurements, we can calculate the predicted number of arms for Stars1, 2, 3, and 4, predicted $M_n$ for those, and finally back calculate the error associated with GPC $M_n$ observations for stars. The results are listed in Table 3.4. Very significant errors can be deducted, which range from 22 to 41 %.

**Table 3.4: Predicted $M_n$ for Stars1, 2, 3, and 4 based on the number of arms observed by $^{29}$Si NMR and based on $T_1$, $T_2$, $T_3$ relative intensities. The error associated with stars's molecular weight determination using the GPC system calibrated with linear PEG polymers was calculated by comparing the $M_n$ listed in columns 3 and 4.**

| Architecture | Observed # of arms by $^{29}$Si NMR | Predicted $M_n$ (g/mol) based on $^{29}$Si NMR | Observed GPC $M_n$ (g/mol) | Error from GPC (%) |
|---|---|---|---|---|
| Stars1 | 2.5 | 1600 | 2059 ± 20 | 22 |
| Stars2 | 2.7 | 1728 | 2640 ± 07 | 34 |
| Stars3 | 3.0 | 1920 | 3249 ± 42 | 41 |
| Stars4 | 3.5 | 2240 | 3727 ± 20 | 40 |

The melting temperature of Stars4 was performed using DSC. 3 different batches were used to calculate their average $T_m$ and standard deviation. According to $^{29}$Si NMR data Stars4 should have between 3 and 4 arms. Table 3.5 lists the observed $T_m$ values for Stars4 in comparison with those obtained for MPEG 550 and 1900, as well as Linear i) and ii). With an average $T_m$ value of 17.28 ± 0.69°C, Stars4 have a melting temperature above that of Linear i) ($T_m$=12.11 ± 0.59°C), which was the linear PEG molecules used to form Stars4 by condensation. Figure 3.14 plots $T_m$ values obtained for MPEG 550 and 1900, Linear i) and ii), and Stars4. Calculating the $T_m$ FWHM for Stars4 gave 7.9 ± 0.57°C, which was pretty close to the width observed for Linear i) (9.90 ± 0.99°C) constituting the arms of Stars4. Ethoxysilane (-Si($OCH_2CH_3$)$_3$) hydrolysis and condensation into multiple siloxane (Si-O-Si) linked branches is a sol-gel process[15] which results in a network. Additionally, the possible hydrogen bonds existing between carbonyl (C=O) and the amine (NH) moieties may slightly reinforce the mechanical properties of this network. Visually, the sol-gel process was witnessed by an increase of the star PEG viscosity compared to that of the linear PEG molecules after drying solutions in a vacuum oven overnight. This data emphasizes that although Stars4 and Linear ii) exhibit similar molecular weights (i.e. 2240 g/mol and 2393 ± 28 g/mol,

respectively) Stars4 is a gel-like material at room temperature but Linear ii) has a solid-flaky appearance ($T_m$=50.45 ± 0.69°C).

**Table 3.5: Measured $T_m$ values for Linear i), Linear ii), Stars4, MPEG 550 and 1900.**

| Name | Averaged $T_m$ (°C) | St. Dev. (°C) |
|---|---|---|
| MPEG 550 | 18.23 | 2.51 |
| Linear i) | 12.11 | 0.59 |
| Stars4 | 17.28 | 0.69 |
| MPEG 1900 | 52.26 | 0.36 |
| Linear ii) | 50.45 | 0.69 |

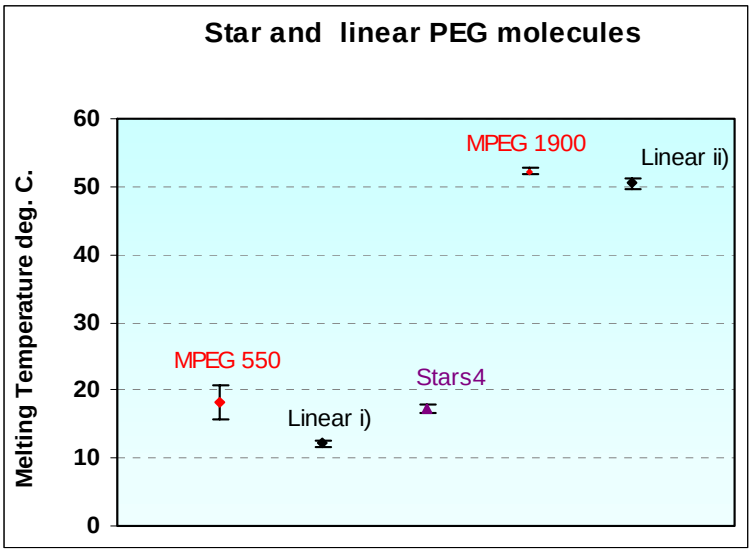


**Figure 3.14: Plot of $T_m$ values obtained for MPEG 550 and 1900, Linear i) and ii), and Stars4 molecules using MDSC.**

Dynamic Light Scattering (DLS) was used to measure the hydrodynamic diameters ($d_h$) of Stars4 molecules in dilute THF solutions. Below this molecular weight, the probability of scattered photons arising from the same molecule may have been too small, therefore decreasing scattering intensity. Small amount of contaminants may also tremendously affect the measured $d_h$ especially when very small molecular weights are concerned.

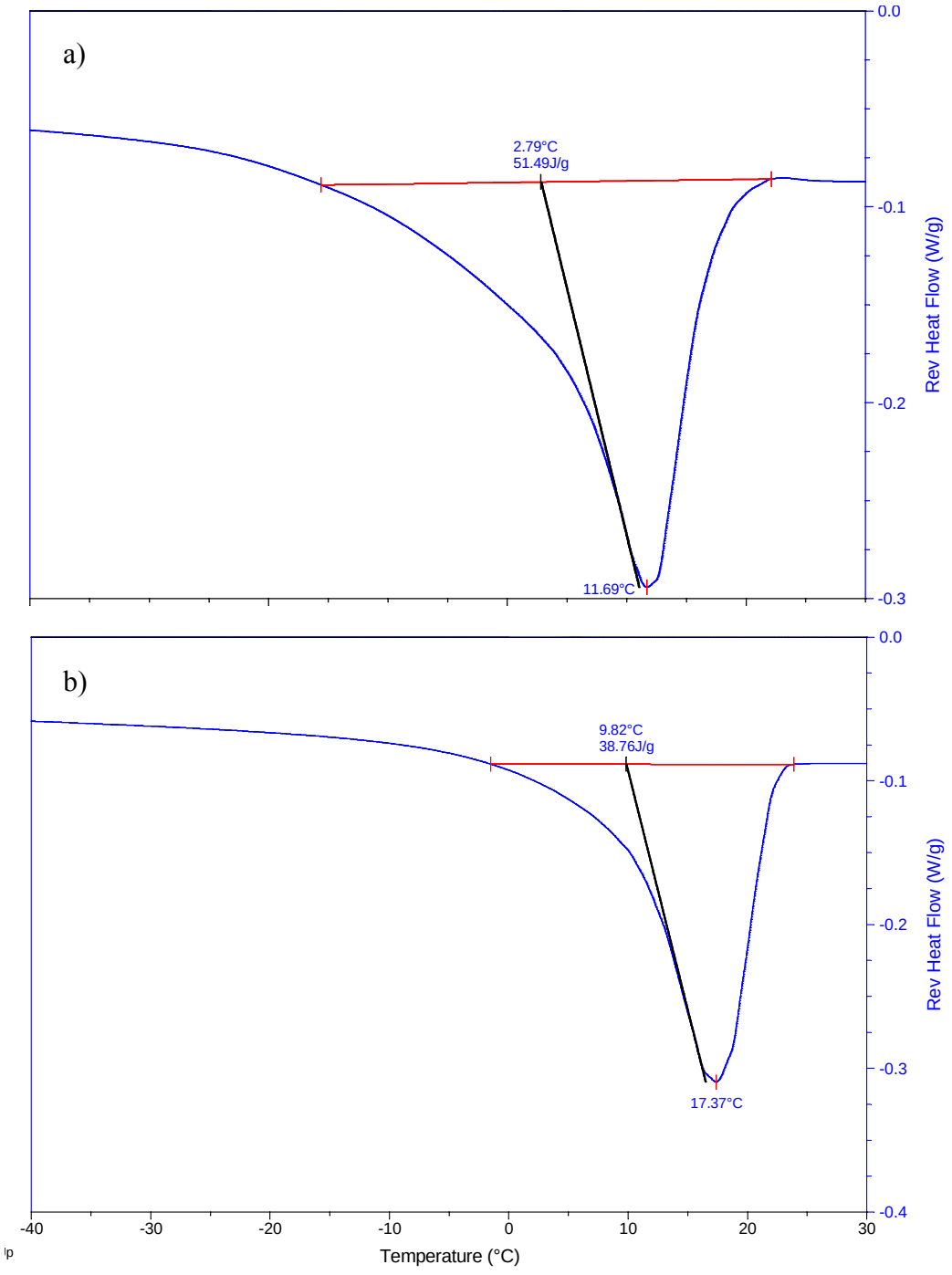


**Figure 3.15: MDSC reverse heat flow vs. temperature showing that a) the broad melting peak characterizing Linear i) molecules is conserved during b) the formation of Stars4 molecules.**

This may also explain the fairly large variation associated with the $d_h$ value obtained for various Stars4. 7 measurements were taken and $d_h$ was found to be equal to 7.06 ± 0.88 nm. However, we can compare this measured $d_h$ to theoretical data. $R_G$ values for linear PEG molecules of molecular weights similar to those considered here have been reported[16, 17]. Fitting these data to a $R_G$ vs. $M_n$ function leads to a very good fit with a power law function $y = 0.0222x^{0.5822}$ where $y$ is $R_G$ and $x$ is the molecular weight of various PEGs. This fitted power law function is shown in Figure 3.16.

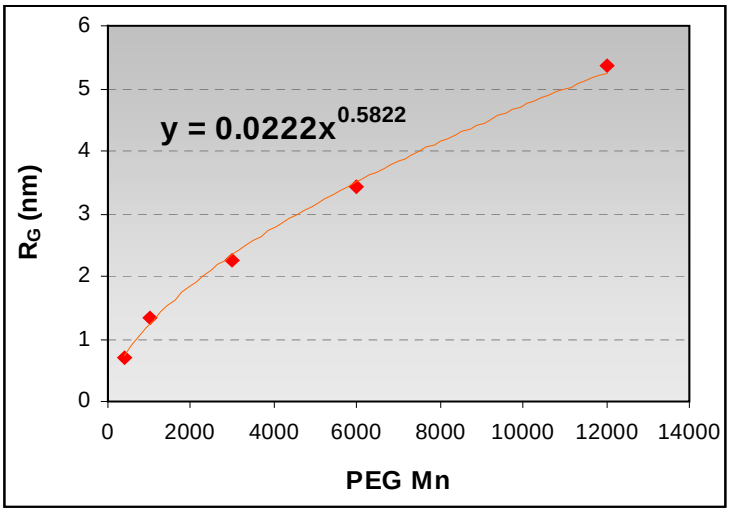


**Figure 3.16: Power law function fitted to $R_G$ vs. $M_n$ for several PEG molecules. These data points are averages calculated from data reported in [16-17].**

Using this power law function we may calculate the theoretical $R_G$ associated with Linear ii) and with the repeating branch within Stars4 (i.e. $M_n$=640 g/mol). These $R_G$ were found to be equal to 2.07 and 0.96 nm for $R_G^{Linear\ ii)}$ and $R_G^{branch}$, respectively. Then, using $R_G^{branch}$ we can calculate the theoretical $R_G^{Stars4}$ dissolved in a good solvent based on the following equation[5]:

$$\log\left(\frac{R_G^{Stars4}}{R_G^{branch}}\right) = 0.1312 * \log(f) + 0.1910 \qquad (2)$$

where $R_G^{branch}$ is assumed to be 0.96 nm, $f$ the functionality Stars4 and was assumed to be 3.5, that is the number of arms calculated from $^{29}$Si NMR data). This yields a $R_G^{Stars4}$ value of 1.79 nm. Assuming that for random coil polymers in a good solvent, the $R_h/R_G$ ratio is about 2[18], $R_h$ for Stars4 should be around 3.58 nm, meaning that $d_h$ should be about 7.16 nm. This agrees very well with the measured value of 7.06 ± 088 nm. According to Huang *et al*[14] 10 000 g/mol 4-arm PEG molecules should have $R_G$ 18% lower than that of a linear PEG molecule with equivalent total molecular weight. Linear ii) was calculated to have $R_G^{Linear\ ii)}$=2.07 nm, whereas $R_G^{Stars4}$=1.79 nm. Therefore, as expected, $R_G^{Stars4}$ is about 16% smaller than $R_G^{Linear\ ii)}$. A summary of calculated and measured $R_G$, $R_h$, and $D_h$ values for Linear ii), 1 branch (repeating unit of Stars4), and Stars4 PEG molecules are presented in Table 3.6.

**Table 3.6: $R_G$, $R_h$, and $D_h$ values (calculated (Calc.) and measured by DLS) reported for Stars4 PEG molecules. Calc. $R_h$ was calculated based on a $R_h/R_G$ ratio equal to 2, which is suitable for molecules dissolved in a good solvent (see text).**

| Architecture | Calc. $R_G$ (nm) | Calc. $R_h$ (nm) | Calc. $D_h$ (nm) | DLS $D_h$ (nm) |
|---|---|---|---|---|
| Linear ii) | 2.07 | - | - | - |
| Branch | 0.96 | - | - | - |
| Stars4 | 1.79 | 3.58 | 7.16 | 7.06 ± 0.88 |

A summary of the characteristics of linear triethoxysilane-functionalized PEG molecules, Linear i) and Linear ii), is showed in Table 3.7.

**Table 3.7: Summary of various properties for Linear i) and ii), and Stars4 PEG molecules**

| Architecture | Linear i) | Linear ii) | Stars4 |
|---|---|---|---|
| $M_n$ (g/mol) | 757 ± 07 | 2393 ± 28 | 2240 |
| Expected # of arms | 1 | 1 | 3.5 |
| $T_m$ (°C) | 12.11 ± 0.59 | 50.45 ± 0.69 | 17.28 ± 0.69 |
| $T_m$ FWHM (°C) | 9.90 ± 0.99 | 4.32 ± 0.40 | 7.9 ± 0.57 |
| Calc. $R_G$ (nm) | 1.09 | 2.07 | 1.79 |
| DLS $D_h$ (nm) | - | - | 7.06 ± 0.88 |

## D. *Conclusion*

In conclusion, we have synthesized and characterized linear and various star-shaped PEG derivatives comprising triethoxysilane functionalities, which therefore may potentially be covalently grafted onto hydroxylated substrates. This has been performed and is the topic of Chapter IV. Triethoxysilane functionalization on linear PEG molecules was found to be quantitative as neither residual hydroxyl (from PEG) nor residual isocyanate (from IPTES) resonances were observed with proton- and carbon-NMR. Premature alcoholysis and hydrolysis of ethoxy groups on these functionalized linear PEG molecules was prevented as seen by silicon-NMR. Stars comprised of 2 to 4 arms were successfully formed using hydrolysis and condensation reactions in acidic water between functionalized linear molecules. Although these reactions are rather slow (~20 hours), they constitute a convenient way to form star polymers at room temperature and lead to fairly well defined stars with narrow polydispersities and with up to about 4 arms. Using NMR spectroscopy and GPC, we have demonstrated that these PEG molecules with different architectures are both characterized by molecular weights of around 2400 g/mol, satisfying our matching molecular weight hypothesis. Although these linear and star PEG oligomers have matching molecular weights, their melting temperatures are significantly different, stars having a much lower melting point than linear molecules. At room temperature, the stars have gel-like appearance, while the linear molecules of similar weight are flaky. Several reports, including this one, have reported on the erroneous determination of Star polymers $M_n$ using a GPC system calibrated with linear molecules. We found errors of up to 40 %, which is why Stars $M_n$ estimated from silicon NMR spectroscopy were thought more reliable. Stars molecular weight which was estimated using silicon NMR was used to calculate theoretical hydrodynamic diameter ($d_h$) for these stars molecules, which agreed very well with the measured $d_h$ values using DLS.

**References:**


1. Jeon, S. I.; Lee, J. H.; Andrade, J. D.; De Gennes, P. G., *Protein-Surface Interactions in the Presence of Polyethylene Oxide. I. Simplified Theory.* J. Colloid Interface Sci., 1991. **142**: p. 149-158.
2. Jeon, S. I.; Andrade, J. D., *Protein-Surface Interactions in the Presence of Polyethylene Oxide. II. Effect of Protein Size.* J. Colloid Interface Sci., 1991. **142**: p. 159-166.
3. Morra, M. J., *On the molecular basis of fouling resistance.* J. Biomater. Sci. Polymer Edn., 2000. **11**: p. 547-569.
4. Fick, J.; Steitz, R.; Leiner, V.; Tokumitsu, S.; Himmelhaus, M.; Grunze, M., *Swelling Behavior of Self-Assembled Monolayers of Alkanethiol-Terminated Poly(ethylene glycol): A Neutron Reflectometry Study.* Langmuir, 2004. **20**: p. 3848-3853.
5. Sofia, S. J.; Premnath, V.; Merrill, E. W., *Poly(ethylene oxide) Grafted to Silicon Surfaces: Grafting Density and Protein Adsorption.* Macromolecules, 1998. **31**: p. 5059-5070.
6. Irvine, D. J.; Mayes, A. M.; Satija, S. K.; Barker, J. G.; Sofia-Allgor, S. J.; Griffith, L. G., *Comparison of tethered star and linear poly(ethylene oxide) for control of biomaterials surface properties.* J. Biomed. Mater. Res., 1998. **40**: p. 498-509.
7. Viswanathan, K.; Long, T. E.; Ward, T. C., *Silicon Surface Modification with Trialkoxysilyl-Functionalized Star-Shaped Polymers.* J. Poly. Sci. Part A: Poly. Chem., 2005. **43**: p. 3655-3666.
8. Karikari, A. S.; Edwards, W. F.; Mecham, J. B.; Long, T. E., *Influence of Peripheral Hydrogen Bonding on the Mechanical Properties of Photo-Cross-Linked Star-Shaped Poly(D,L-lactide) Networks.* Biomacromolecules, 2005. **6**: p. 2866-2874.
9. Viswanathan, K.; Ozhalici, H.; Elkins, C. L.; Heisey, C.; Ward, T. C.; Long, T. E., *Multiple Hydrogen Bonding for Reversible Polymer Surface Adhesion.* Langmuir, 2006. **22**: p. 1099-1105.
10. Vrancken, K. C.; Van der Voort, P.; Gillis-D'Hamers, I.; Vansant, E. F.; Grobet, P., *Influence of water in the reaction of gama-aminopropyltriethoxysilane with silica gel.* J. Chem. Soc. Faraday Trans., 1992. **88**: p. 3197-3200.
11. Tingaut, P.; Weigenand, O.; Militz, H.; De Jeso, B.; Sebe, G., *Functionalisation of wood by reaction with 3-isocyanatopropyltriethoxysilane: Grafting and hydrolysis of the triethoxysilane end groups.* Holzforschung, 2005. **59**: p. 397-404.
12. Zhou, H.; Wilkes, G. L., *Comparison of lamellar thickness and its distribution determined from d.s.c, SAXS, TEM and AFM for high-density polyethylene films having a stacked lamellar morphology.* Polymer, 1997. **38**: p. 5735-5747.
13. Harris, J. M., *Poly(ethylene glycol) chemistry: biotechnical and biomedical applications*, ed. J.M. Harris. 1992: Plenum Press.
14. Huang, H.; Fulchiero, E. C.; Penn, L. S., *Comparison of tethering of linear and four-arm poly(ethylene oxide).* Macromolecules, 2005. **38**: p. 1028-1030.

15. Long, T. E.; Kelts, L. W.; Turner, S. R.; Wesson, J. A.; Mourey, T. H., *Synthesis and Characteriaztion of Well-Defined Star Polymers via a Controlled Sol-Gel Process.* Macromolecules, 1991. **24**: p. 1431-1434.
16. Kulkarni, A. M.; Chatterjee, A. P.; Schweizer, K. S.; Zukoski, C. F., *Effects of polyethylene glycol on protein interactions.* J. Chem. Phys., 2000. **113**: p. 9863-9873.
17. Bhat, R.; Timasheef, S. N., *Steric exclusion is the principal source of the preferential hydration of proteins in the presence of polyethylene glycols.* Protein Science, 1992. **1**: p. 1133-1143.
18. Neradovic, D.; Soga, O.; Van Nostrum, C. F.; Hennink, W. E., *The effect of the processing and formulation parameters on the size of nanoparticles based on block copolymers of poly(ethylene glycol) and poly(N-isopropylacrylamide) with and without hydrolytically sensitive groups.* Biomaterials, 2004. **25**: p. 2409-2418.

# CHAPTER IV.

## SELF-ASSEMBLY OF MATCHING MOLECULAR WEIGHT LINEAR AND STAR-SHAPED POLYETHYLENE GLYCOL MOLECULES AND THEIR ALBUMIN ADSORPTION PROPERTIES

### A. *Introduction*

Protein adsorption properties of tethered polyethylene glycol (PEG) have been extensively studied over the past decades, and PEG-tethered surfaces have emerged as protein resistant surfaces. Several hypotheses and mechanisms have been proposed in order to make sense of the unique properties exhibited by PEG. Some of the unique characteristics of PEG molecules include its water solubility and its steric repulsion properties, which are both believed to contribute to PEG's protein resistance ability[1-4].

PEG is a semicrystalline polymer which exists in a wide range of molecular weights from 200 up to several millions g/mol. While PEG 200 (200 g/mol) is liquid at room temperature, PEG 600 (600 g/mol) is a waxy solid, PEG 2000 (2000 g/mol) is formed of waxy chips, and PEG 8000 (8000 g/mol) and above may be comprised of a crystalline powder. This results from the fact that the melting temperature of PEG in its solid state proportionally increases as a function of its molecular weight up to a maximum of about 70°C[5]. Table 4.1 shows melting points and form of PEGs with various molecular weights. In the crystalline state, PEG chains are arranged according to a monoclinic crystal structure characterized by the following dimensions: a=7.96 Å, b=13.11 Å, c=19.39 Å, and β=124°48'. This monoclinic unit cell is comprised of 4 PEG chains, each one comprising 7 ($CH_2CH_2O$) monomer units, and 2 helical turns. This yields a monomer unit size averaging 2.77 Å in length, which is consistent with values reported in the literature.

PEG has very unique solubility properties in water across this molecular weight range. The helical crystal structure of PEG chains with trans-gauche-trans conformation has been reported to fit very well within a hexagonal water structure[6]. In fact, PEG chains are believed to be more ordered when dissolved in water than when dissolved in organic solvents such as chloroform or in the melt. This would be due to the PEG chain conformation which may be accommodated in hexagonal or cubic water lattice structures (i.e. ice).

**Table 4.1: Melting temperatures and appearance of PEG molecules for various molecular weights.**

| Molecular weight | Melting point (°C) | Appearance at room temperature |
|---|---|---|
| 200 | -65 | liquid |
| 600 | 20 to 25 | waxy solid |
| 2000 | 52 to 54 | waxy chips |
| 8000 to several millions | 65 to 70 | crystalline powder |

Even the largest molecular weights highly crystalline molecules exhibit high water dissolution in a unique manner due to the melting of PEG crystals. In fact, it is thought that PEG solubility in water depends on temperature. What results is a closed immiscibility loop[7], where a low and high critical solution temperatures are known to occur. The low critical temperature (LCT) is also known as the cloud point which depends on molecular weight, concentration, and pH values. While PEG 1900 cloud point is around 180°C, a 10 % potassium sulfate salt addition leads to a significant cloud point decrease. This closed immiscibility loop means that PEG can exhibit some hydrophobic properties although it is a widely recognized hydrophilic polymer. PEG is therefore recognized for its interesting solubility and swelling properties in water.

Dipole relaxation measurements and Nuclear Magnetic Resonance (NMR) proton relaxation rate studies have been performed to study the mobility of PEG dissolved in water solutions[8]. It was found that longer PEG chains, i.e. chains with more than about 100 monomer units, have relaxation rates that are not affected by end group dynamics. However, shorter PEG chain relaxation rates may be affected by end group contributions.

PEG chains comprised of more than about 100 monomer units were also found to have segmental motions that were independent of PEG molecular weight. In contrast, smaller molecular weights had relaxation rates that depended on end group dynamics. Segmental motions may also depend on PEG chain length. In general, PEG chains with more than about 100 units have higher mobility and this mobility is independent of molecular weights[9, 10]. Note that similar mobility trends were found for hydrated PEG films, implying that grafted PEG chains may relax in a fashion similar to unattached PEG chains in aqueous solution. Below chain lengths of about 100, mobility (or relaxation rates) may be lower and generally depends on PEG molecular weight and end group dynamics.

Steric repulsion is believed to arise from the compression of longer PEG chains when a protein is approaching the interface, while shorter PEG chains may mostly benefit from PEG-water interaction properties. For longer chains (> ~100 monomer units) in the brush conformation[1], grafting density was found to greatly affect shielding from the underlying material, and affected protein resistance. The change in free energy of the protein-PEGylated substrate interface was calculated as the sum of the free energies arising from steric repulsion and hydrophobic attractions between the advancing protein and the PEGylated surface. The short-range van der Waals interactions were neglected because they were outweighed by the long-range hydrophobic interactions. The steric repulsion free energy had osmotic and elastic contributions. From these free energy calculations, it was concluded that PEG surface density and chain length are important factors accounting for protein repulsion, and that high PEG surface density is especially important for repelling smaller proteins. However, shorter PEG chains not in the brush structure but more randomly oriented may not exhibit significant steric exclusion due to small exclusion volumes. Instead, their protein resistance appears to be highly dependent on PEG chains conformation (helical, amorphous or planar)[11, 12] and may arise from interfacial water layer stabilization, emphasizing the importance of PEG-water hydration and hydrogen bonding properties[12-14]. Wang *et al*[14]found that the PEG crystalline helical conformation forms stronger hydrogen bonds with water molecules, whereas the planar structure allows for weaker hydrogen bonds. Additionally, protein resistance may

also arise from electrostatic repulsion, a contribution that is absent with longer PEG chains[13].

Crystalline and amorphous (random coils) grafted linear PEG chains comprised of between 2 and 450 ethylene glycol units have been shown to successfully repel proteins of various different sizes including 12 000 g/mol (cytochrome-c[15, 16]), 15 000 g/mol (lysozyme, ribonuclease[17]), 55 000 g/mol (pyruvate kynase[18]), albumin (68 000 g/mol[15, 16]), 340 000 g/mol (fibrinogen[12, 17]), and 500 000 g/mol (fibronectin[15]). Stars-shaped PEG molecules with more than 1 order of magnitude greater PEG chain density per unit volume failed to repel proteins near the surface, where the PEG segment density is lower[16]. Contrarily, tethered linear molecules, which were also overlapping, presented higher PEG segment density near the substrate and better resisted protein adsorption. While the primary protein resistance mechanisms of very short PEG chains (<6 monomer units) are believed to comprise electrostatic repulsion and interfacial water layer stabilization, much longer PEG chains (>100 monomer units) appear to take advantage of their steric repulsion ability.

In Chapter III, we have synthesized and characterized linear and star-shaped PEG molecules with matching molecular weights around 2400 g/mol, comprising about 43 ethylene glycol units and triethoxysilane functionalities. This relatively small molecular weight falls in between those mostly studied and reported in the literature. This smaller molecular weight allows a decrease of the steric hindrance associated with much larger molecular weight PEG stars (i.e. hard-sphere like structure)[15, 16], thereby increasing PEG segment density near the substrate. Protein adsorption of these self-assembled star-shaped PEG molecules will be compared to that of linear PEG molecules with matching molecular weight. Additionally, core-functionalized PEG stars comprising about 4 arms permit the increase of PEG segment mobility near the surface compared to end-functionalized PEG stars as those studied by Sofia[15] and Irvine[16]. This increased mobility near the surface may increase protein resistance.

Here, the intent was to graft the matching molecular weight linear and star-shaped PEG functionalized molecules onto silicon wafers substrates. Comparative study of human albumin adsorption will be conducted using X-Ray photoelectron Spectroscopy (XPS), ellipsometry, and goniometry.

## B. *Materials and Methods*

### 1. Linear and star-shaped triethoxysilane PEG derivatives

In Chapter III, the synthesis of well defined linear and star-shaped PEG molecules was demonstrated. These were comprised of triethoxysilane functionalities, enabling the covalent grafting of these molecules on hydroxylated substrates. The protein adsorption study on star-shaped films presented here was limited to PEG stars comprised of 3 to 4 arms, which were the stars with the highest number of arms that could be synthesized using ethoxy group hydrolysis and condensation reactions at room temperature and for about 20 hrs. Based on $^{29}$Si NMR, these stars were estimated to have a molecular weight of about 2240 g/mol, while the synthesized linear PEG molecules had a molecular weight of about 2393 g/mol. Thus, these linear and star-shaped PEG molecules exhibited matching molecular weights. Although the linear and star-shaped PEG polymers have matching molecular weights, they exhibit significantly different melting points and hence structure at room temperature. While stars were found to have low melting point of about 17 °C, linear molecules had a melting temperature of about 50°C. At room temperature, therefore, the stars have gel-like properties, while the linear molecules of similar weight are flaky. While linear PEG had a calculated $R_G$ of about 2.07 nm, that of the star molecules was around 1.79 nm.

### 2. Cleaning and hydrophilization of substrates

Silicon wafers were cut into 2.5x1.25 cm$^2$ pieces, and were sonicated in acetone for 30 minutes and ethanol for 5 minutes to remove microorganisms and dust particles. A 5

minute sonication in deionized water ensured the removal of any residual organic solvent on the surface. The pieces were dried with ultra-pure nitrogen gas, and immediately immersed in a $H_2O_2$:$H_2SO_4$ 5:2 v/v piranha solution for 40 min at 75°C. The piranha solution was made fresh each time to prevent the decomposition of hydrogen peroxide into hydronium ions and to ensure its full oxidizing power. This step further removed any organic residue, but also hydrophilized the silicon substrates, i.e. added hydroxyl functionalities on the surface. These hydroxyl groups were subsequently utilized for covalently grafting triethoxysilane-functionalized linear and star-shaped PEG molecules. This hydrophilization renders the substrates very hydrophilic, which was checked by measuring the contact angle before and after piranha solution treatment. Wafer pieces were then profusely rinsed in deionized water, rinsed with methanol to remove any residual water at the surface, and finally dried with a stream of nitrogen gas. These cleaned and hydrophilized wafers were immediately used for the PEG grafting process.

3. Grafted linear and star-shaped PEG chains

Triethoxysilane-functionalized linear and star-shaped PEG molecules were grafted onto silicon wafer at 2 different PEG concentrations using a rotational table to ensure film homogeneity. The critical concentrations for these linear and star polymers corresponded to the concentration at which molecules in solutions start overlapping were calculated. The chosen concentrations (0.5 and 15 % w/v in methanol) were below and above this calculated critical concentration. 50 mg or 1.5 g of either linear or star PEG was added to 10 ml of anhydrous methanol leading to 0.5 and 15% w/v solutions. 2 silicon pieces were immersed in each solution concentration and grafting was allowed to proceed for 16 hrs on a rotational table at room temperature. At least 3 different batches were made using different batches of linear and star PEG every time. Grafting was expected to take place via ethoxy alcoholysis and condensation reactions with hydroxyl functionalities on silicon substrates. Following the grafting reaction, the substrates were taken out of solution and sonicated in methanol to remove any physisorbed PEG molecules. These

were finally placed in an oven at 40°C for at least 36 hrs to reinforce film robustness by driving more condensation reactions.

### 4. Human albumin adsorption on PEGylated surfaces

Human serum albumins (68 000 g/mol) (HSA) and phosphate buffered saline pH 7.4 were obtained from Sigma-Aldrich. Phosphate buffered saline powder was mixed with deionized water at 25°C to yield a 0.01M phosphate buffered saline (PBS), comprising 0.138M NaCl and 0.0027M KCl. Albumins were dissolved in the saline solution at the physiological concentration of 4 mg/ml. These albumin solutions were gently agitated until full dissolution. Wafer pieces comprising linear or star-shaped PEG films were profusely rinsed with the saline solution and immediately immersed in albumin solutions. Adsorption was allowed to proceed for 18 hrs at 25°C on a rotating table to mimic proteins circulation. This ensured that protein adsorption was homogeneous over the whole surface and that the various surface characterization tools which average signals over a certain spot size would yield repeatable data. After adsorption, the substrates were taken out and rinsed with 1.5 ml of PBS, then with 1 ml of deionized water at 25°C to remove PBS salts, and finally gently dried under a stream of nitrogen. 4 linear and 4 star PEG grafted films were tested for albumin adsorption.

### 5. Characterization of PEGylated substrates and protein adsorption

X-Ray Photoelectron Spectroscopy (XPS) was used to confirm linear and star-shaped PEG attachment to the surface and to calculate film thicknesses. A Perkin-Elmer 5400 apparatus along with monochromatic Mg $K_\alpha$ X-rays ($h\nu$=1253.6 eV) and a take-off angle (angle between surface plane and detector) of 45° were used. The 285.00 eV carbon C1s peak was used as a reference. The XPS sampling depth depends on the take-off-angle and on a given photoelectron attenuation length which depends on the surface chemistry according to:

$$d = \lambda \sin\theta \quad (1)$$

where $d$ is the sampling depth, $\lambda$ the photoelectron attenuation length which can be calculated based on the overlayer chemical composition and on the photoelectron nature, and $\theta$ the take-off-angle, i.e. the photoelectron emission angle between the surface plane and the detector. $\lambda$ was calculated using the NIST Standard Reference Database (version 1.1) and found to be equal to 2.90 nm for C 1s photoelectrons. This value agrees well with values reported in the literature for PEG films[15]. At a 45° take-off-angle, the corresponding sampling depth was found to be equal to 2.05 nm for the grafted PEG films studied here and for the C 1s carbon survey scans. The C 1s carbon signal was deconvulated into separate fitted Gaussian curves and the intensity of the ether carbon peak ($OCH_2CH_2$) at about 286.5 eV was used to calculate the various film thicknesses and estimate grafting densities. A minimum of 3 independent XPS surveys was taken per film architecture (linear vs. star) and per concentration. Albumins contain 15% nitrogen. Therefore, their adsorption on linear and star-shaped PEG films was characterized based on the XPS nitrogen signal intensity. It is worth noting that human serum albumin have been shown to have lower self-binding properties compared to bovine serum albumin[19]. Self-binding properties may result in albumin aggregation in solution and may therefore affect protein adsorption on surfaces. Therefore, human serum albumin should always be used for protein adsorption studies dealing with coatings to be inserted in the human body.

A Beaglehole Picometer Ellipsometer with a 632.8 nm laser wavelength was used to calculate the thickness of PEG and albumin films on silicon wafer substrates. $SiO_2$ (natural silica layer present at the wafer surface) and PEG are characterized by very similar refractive indices and thus were modeled as 1 layer with a 1.455 refractive index. The measurements were performed in air (1.003 for refractive index) and bulk silicon was given a 3.875 refractive index. The $SiO_2$ layer thickness of 4 bare silicon wafers was measured immediately after piranha treatment and the $SiO_2$ thickness was found to be statistically equal to that of natural silica layer on wafers, i.e. 2 nm thick. This silica thickness was subtracted from the total thickness in order to obtain the thickness of the

PEG films only. For albumin film thickness calculations, the same refractive index of 1.455 was assumed which is an appropriate average refractive index for proteins[15]. Again, the thickness of ($SiO_2$+PEG) was subtracted from the total calculated thickness in order to obtain the albumin thickness only. Therefore, for PEGylated surfaces, as well as for albumin-PEGylated surfaces, a 3-medium interface model was assumed comprised of an air layer, a ($SiO_2$ ± PEG ± HSA) layer, and finally a bulk silicon layer with refractive indices of 1.003, 1.455, and 3.875, respectively. 3 measurements at 3 different spots were taken per sample.

Static water contact angles were measured using the sessile drop method using a goniometer and syringed deionized water drops. Water contact angle values were compared between bare silicon wafers, as well as linear and star-shaped PEG films before and after albumin adsorption. 3 measurements were taken per sample.

## C. *Results and discussion*

### 1. Linear PEG film thickness and grafting density

Previously synthesized and characterized (see Chapter III) linear and star-shaped triethoxysilane-functionalized PEG molecules, of matching molecular weight around 2400 g/mol, were covalently self-assembled on silicon wafers. The grafting reaction took place between ethoxy groups from the functionalized PEG molecules and hydroxyls added on the wafers surface during oxidation with the $H_2O_2$:$H_2SO_4$ 5:2 v/v piranha solution. Figure 4.1 illustrates the grafting or covalent self-assembly process, which was conducted using either linear or star-shaped PEG molecules at 2 different concentrations, i.e. 0.5% and 15% w/v. This grafting procedure is expected to lead to the covalent attachment of a single layer of either linear or star-shaped PEG molecules onto silicon wafer substrates.

These 2 different concentrations were estimated to be below and close to the critical concentration corresponding to molecules overlap in solution and calculated according to the following relationship[15, 16]:

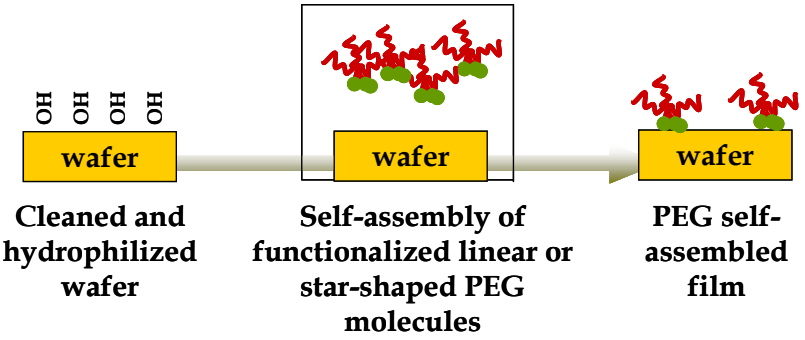


**Figure 4.1: Triethoxysilane functionalized PEG stars grafted to a hydrophilized silicon wafer. The same grafting process was conducted using linear ii) PEG molecules with overall matching molecular weight.**

$$C_{crit} = \left( \frac{M}{N_A \frac{4}{3} \pi R_G^{\,3}} \right) \qquad (2)$$

where $M$ is the molecular weight of the linear or star-shaped PEG molecules, $N_A$ the Avogadro number, and $R_G$ the radius of gyration which was calculated in Chapter III. $C_{crit}$ was calculated for both the linear and star-shaped PEG molecules and found to be equal to 10.8 and 15.5 % for Linear ii) and Stars4, respectively. Therefore, at 0.5% concentration the PEG solutions were dilute, while at 15% concentration both Linear ii) and Stars4 molecules were expected to start overlapping in solution.

As shown in Figure 4.2 a-b, analysis of XPS C 1s spectra confirmed the successful grafting of both linear and star-shaped PEG molecules. The PEG moiety of the film is characterized by the (C-O) peak, while the urethane carbon (O-C=O) arises at around 288 eV, and the inorganic carbon has the lowest binding energy of about 283.9 eV (when C-C

is referenced at 285 eV). Peak intensity is known to decay exponentially with film thickness, resulting in the following relationship[18]:

$$I \propto \exp\left(\frac{-d}{\lambda \sin\theta}\right) \tag{3}$$

where $I$ is the signal intensity, $d$ the overlayer thickness, $\lambda$ the photoelectron attenuation length through the overlayer, and $\theta$ the take-off-angle used when measuring the corresponding signal intensity (i.e. angle between surface plane and detector, 45° here). Therefore, the intensity of the fitted (C-O) peak may be used to calculate PEG films thickness. Because a single PEG layer is considered here, any increase in the (C-O) peak intensity should correspond to an increase in a single layer thickness which may be due to chain conformation changes. Changes in PEG chain conformations often mean that the grafting density of these chains is varying as well. For instance, Figure 4.3 illustrates how both the layer thickness and the layer grafting density increase when grafted PEG chains change from a) a low density pancake, to b) a higher density mushroom, to finally c) a very dense brush conformation. When the PEG solution's concentration increases from 0.5 to 15% w/v, PEG chains are approaching the overlap concentration in solution, and therefore should lead to a thicker PEG single layer with most likely chains overlap. The thickness of ultra-thin overlayers (i.e. less than about 10 nm in thickness) can be calculated using the relationship[15, 18]:

$$\frac{I}{I_0} = 1 - \exp\left(\frac{-d}{\lambda \sin\theta}\right) \tag{4}$$

where $I$ is the intensity of a particular (C-O) peak, $I_0$ the intensity of the same peak obtained for a film thicker than the sampling depth, which was found to be equal to 2.05 nm at 45 ° take-off-angle with the surface chemistry considered here, $d$ the thickness of the overlayer of interest, $\lambda$ the photoelectron attenuation length through the PEG overlayer ($\lambda$=2.90 nm here), and $\theta$ the take-off-angle used when measuring the corresponding signal intensities ($\theta$ =45° here).

a)

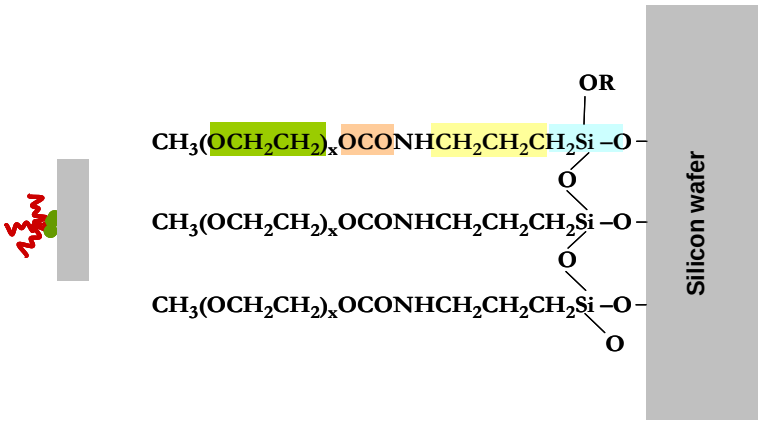


b)

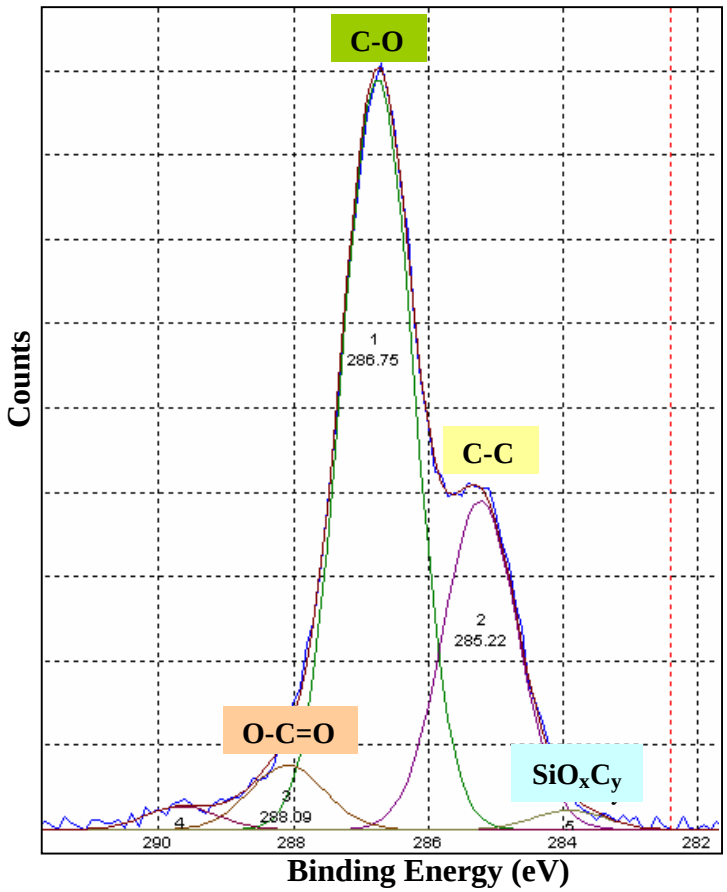


**Figure 4.2: a) Structure of a 3-arm PEG star molecule grafted to a silicon wafer, and b) C 1s XPS spectrum obtained at a 45° take-off-angle for grafted linear PEG molecules (high concentration) on silicon wafer. This shows the PEG ether peak around 286.5 eV, as well as the urethane carbon peak around 288.0 eV, and the inorganic carbon around 283.9 eV. These peaks confirm the successful covalent self-assembly of triethoxysilane linear PEG molecules to hydroxylated silicon wafers.**

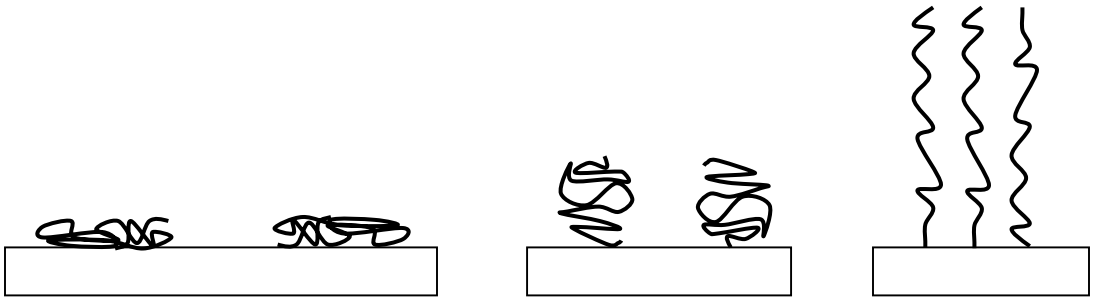


**Figure 4.3: This shows various conformations which PEG molecules may take when grafted to a surface. These include a) pancake, b) mushroom, and c) densely packed brushes. The thickness and grafting density both increase from a) to c).**

$I_0$ constitutes a challenging estimate which is usually calculated based on the intensity of the (C-O) peak obtained for a film with similar chemistry and thicker than the sampling depth, and given this film thickness measured by ellipsometry. $I_0$ may be estimated using equation 4. Alternately, by using equation 4, and given the ellipsometry thickness and the measured (C-O) peak intensity for 6 Linear ii) PEG grafted films, an average value of $I_0$ was calculated and used for estimating PEG films thickness based on (C-O) intensity. There was no statistical difference between the calculated $I_0$ from the 0.5 and 15 % grafting solution, and the average value for $I_0$ was found to be equal to 1908 ± 200 counts.

Additionally, an overlayer grafting density, defined as the area per anchored molecule (molecules/Å$^2$), is defined by[16]:

$$\sigma = 1/L^2 = \left(\frac{h\rho N_A}{M}\right) \tag{5}$$

where $h$ is the overlayer thickness measured by ellipsometry, $\rho$ the molecular mass density, $N_A$ the Avogadro's number, and $M$ the molecular weight of the grafted molecules.

**Table 4.2: PEG ether peak (C-O) intensity as measured with XPS, along with ellipsometry thicknesses for 3 different batches of Linear ii) grafted films from 0.5% and 15% solutions.**

| | Grafted Linear ii) from 0.5% solutions | | | Grafted Linear ii) from 15% solutions | | |
|---|---|---|---|---|---|---|
| XPS (C-O) intensity $I$ (counts) | 811 | 784 | 859 | 678 | 672 | 833 |
| Ellipsometry thickness $d$ (Å) | 14.8 | 12.4 | 12.6 | 12.7 | 12.2 | 12.4 |
| Calculated $I_0$ (counts) | 1844 | 1764 | 2175 | 1440 | 1560 | 1778 |
| $I_0$ average and standard deviation (counts) | 1908 ± 200 | | | | | |

The grafting point separation $L$ is simply expressed as:

$$L = \sqrt{\frac{1}{\sigma}} \tag{6}$$

Given this calculated $I_0$ value and the measured (C-O) intensities for each film, thicknesses were calculated using equation 4 and are shown in Table 4.3. Low grafting densities are sometimes considered to be achieved when the grafting point separation $L$ is much larger than the radius of gyration $R_G$ of the grafted molecules corresponding to a pancake or mushroom conformation[15, 20]. When $L \sim 2R_G$, chains are most likely in the mushroom conformation and begin to overlap. Finally, if $L < R_G$, the film is characterized by densely packed chains in the brush conformation. Other studies have compared $R_G$ with film thickness $d$ to estimate the conformation of the grafted chains[21]. It follows that mushroom conformation is obtained when $d < R_G$, while moderate brush conformation occurs when $d > R_G$.

Due to their thickness range, the linear PEG layers appear to be amorphous in nature rather than crystalline with a helical structure. Fick *et al*[4] studied linear PEG chains of

similar molecular weight and demonstrated that amorphous PEG single layer had a dried thickness around 23 Å as measured by ellipsometry, while crystalline PEG films exhibited a dried thickness of about 105 Å. Table 4.3 shows that for Linear ii) grafted films from 0.5 and 15% solutions, $L < R_G$, which would imply that Linear ii) PEG chains are overlapping and in a fairly dense brush conformation according to[15, 20]. However, it also implies that $d < R_G$, which, according to[21], signifies that a mushroom conformation would be achieved, which may or may not have overlapping chains. This criteria, $d < R_G$, reflects the dried thickness $d$, when the wet thickness should be considered because PEG is known to swell by several orders of magnitude when immersed in water[4]. In fact, Fick[4] measured a wet PEG film thickness of about 60 Å for an amorphous PEG film of similar molecular weight than the one studied here. This corresponds to about 300% increase in wet thickness compared to the dry one. Assuming that the thickness of the Linear ii) PEG film studied here also increases by about 300% lead to $d > R_G$ and to a Linear ii) PEG film in the brush conformation with significant chains overlap.

Both solution concentrations used for the grafting process, 0.5 and 15 % w/v, led to similar (C-O) intensities seen with XPS, and therefore similar thicknesses and grafting densities. This is due to the fact that 50 mg and 1.5 g of triethoxysilane linear PEG molecules were used during the grafting experiments on 2 wafer pieces each measuring $1.25 \times 2.50$ mm$^2$. 50 mg corresponding to about $1.24 \times 10^{19}$ molecules already represents enough molecules to achieve grafted chain overlap. Since the goal was to maximize the grafting density, the films obtained using the 15% Linear ii) PEG solution concentration emphasize that the grafting densities obtained must be the largest possible given these triethoxysilane-functionalized PEG molecules. Additionally, this shows that although the conformation of linear PEG chains was not overlapping vs. overlapping for 0.5 and 15 % solution, respectively, both solutions led to overlapping, grafted, linear PEG chains.

Table 4.4 shows the static water contact angles that were measured on 3 different spots on each sample, for 4 different Linear ii) films, 2 obtained from 0.5% (w/v) PEG solutions, and 2 obtained from 15% (w/v) PEG solutions. It is clear again that no statistical

difference can be seen between the 2 different concentrations because, as mentioned earlier, densely packed PEG chains in the brush conformation were obtained with both concentrations. Therefore, these 4 Linear ii) films were treated as 1 population, and the water contact angle average and standard deviation are reported in Table 4.4 and were found equal to 58.61 ± 3.47°. Comparatively, the water contact angle of bare silicon wafers and hydroxylated silicon wafer (i.e. after treatment with piranha solution) were also measured and are reported in Table 4.5. As received wafers have a water contact angle characteristic of the native silica layer, i.e. about 58°, which is somewhat hydrophilic. As expected, the addition of hydroxyl groups at the surface significantly decreases the water contact angle down to about 10°[22].

**Table 4.3: Measured (C-O) XPS intensities for Linear ii) PEG films grafted from 0.5 and 15 % w/v solutions. (C-O) intensities were used to calculate PEG Linear ii) film thicknesses, which were compared to thicknesses measured by ellipsometry. Grafting densities $\sigma$ were calculated using equation (5), while grafting point separation distances $L$ were calculated using equation (6). $R_G$ values were obtained from the previous study (Chapter III).**

| | Grafted Linear ii) from 0.5% (w/v) solutions | | | Grafted Linear ii) from 15% (w/v) solutions | | |
|---|---|---|---|---|---|---|
| XPS (C-O) intensity $I$ (counts) | 811 | 784 | 859 | 678 | 672 | 833 |
| Calculated XPS thickness $d$ (Å) | 13.7 | 13.1 | 14.8 | 10.8 | 10.7 | 14.2 |
| Ellipsometry thickness $d$ (Å) | 14.8 ±0.7 | 12.4 ±0.5 | 12.6 ±0.3 | 12.7 ±0.6 | 12.2 ±0.3 | 12.4 ±0.4 |
| Grafting density $\sigma \times 10^4$ (molecules/Å$^2$) | 36.8 | 30.8 | 31.3 | 31.5 | 30.3 | 30.8 |
| Grafting point separation $L$ (Å) | 16.5 | 18.0 | 17.9 | 17.8 | 18.2 | 18.0 |
| Calculated $R_G$ (Å) | 20.7 | | | | | |
| Expected hydrated conformation | Brush with significant chains overlap | | | | | |

**Table 4.4: Water contact angles measured for Linear ii) films self-assembled from 0.5 and 15% w/v solutions. The sessile drop method was used and measurements were taken at 3 different spots on each sample.**

| | Grafted Linear ii) from 0.5% (w/v) solutions | Grafted Linear ii) from 15% (w/v) solutions |
|---|---|---|
| Water contact angle $\theta$ (°) | 57 ± 3 | 61 ± 3 |
| Overall $\theta$ average and standard deviation (°) | 59 ± 3 | |

**Table 4.5: Water contact angles measured for as received silicon wafers and hydroxylated silicon wafers (i.e. surface-modified with hydroxyl groups due to treatment with oxidizing piranha solution). The sessile drop method was used and measurements were taken at 3 different spots on each sample.**

| | Bare silicon wafer | Hydroxylated silicon wafer |
|---|---|---|
| Water contact angle $\theta$ (°) | 58 ± 1 | 10 ± 1 |

Linear ii) PEG coatings increase the water contact angle back to about 59°. This is believed to be due to the amphiphilic nature of the triethoxysilane-functionalized PEG molecules which have been self-assembled here. The triethoxysilane moiety is known to be hydrophobic, while the PEG moiety is hydrophilic because these experiments were conducted below the cloud point. Coating comprised of linear PEG chains of molecular weight averaging 600 g/mol with silane bridges linking PEG chains to the wafer have been reported to exhibit water contact angles around 15-20°[22]. Therefore, the additional increase in the contact angle that we observed from Linear ii) films compared to hydroxylated wafers, appears to be due to the rather hydrophobic triethoxysilane moieties.

2. Star-shaped PEG film thickness and grafting density

The same analysis procedure as that used with linear films was used to calculate the thickness and grafting density of star-shaped PEG films synthesized using Stars4 OEG molecules. The obtained values are reported in Table 4.6. Similarly to the Linear ii) PEG films, both PEG star solution concentrations led to the same range of film thickness

as calculated using the XPS (C-O) intensity and as measured by ellipsometry. However, the sample-to-sample variation between measured thicknesses for Stars4 films was larger than that observed for Linear ii) films. This larger variation may arise from the fact that PEG stars appear to be in the mushroom conformation which induces a much less ordered layer compared to linear chains in the densely packed brush conformation. Generally, the Stars4 PEG films are thinner than the Linear ii) PEG films in the dried state because stars are comprised of ~640 g/mol arm, whereas linear molecules are 2393 g/mol long. However, in the hydrated state, the radius of gyration serves to estimate the effective hydrated diameter $d_{wet}$ of grafted linear and star-shaped PEG molecules[16], which defines the area occupied by PEG molecules in solution and is given by:

$$d_{wet} = 2R_G \tag{7}$$

Also, as expected, the number of chains grafted per unit area is significantly larger for the Stars4 films than for the Linear ii) ones ($0.829 \pm 0.030$ chains/nm$^2$ vs. $0.319 \pm 0.024$ chains/nm$^2$, respectively). This general trend agrees with previous studies which have compared the surface attachment density of linear vs. star-shaped PEG molecules[16, 23]. Grafted PEG stars seem to consistently exhibit higher numbers of chain per unit area due to large number of arms per molecule. While Huang[23] observed that the surface attachment density of 4-arm stars was larger by a factor of 4-5, the experiments described here on indicated an increase of a factor of ~2.6 for the surface attachment density of Stars4 vs. Linear ii). The lower chain density increase in the results reported here may be due to the functional end groups. There were 4 amine groups per star molecules, whereas as reported here, the hydrolysis reaction may have resulted in some uncondensed hydroxyl end groups on the Stars4 molecules. It was demonstrated that 3 of these 4 amines per star molecule had reacted and formed bonds with the substrate. Reduced lateral dimensions for the stars attached by 3 out of their 4 arms were hypothesized to be responsible for the 4.5 fold increase in chain attachment density at all times. In the results reported here, Stars4 are core-functionalized and thus have free arms as opposed to arms tethered to the surface.

**Table 4.6: Measured (C-O) XPS intensities for Stars4 PEG films grafted from 0.5 and 15 % w/v solutions. (C-O) intensities were used to calculate PEG Linear ii) film thicknesses, which were compared to thicknesses measured by ellipsometry. Grafting densities $\sigma$ were calculated using equation (5), while grafting point separation distances $L$ were calculated using equation (6). The number of chains per Å$^2$ was calculated by multiplying $\sigma$ by 3.5 which is the average number of arms for Stars4 as characterized by $^{29}$Si NMR. $R_G$ was obtained from the previous study (Chapter III).**

| | Grafted Stars4 from 0.5% (w/v) solutions | | Grafted Stars4 from 15% (w/v) solutions | |
|---|---|---|---|---|
| XPS (C-O) intensity $I$ (counts) | 501 | 484 | 520 | 400 |
| Calculated XPS thickness $d$ (Å) | 7.5 | 7.2 | 7.9 | 5.8 |
| Ellipsometry thickness $d$ (Å) | 7.2 ± 0.6 | 9.0 ± 0.2 | 4.9 ± 0.8 | 8.4 ± 0.3 |
| Grafting density $\sigma \times 10^4$ (molecules/Å$^2$) | 24.5 | 24.2 | 23.4 | 22.6 |
| Number of chains$\times 10^4$/Å$^2$ | 85.8 | 84.7 | 81.9 | 79.1 |
| Grafting point separation $L$ (Å) | 20.2 | 20.3 | 20.7 | 21.0 |
| Calculated $R_G$ (Å) | 17.9 | | | |
| Expected hydrated conformation | Mushroom with significant chain overlap | | | |

This may increase the exclusion volume of Stars4 which may increase the stars lateral dimensions, resulting in the lower increase in chain density observed at the surface in our study. The chain attachment density that is reported here is about 1 order of magnitude larger than that previously reported by Huang[23], which is explained by the fact that Stars4 have significantly lower molecular weight than 10 000 g/mol, which allows for tighter packing at the surface due to lower excluded volumes. Sofia[15] also observed dramatic grafting density increase as the molecular weight of linear PEG chains decreased from 20 000 to 3400 g/mol. Such an increase in chain attachment density was not observed when 3 to 4-arm polystyrene stars were tethered from a 1 wt % solution (good solvent) on silicon wafers and compared to linear polystyrene molecules with

equivalent molecular weight[21]. This increased chain attachment density for star-shaped vs. linear molecules may be specific to PEG polymers in good solvents.

Comparing the grafting point separation $L$ to Stars4 radius of gyration $R_G$ suggests that grafted PEG stars would be in a mushroom conformation with significant chain overlap because $R_G^{\text{Stars4}} < L^{\text{Stars4}} < 2R_G^{\text{Stars4}}$. Again, the solution concentration does not seem to affect the obtained conformation as similar $L$ values are obtained for both concentrations. Viswanathan[21] grafted polystyrene stars from a 1 wt % solution on silicon wafers. These star polymers, which have similar number of arms as that of Stars4 PEG molecules and which were comprised of trimethoxysilane functionalities, were found to give rise to films in the mushroom conformation as well. Based on $d_{wet}$ and grafting point separation $L$ values reported for Linear ii) and Stars4 PEG films, the surface may be modeled as shown below in Figure 4.4.

Static water contact angles were measured for Stars4 PEG films using the sessile drop method and the results are presented in Table 4.7. With an average contact angle of about 42°, the Stars4 films were found to be more hydrophilic than the Linear ii) films which were characterized by a contact angle of about 59°. This 17° water contact angle decrease agrees with the fact that Stars4 films are characterized by significantly more PEG chains per unit area compared to Linear ii) films as calculated and reported in Tables 4.3 and 4.6. Figure 4.5 illustrates the change in water contact angle as a function of its surface modification.

Table 4.8 summarizes the various studied properties for Linear ii) and Stars4 PEG films. Averages and standard deviations are given and were calculated using values reported in Tables 4.3-4.6. Generally, film thickness calculated from the XPS ether peak intensity correlate with those measured by ellipsometry.

3. Protein adsorption studies

Human albumin adsorption was allowed on 4 linear ii) and 4 Stars4 PEG films for 18 hrs at room temperature. Since human albumins are comprised of 15% nitrogen, the XPS nitrogen N 1s peak intensity was used to compare the amount of albumin adsorbed on films to those adsorbed on bare silicon wafers.

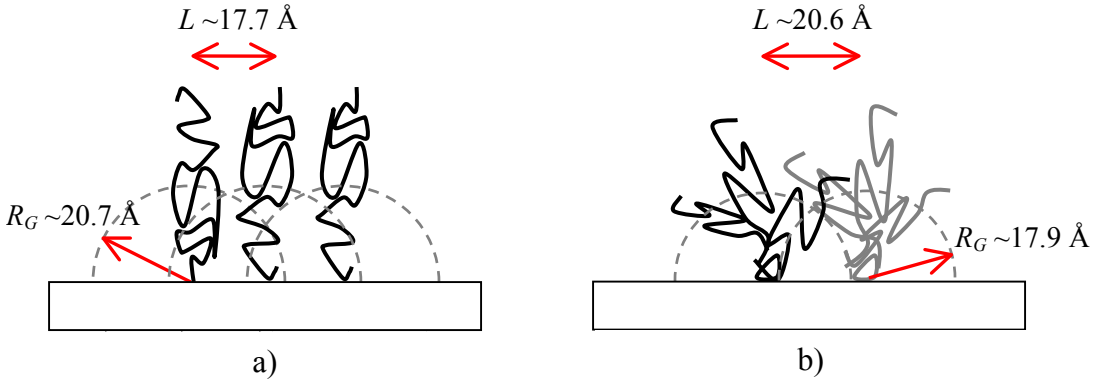


**Figure 4.4: Model of a) Linear ii), and b) Stars4 PEG film conformations in a good solvent. Stars4 have between 3 and 4 arms. The dashed lines represent the occupancy of PEG molecules in the hydrated state with a diameter $d_{wet} = 2R_G$.**

**Table 4.7: Water contact angles measured for Linear ii) films self-assembled from 0.5 and 15% w/v solutions. The sessile drop method was used and measurements were taken at 3 different spots on each sample.**

| | Grafted Stars4 from 0.5% (w/v) solutions | Grafted Stars4 from 15% (w/v) solutions |
|---|---|---|
| Water contact angle $\theta$ (°) | 40 ± 4 | 43 ± 5 |
| Overall $\theta$ average and standard deviation (°) | 42 ± 4 | |

A single N 1s peak appeared around 400.00 eV in all cases. Note that Linear ii) and Stars4 respectively have 1 and 3-4 nitrogen atoms in their structure. Thus the N 1s intensity obtained from each coating before protein adsorption was subtracted from the measured N 1s intensity after adsorption in order to obtain the contribution from albumins only. The N 1s intensities measured for the 8 films and for the 4 bare silicon wafers are reported in Table 4.9.

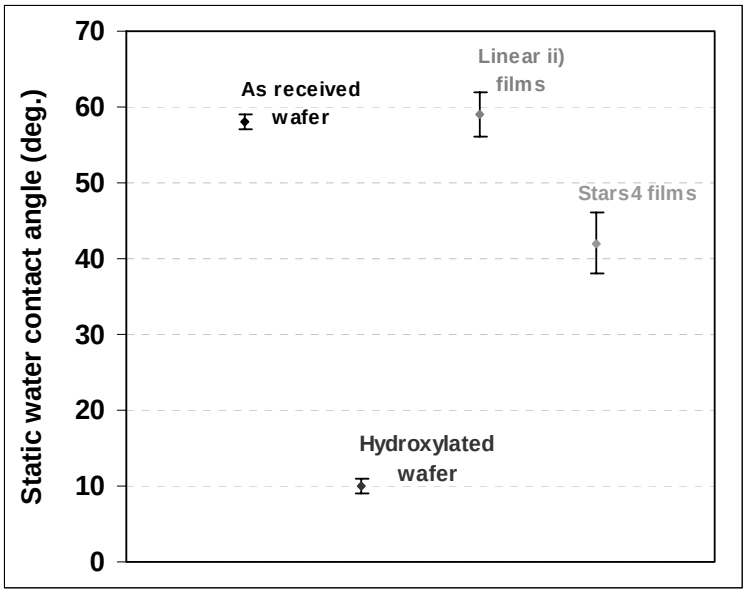


**Figure 4.5: Change in Change in water contact angle as a function of wafer surface modification. A significant drop is noticed between Linear ii) and Stars4 films due to increasing number of PEG chains per unit area for Stars4 compared to Linear ii) films. The contact angles of Linear ii) films are similar to those of the native $SiO_2$ wafer layer.**

**Table 4.8: Summary of various properties for Linear ii) and Stars4 films. Averages and standard deviations were calculated from values reported in Tables 4.3-4.6. $d_{wet}$ was calculated as $2R_G$ as stated by equation (7).**

| | Linear ii) films | Stars4 films |
|---|---|---|
| XPS (C-O) intensity $I$ (counts) | 773 ± 80 | 476 ± 53 |
| Calculated XPS thickness $d$ (Å) | 12.9 ± 1.7 | 7.1 ± 0.9 |
| Ellipsometry thickness $d$ (Å) | 12.8 ± 1.0 | 7.4 ± 1.8 |
| Grafting density $\sigma \times 10^4$ (molecules/Å$^2$) | 31.9 ± 2.4 | 23.7 ± 0.9 |
| Number of chains$\times 10^4$/Å$^2$ | 31.9 ± 2.4 | 82.9 ± 3.0 |
| Grafting point separation $L$ (Å) | 17.7 ± 0.6 | 20.6 ± 0.4 |
| Calculated $R_G$ (Å) | 20.7 | 17.9 |
| Calculated $d_{wet}$ (Å) | 41.4 | 35.8 |
| Expected hydrated conformation | Brush with significant chain overlap | Mushroom with significant chain overlap |
| Water contact angle (°) | 59 ± 3 | 42 ± 4 |

There was no difference found between the amounts of albumin adsorbed on Linear ii) films made from a 0.5% tethering solution compared to that adsorbed on Linear ii) films made from a 15% tethering solution. This was due to the fact that, as seen in the previous sections, both grafting solution concentrations resulted in Linear ii) films with dense brush conformation and significant chain overlap. Stars4 films behaved similarly, as no difference could be noticed between the N 1s intensity obtained for films self-assembled from 0.5 and 15% grafting solutions. Again, PEG stars were shown to be in the mushroom conformation for both of these grafting solution concentrations.

**Table 4.9: Intensity of XPS N 1s peaks obtained from 4 Linear ii) and 4 Stars4 films which were immersed in albumin solutions for 18 hrs. N 1s intensities are proportional to the thickness of the adsorbed albumin overlayers. These intensities are compared to those obtained for uncoated silicon wafers.**

| | N 1s intensity (counts) |
|---|---|
| Adsorbed albumin on Linear ii) films | 454 ± 53 |
| Adsorbed albumin on Stars4 films | 450 ± 173 |
| Adsorbed albumin on uncoated silicon wafers | 1067 ± 135 |

Comparatively, uncoated silicon wafers adsorbed significantly more albumin as the N 1s intensity on uncoated wafers is larger than that on coated wafer by a factor of about 2.4. This suggests that the albumin layer on uncoated wafers is at least twice as thick as those measured on Linear ii) and Stars4 films. Therefore, both coating architectures significantly reduced the amount of adsorbed albumin. However, there was no statistical difference between the N 1s intensity arising from the Linear ii) films compared to those arising from the Stars4 films. This suggests that similar albumin amounts would have adsorbed on Linear ii) and Stars4 films, and that the linear and stars film architectures corresponding to overlapping brush and mushroom conformations, respectively, did not affect protein adsorption. Figure 4.6 illustrates the averages and standard deviations of N 1s intensities obtained for coated and uncoated silicon wafers.

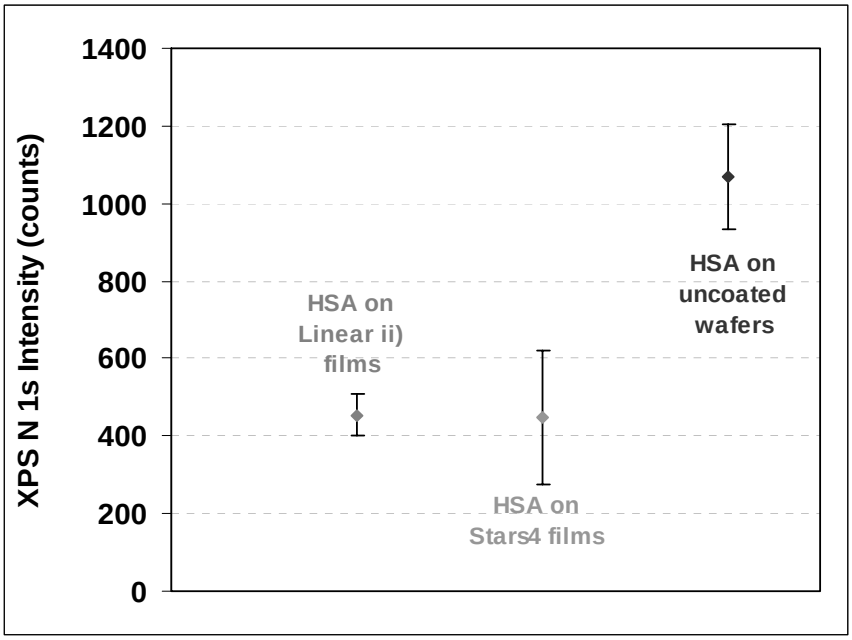


**Figure 4.6: Measured N 1s intensities arising from albumin overlayers deposited on Linear ii) and Stars4 films, as well as uncoated silicon wafers. 4 samples were tested in each case, from which averages and standard deviations were calculated.**

The thickness of adsorbed albumin layers on Linear ii) and Stars4 films, as well as on 4 bare wafers, which had been immersed for 18 hrs and at room temperature in a 4 mg/ml protein solution at pH 7, was measured in air using ellipsometry. As shown in Table 4.10, the average albumin layer thickness as measured on 4 uncoated silicon wafers was found to be around 25 Å. This value agrees very well with previously reported adsorbed albumin thicknesses on silicon wafers native silica layer[16, 24]. While Su[24] measured an hydrated albumin thickness of about 30 Å corresponding to pH 7 and a bulk concentration around 3 mg/ml, Irvine[16] found a dried thickness close to 68 Å. It is well accepted that albumin structural deformation may occur upon adsorption on a surface[24]. For example, at pH 7 and around albumin physiological concentration, albumins were found to adsorb with their long axis (140 Å-long) parallel to the surface plane and were characterized by a thickness smaller than the dimension of their small axis, i.e. 40 Å. This suggests that some structural deformations occur upon adsorption on a hydrophilic surface, i.e. native silica layer. The 25 Å-thick albumin layer measured here with ellipsometry may therefore correspond to the same type of structural deformation upon adsorption on uncoated silicon wafers. Based on the N 1s intensities

reported in Table 4.9, we may assume that the thickness of albumin layer on Linear ii) and Stars4 films is about half that measured on uncoated wafers, which would correspond to about 12 Å in thickness. This value agrees very well with previously reported values obtained for linear PEG coatings with low surface densities (i.e. below chain overlap) and measured in air with ellipsometry after immersion in a 2 mg/ml albumin solution for 24 hrs[15]. Here, both Linear ii) and Stars4 films are believed to exhibit significant chain overlap, which according to Sofia's study should not give rise to such thick albumin layers. However, 4 mg/ml albumin solutions were used here as opposed to only 2 mg/ml by Sofia[15]. This much higher concentration may explain the unexpectedly thick albumin layers obtained on Linear ii) and Stars4 films, as protein concentration is known to strongly affect adsorption amounts along with pH, ionic strength, and temperature[24, 25]. Clearly, there is a large sample-to-sample variation, which is often observed in protein adsorption experiments[15, 16].

Ellipsometry measurements were also performed on Linear ii) and Stars4 films after immersion in albumin solution but were not found reliable compared to those obtained on bare silicon due to the PEG layer itself. PEG molecules are known to swell when immersed in aqueous solutions such as the one which was used for these protein adsorption experiments. This swelling results in an increase of the thickness of PEG layers by several orders of magnitudes. More than a 200% increase in thickness was reported for hydrated amorphous linear PEG films with similar molecular weight[4]. Because the samples were not extensively dried after protein adsorption experiments residual hydrogen-bound water was probably present within the PEG films, therefore increasing its thickness. Additionally, a 3-medium interfacial system was considered for all the ellipsometry experiments, where PEG and albumin are treated as a single layer due to similar refractive indices. The protein layer thickness measurement is thus only possible if the self-assembled PEG layer thickness is known at the time of the measurement, which was not the case here. Note that this was not an issue for the albumin layer on uncoated wafers as the system was only comprised of bulk silicon, silica, and albumin. This swelling factor is not believed to be problematic with XPS N 1s

intensity measurements, as most of the nitrogen signal arises specifically from the albumin layer and not from PEG films.

**Table 4.10: Adsorbed albumin layer thickness on uncoated silicon wafers as measured with ellipsometry. 4 wafers were tested and 3 measurements were taken on each sample. Note the large variation associated with this data set.**

| | Ellipsometry thickness (Å) |
|---|---|
| Adsorbed HSA on uncoated wafers | 24.4 ± 15.2 |

Water contact angles were measured for adsorbed albumin layers on Linear ii) films, Stars4 films, and uncoated silicon wafers and are reported in Table 4.11 and plotted in Figure 4.7. The values obtained for adsorbed HSA on Linear ii) films are slightly larger than those obtained for Stars4 films. Additionally, there was no statistical difference between the contact angle values obtained for adsorbed HSA on Linear ii) films and uncoated wafers. Overall, the HSA layer increased the contact angles of both Linear ii) and Stars4 films. This overall contact angle increase may be due to hydrophobic moieties present at the surface of the HSA layer, as albumins are comprised of both hydrophobic and hydrophilic moieties. The slightly lower contact angles observed for HSA-coated Stars4 films compared to those observed with HSA-coated Linear ii) films and uncoated wafers may arise from slightly different adsorbed conformations, which is known to occur with hydrophilic surfaces[24]. Based on water contact angle values, Stars4 films appear to be significantly more hydrophilic than Linear ii) films as their respective contact angles were found to be 42 and 59°. Additionally, Stars4 films which are in the mushroom conformation should be less ordered than Linear ii) films. This increased disorder within the PEG layer may have given rise to more ethylene glycol units at the surface, which would decrease the contact angle. Or, the slightly lower contact angle observed for HSA-coated Stars4 films may arise from slight conformational differences. Harder[12] reported some drastic contact angle differences for highly ordered PEG SAMs terminated by either OH or $OCH_3$ groups. The contact angle was found to increase from 30-35° to 63°, respectively. A slight increase in structural disorder decreased the contact angle to 57°. It has to be realized that especially Stars4 films, but

also Linear ii) films, are much less ordered than SAMs. Therefore, the conformational change between brushes and mushroom should drastically increase disorder within the PEG layer, which may in turn affect the measured contact angle.

**Table 4.11: Water contact angles measured for the albumin overlayers adsorbed on Linear ii) and Stars4 films, as well as those adsorbed on uncoated silicon wafers. 3 measurements were taken on each sample.**

| | Water contact angle $\theta$ (°) |
|---|---|
| Adsorbed HSA on Linear ii) films | 68 ± 4 |
| Adsorbed HSA on Stars4 films | 58 ± 5 |
| Adsorbed HSA on uncoated wafers | 63 ± 3 |

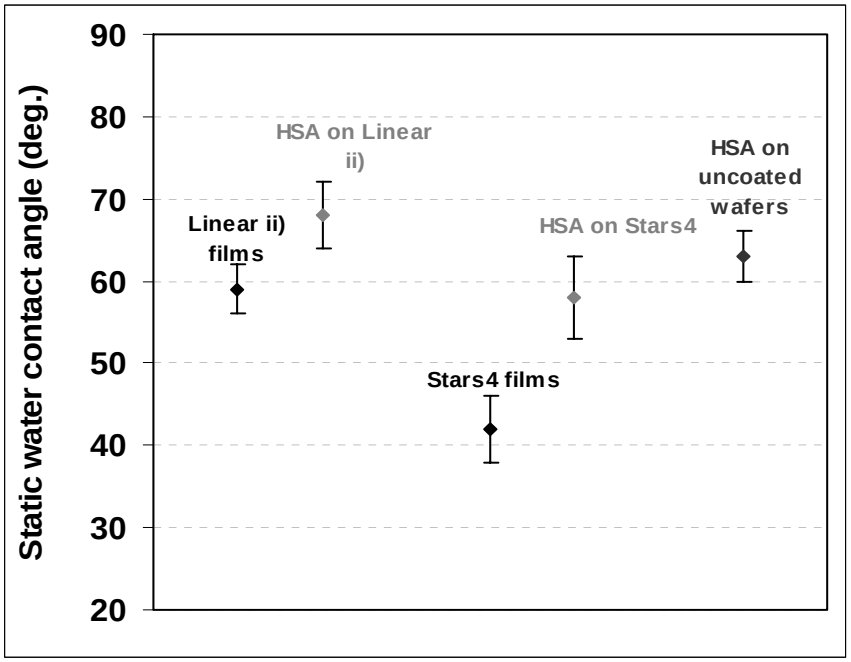


**Figure 4.7: Measured water contact angles for Linear ii) and Stars4 PEG films before and after immersion in albumin (HSA) solution for 18 hrs at room temperature. The contact angle values obtained for the albumin overlayers on Linear ii) and Stars4 films are comparable to those obtained for the albumin overlayer on uncoated wafers.**

**Table 4.12: Summary of various characteristics observed for adsorbed albumin on Linear ii) and Stars4 PEG films, as well as for adsorbed albumin on uncoated silicon wafers.**

| | Adsorbed HSA on Linear ii) films | Adsorbed HSA on Stars4 films | Adsorbed HSA on uncoated wafers |
|---|---|---|---|
| XPS N 1s intensity (counts) | 454 ± 53 | 450 ± 173 | 1067 ± 135 |
| Ellipsometry thickness (Å) | - | - | 24.4 ± 15.2 |
| Water contact angle (°) | 68 ± 4 | 58 ± 5 | 63 ± 3 |

### D. *Conclusion*

In conclusion, linear and star-shaped PEG molecules comprising triethoxysilane functionalities and characterized by similar overall molecular weights around 2400 g/mol, have been successfully self-assembled onto silicon wafers via reactions with hydroxyl groups on the surface. High PEG chain grafting densities were obtained for both molecular architectures at 2 concentrations, i.e. 0.5% which was below the critical concentration (i.e. molecule overlap exist in solution) and 15 % which was above this critical concentration. In both cases self-assembled PEG chains overlap was believed to have occurred, but while the linear chains adopted a dense brush conformation, the star-shaped molecules seemed in the mushroom conformation. While the linear films exhibited very consistent thickness measurements by ellipsometry, those performed on star-shaped films showed a larger variation. While this larger variation may just be due to different swelling amount, it may also suggest that the self-assembly of star-shaped molecules did not lead to as ordered layer structures as those obtained with self-assembled linear molecules due to large molecular lateral dimensions. Based on XPS nitrogen intensity measurements, both film architectures reduced the amount of adsorbed albumins by more than a factor of 2 as compared to that observed on uncoated silicon wafers. However, there was no statistical difference between the amounts of adsorbed albumins on linear films vs. that on star-shaped PEG films. Also, the much higher albumin concentration used here, i.e. 4 mg/ml instead of 1-2 mg/ml as usually seen in the literature, but still within the physiological range, may be responsible for the believed fairly high amount of adsorbed proteins observed on both PEG film architectures.

Uncoated control samples were characterized by a 25 Å-thick albumin layer by ellipsometry in air, which falls within the range of values previously reported.

**References:**


1. Jeon, S.I., Lee, J. H.; Andrade, J. D.; De Gennes, P. G., *Protein-Surface Interactions in the Presence of Polyethylene Oxide. I. Simplified Theory.* J. Colloid Interface Sci., 1991. **142**: p. 149-158.
2. Jeon, S.I., Andrade, J. D., *Protein-Surface Interactions in the Presence of Polyethylene Oxide. II. Effect of Protein Size.* J. Colloid Interface Sci., 1991. **142**: p. 159-166.
3. Morra, M.J., *On the molecular basis of fouling resistance.* J. Biomater. Sci. Polymer Edn., 2000. **11**: p. 547-569.
4. Fick, J., Steitz, R.; Leiner, V.; Tokumitsu, S.; Himmelhaus, M.; Grunze, M., *Swelling Behavior of Self-Assembled Monolayers of Alkanethiol-Terminated Poly(ethylene glycol): A Neutron Reflectometry Study.* Langmuir, 2004. **20**: p. 3848-3853.
5. Harris, J.M., *Poly(ethylene glycol) chemistry: biotechnical and biomedical applications*, ed. J.M. Harris. 1992: Plenum Press.
6. Kjellander, R., Florin, E., *Water structure and changes in thermal stability of the system poly(ethylene oxide)-water.* J. Chem. Soc. Faraday Trans., 1981. **1**: p. 2053-2077.
7. Golander, C.-G., Herron, J. N.; Lim, K.; Claesson, P.; Stenius, P.; Andrade, J. D. , *Properties of Immobilized PEG films and the Interaction with Proteins*, in *Poly(Ethylene Glycol) Chemistry*, J.M. Harris, Editor. 1992, Plenum Press.
8. Lee, J.H., Lee, H. B.; Andrade, J. D., *Blood compatibility of polyethylene oxide surfaces.* Prog. Polym. Sci. , 1995. **20**: p. 1043-1079.
9. Liu, K.J., Ullman, R., *Proton Magnetic Relaxation in Polyethylene Oxide Solutions.* J. Chem. Phys., 1968. **48**: p. 1158-1168.
10. Hammes, G.G., Roberts, P. B., *Cooperativity of Solvent-Macromolecule Interactions in Aqueous Solutions of Polyethylene Glycol and Polyethylene Glycol-Ureal.* J. Am. Chem. Soc., 1968. **90**: p. 7119-7122.
11. Feldman, K., Hahner, G.; Spencer, N. D.; Harder, P.; Grunze, M., *Probing Resistance to Protein Adsorption of Oligo(ethylene glycol)-Terminated Self-Assembled Monolayers by Scanning Force Microscopy.* J. Am. Chem. Soc., 1999. **121**: p. 10134-10141.
12. Harder, P., Grunze, M.; Dahint, R.; Whitesides, G. M.; Laibinis, P. E., *Molecular Conformation in Oligo(ethylene glycol)-Terminated Self-Assembled Monolayers on Gold and Silver Surfaces Determines Their ability to Resist Protein Adsorption.* J. Phys. Chem. B, 1998. **102**: p. 426-436.
13. Dicke, C., Hahner, G., *pH-Dependent Force Spectroscopy of Tri(ethylene Glycol)- and Methyl-Terminated Self-Assembled Monolayers Adsorbed on Gold.* J. Am. Chem. Soc., 2002. **124**: p. 12619-12625.
14. Wang, R.L.C., Kreuzer, H. J.; Grunze, M., *Molecular Conformation and Solvation of Oligo(ethylene glycol)-Terminated Self-Assembled Monolayers and Their Resistance to Protein Adsorption.* J. Phys. Chem. B, 1997. **101**: p. 9767-9773.

15. Sofia, S.J., Premnath, V.; Merrill, E. W., *Poly(ethylene oxide) Grafted to Silicon Surfaces: Grafting Density and Protein Adsorption.* Macromolecules, 1998. **31**: p. 5059-5070.
16. Irvine, D.J., Mayes, A. M.; Satija, S. K.; Barker, J. G.; Sofia-Allgor, S. J.; Griffith, L. G., *Comparison of tethered star and linear poly(ethylene oxide) for control of biomaterials surface properties.* J. Biomed. Mater. Res., 1998. **40**: p. 498-509.
17. Prime, K.L., Whitesides, G. M., *Adsorption of proteins onto surfaces containing end-attached oligo(ethylene oxide): A model system using self-assembled monolayers.* J. Am. Chem. Soc., 1993. **115**: p. 10714-10721.
18. Powell, C.J., Jablonski, A., *Electron effective attenuation lengths for applications in Auger electron spectroscopy and x-ray photoelectron spectroscopy.* Surf. Interface. Anal., 2002. **33**: p. 211-229.
19. McKeon, K.; Love, B. J.; Byrd, T.; Walz, J. *Measurement of the Self-binding Properties of Albumin*. in *Adhesion Society* 2007. Blacksburg, VA.
20. Vermette, P., Meagher, L., *Interactions of phospholipid- and poly(ethylene glycol)-modified surfaces with biological systems: relation to physico-chemical properties and mechanisms.* Colloids and Surfaces B: Biointerfaces, 2003. **28**: p. 153-198.
21. Viswanathan, K., Long, T. E.; Ward, T. C., *Silicon Surface Modification with Trialkoxysilyl-Functionalized Star-Shaped Polymers.* J. Poly. Sci. Part A: Poly. Chem., 2005. **43**: p. 3655-3666.
22. Zhang, M., Desai, T.; Ferrari, M., *Proteins and cells on PEG immobilized silicon surfaces.* Biomaterials, 1998. **19**: p. 953-960.
23. Huang, H., Fulchiero, E. C.; Penn, L. S., *Comparison of tethering of linear and four-arm poly(ethylene oxide).* Macromolecules, 2005. **38**: p. 1028-1030.
24. Su, T.J., Lu, J. R.; Thomas, R. K.; Cui, Z. F., *Effect of pH pn the Adsorption of Bovine Serum Albumin at the Silica/Water Interface Studied by Neutron Reflection.* J. Phys. Chem. B, 1999. **103**: p. 3727-3736.
25. Norde, W., *Driving Forces for Protein Adsorption at Solid Surfaces*, in *Biopolymers at interfaces*, M. Malmsten, Editor. 2003, Marcel Dekker, Inc. p. 21-44.

# CHAPTER V.

## CONCLUSIONS

To conclude, linear and star-shaped PEG derivatives comprised of 2.5 to 3.5 arms have been synthesized and have been shown to comprise triethoxysilane functionalities. These triethoxysilane core-functionalized linear and star-shaped PEG molecules were subsequently self-assembled onto hydroxylated silicon wafers via covalent reactions and human albumin adsorption was studied. Both linear and star-shaped PEG molecules were found to be well-defined polymers. PEG stars were formed based on the hydrolysis and condensation of pre-functionalized linear molecules in acidic water and at room temperature. The albumin adsorption resistance of linear and star-shaped PEG molecules has been extensively studied in the literature. In fact, PEG stars, with hard-sphere-like structures resulting from their large number of arms (20-72), have generally showed a lower ability in reducing protein adsorption compared to linear PEG molecules. This was shown to be due to the high steric hindrance associated with the large number of arms, which resulted in difficulties to achieve overlapping chains with such PEG stars. Additionally, linear PEG molecules were generally characterized by molecular weights more than 1 order of magnitude lower than those of star-shaped PEG molecules. Here, PEG stars with significantly fewer arms (3-4) and linear PEG molecules have been self-assembled on silicon wafers and studied in terms of their albumin adsorption resistance. PEG stars' self-assembly has resulted in overlapping chains in the mushroom conformation whereas linear PEG chains' self-assembly resulted in overlapping chains in the brush conformation. The low number of arms characterizing the star molecules is believed to have led to the observed overlapping PEG stars' chains. Additionally, the molecular weight of linear and star-shaped PEG molecules was closely matched and found to be around 2400 g/mol. Although these linear and star PEG oligomers have matching molecular weights, their melting temperatures were found to be significantly different, as stars had a much lower melting point than linear molecules (~17 vs. 51ºC). While stars had a gel-like appearance at room temperature, linear molecules were flaky.

Also, star-shaped PEG films were shown to be significantly more hydrophilic than linear PEG films (~42 vs. 59º), which was due to a higher PEG chain concentration for star-shaped PEG films compared to that for linear films. Human albumin adsorption on linear and star-shaped PEG oligomers were studied based on XPS nitrogen intensity measurements. Both film architectures reduced the amount of adsorbed albumins by more than a factor of 2 as compared to the adsorption observed on uncoated silicon wafers. Uncoated control samples were characterized by a 25 Å-thick albumin layer as measured by ellipsometry in air, which falls within the range of values previously reported in the literature. However, there was no statistical difference between the amounts of adsorbed albumins on linear films vs. that on star-shaped PEG films. Based on these results, it seems that self-assembled PEG star molecules in the mushroom conformation and which were characterized by 3-4 arms/molecule did not improve the resistance to human albumin adsorption compared to linear PEG molecules. Therefore, the higher PEG segment concentration arising from the star structure did not further reduce protein reduction compared to the linear structure.

# CHAPTER VI.

## FUTURE WORK

### A. *Protein adsorption study using ellipsometry*

Although the thickness of the albumin layer adsorbed on bare silicon wafers was estimated using ellipsometry, the protein layer thickness adsorbed on Linear ii) and Stars4 PEG coatings could not be precisely estimated using the same technique. This was due to significant swelling of the PEG films during the albumin adsorption experiments and to the fact that the HSA-PEG coated silicon wafers were very gently dried under nitrogen flow. This drying procedure was expected to leave the surface hydrated. Therefore, grafted linear and star-shaped PEG molecules were expected to be bound to water molecules when ellipsometry measurements were attempted. More than a 200% increase in thickness was reported[1] for amorphous PEG films in the hydrated state and of molecular weight similar to those used here. This demonstrates the dramatic effect of water-PEG interaction on the thickness of PEG films.

To resolve this issue, the thickness of both Linear ii) and Stars4 PEG films grafted on silicon wafers could be estimated by conducting ellipsometry experiments using Linear ii) and Stars4 PEG films in the hydrated state. 3 types of experiments could be envisioned. First, the swelling of Linear ii) and Stars4 PEG films in the HSA-PEG coated wafers could be mimicked by immersing Linear ii) and Stars4 coated wafers in phosphate buffered saline (PBS), pH=7.4, for 18 hrs at room temperature. The coated wafers would then be gently dried under a nitrogen flow and the hydrated thickness would be immediately obtained from ellipsometry data. This would ensure that the HSA and PEG films would be in similar hydrated conditions when measuring their respective thicknesses. The hydrated PEG thickness would then be subtracted from the total thickness obtained for the HSA-PEG coated wafer systems, which would lead to an estimate of the HSA layer thickness adsorbed on Linear ii) and Stars4 PEG films.

Because adsorbed water molecules within the PEG films would significantly increase the dielectric constant of the PEG-water layer (i.e. hydrated PEG films), the main challenge would be to correctly estimate the dielectric constant or refractive index of the PEG-water interface, which is needed to calculate film thickness. The second type of experiments could involve measurements of PEG films immersed in PBS as opposed to measurements obtained in air. This would maximize the swelling of both PEG films and allow the calculation of their respective thickness in the hydrated state. Linear ii) and Stars4 PEG films in PEG coated wafers would be placed in a liquid cell filled with PBS. Finally, the in-situ adsorption of albumin and other proteins onto PEG-coated substrates as well as uncoated substrates could be monitored using ellipsometry. The kinetics of protein adsorption could be accurately followed. Transparent substrates such as quartz or glass as opposed to silicon wafers would allow to measure reflectivity parameters from the back of the film-albumin interface. This would minimize the effect of the HSA dissolved in PBS medium on the reflection at the interface. Adsorbed protein layer thickness would thus be measured in-situ and as a function of time. Comparing protein adsorption kinetics and protein layer thickness obtained for linear and star-shaped PEG films may allow to resolve a difference between the protein adsorption properties of these 2 PEG molecular architectures.

### B. *Protein adsorption study using neutron reflectivity*

Neutron reflectivity (NR) has great potential to study layers interfaces due to the neutron resolution perpendicular to the substrate plane. Information about layer conformation and thickness, water absorption, surface coverage, and interface roughness can be determined from the reflectivity curves using a box model. Films may be studied under various environments including air, and protein dissolved in deuterium oxide ($D_2O$). NR is therefore an interesting tool to study in-situ protein adsorption. NR is sensitive to neutrons scattering length which offer a good resolution between adjacent atoms in the periodic table whereas x-ray reflectivity, arising from atom's electron density, increases with the atomic number. For instance, the great contrast provided between hydrogen and

deuterium isotopes is very useful for organic films comprised of carbon, hydrogen, oxygen and silicon. Of particular interest here, would be the adsorbed protein/PEG interface, which would be compared to the adsorbed protein/uncoated substrate interface. Based on the known scattering length density of deuterium oxide, hydrogen, silicon, silicon dioxide, PEG, and proteins in $D_2O$ (6.35, -0.56, 2.07, 3.60, 0.56, and $3.42 \times 10^{-6} Å^{-2}$, respectively), it is possible to enhance the reflectivity contrast between PEG films and adsorbed protein films by having a fully deuterated PEG film as opposed to a protonated film which has a fairly low scattering length density[2]. The adsorbed protein layer thickness on PEG films and uncoated substrates would be obtained and the conformation of Linear ii) and Stars4 PEG films could be compared to those hypothesized in Chapter IV based on XPS data. In-situ adsorption kinetic studies may also be conducted, i.g. data taken every hour, and may lead to the observation of different adsorption kinetics for Linear ii) PEG films in the brush conformation vs. Stars4 PEG films in the mushroom conformation.

### C. *Other biocompatibility studies*

Protein adsorption is believed to be dependent on several factors including protein solution concentration, pH, temperature, and ionic strength[3, 4]. The albumin adsorption experiments reported in Chapter IV were conducted at a 4 mg/ml protein concentration, which is twice that commonly utilized in the literature, although still within the physiological concentration range. Future work should include albumin adsorption experiments conducted at a 2mg/ml concentration. In addition to albumin adsorption studies, other proteins (i.e. fibrinogen and high molecular weight kininogen) and cells such as platelets are involved in the coagulation cascade[5, 6] and are therefore considered important factors which could be assessed in the future. Finally, *ex-vivo* and *in-vivo* biocompatibility properties could be assessed by studying tissue compatibility, blood compatibility, protein adsorption, and cell adhesion. *Ex-vivo* experiments could involve applying PEG films on hemodialysis components such as the various tubing which come into play in this therapy. Overlapping linear and star-shaped PEG chains

could be achieved by pre-functionalizing the various polymeric substrates using oxygen plasma etching. This would insure the substrates' surface modification with the addition of hydroxyl (OH) and carboxylic acid (COOH) functionalities which would then react with triethoxysilane functionalized linear and star-shaped PEG oligomers. *In-vivo* experiments could be performed by inserting coated components in small animal arteries. Blood fluids and cells are comprised of various interacting proteins and cells, where competitive protein adsorption results in adsorption and desorption events (i.e. The Vroman Effect[4, 7]), which directly affects cell adhesion and blood coagulation.

**References:**


1. Fick, J.; Steitz, R.; Leiner, V.; Tokumitsu, S.; Himmelhaus, M.; Grunze, M., *Swelling Behavior of Self-Assembled Monolayers of Alkanethiol-Terminated Poly(ethylene glycol): A Neutron Reflectometry Study.* Langmuir, 2004. **20**: p. 3848-3853.
2. Fragneto, G.; Su, T. J.; Lu, J. R.; Thomasa, R. K.; Rennie, A. R., *Adsorption of proteins from aqueous solutions on hydrophobic surfaces studied by neutron reflection.* Phys. Chem. Chem. Phys., 2000. **2**: p. 5214-5221.
3. Su, T. J.; Lu, J. R.; Thomas, R. K.; Cui, Z. F., *Effect of pH pn the Adsorption of Bovine Serum Albumin at the Silica/Water Interface Studied by Neutron Reflection.* J. Phys. Chem. B, 1999. **103**: p. 3727-3736.
4. Norde, W., *Driving Forces for Protein Adsorption at Solid Surfaces*, in *Biopolymers at interfaces*, M. Malmsten, Editor. 2003, Marcel Dekker Inc. p. 21-44.
5. Basmadjian, D.; Sefton, M.; Baldwin, S., *Coagulation on biomaterials in flowing blood: some theoretical considerations.* Biomaterials, 1997. **18**: p. 1511-1522
6. Michal, G., *Blood Coagulation and Fibrinolysis*, in *Biochemical Pathways*, G. Michal, Editor. 1999, Wiley Spektrum.
7. Ball, V.; Schaaf, P.; Voegel, J.-C., *Mechanism of Interfacial Exchange Phenomena for Proteins Adsorbed at Solid-Liquid Interfaces*, in *Biopolymers at interfaces*, M. Malmsten, Editor. 2003, Marcel Dekker, Inc.

## Vita

Christelle Jullian was born in Montpellier, France, on July 27, 1979. She graduated from the University of Technology of Compiègne, France, in September 2002 with a B.S. in Mechanical Engineering, with a minor in Materials Science and Engineering. She then graduated with a M.S. in Materials Science and Engineering in December 2003 from Virginia Tech. She worked for 1 year at the VT applied biosciences center (VTabc) and began her Ph.D. studies in the Fall of 2004. Christelle defended her Ph.D. in Fall 2007.